

THE DESIGN, FABRICATION, AND PRESSURE TESTING OF A LOW-  
TEMPERATURE CO-FIRED CERAMIC ELECTRIC PROPULSION THRUSTER

By

Derek J. Reis

A thesis

submitted in partial fulfillment

of the requirements for the degree of

Master of Science in Mechanical Engineering

Boise State University

May 2013

© 2013

Derek J. Reis

ALL RIGHTS RESERVED

BOISE STATE UNIVERSITY GRADUATE COLLEGE

**DEFENSE COMMITTEE AND FINAL READING APPROVALS**

of the thesis submitted by

Derek J. Reis

Thesis Title: The Design, Fabrication, and Pressure Testing of a Low-Temperature Co-Fired Ceramic Electric Propulsion Thruster

Date of Final Oral Examination: 12 March 2013

The following individuals read and discussed the thesis submitted by student Derek J. Reis, and they evaluated his presentation and response to questions during the final oral examination. They found that the student passed the final oral examination.

Donald G. Plumlee, Ph.D. Chair, Supervisory Committee

Jim Browning, Ph.D. Member, Supervisory Committee

Amy Moll, Ph.D. Member, Supervisory Committee

The final reading approval of the thesis was granted by Donald G. Plumlee, Ph.D., Chair of the Supervisory Committee. The thesis was approved for the Graduate College by John R. Pelton, Ph.D., Dean of the Graduate College

## ABSTRACT

Electric thrusters have been used for many years for orbital station-keeping and propulsion. As technology advances, smaller satellites are possible that require less thrust. The resulting miniature electric thrusters need low-weight and compact designs. This thesis specifies the design, fabrication, and testing of a thruster and its fluid delivery system designed for use with a micro-satellite weighing less than fifty kilograms.

The advent of Micro-Electro-Mechanical Systems (MEMS) has sparked a new market with incredibly small scale designs. Using this technology with Low-Temperature Co-fired Ceramic (LTCC) materials has spawned the new distinction of Ceramic Micro-Electro-Mechanical Systems (C-MEMS). The thruster body is made entirely out of LTCC and it has embedded electrical connections and gas delivery channels integrated wholly within the thruster. These thrusters are tested inside a vacuum chamber system set up at Boise State University to simulate the pressure ranges seen in typical space applications. Plasma generation requires adequate gas pressures localized to the time-varying electric field inside of a vacuum. Prior testing for prototype thrusters at Boise State University proved that a single hole central gas injection point was not taking full advantage of the locations of high electric field intensity. This was the driving force to generate a computational fluid dynamics (CFD) model to simulate the pressure ranges as they applied to the areas of high electric field intensity. *ANSYS Fluent* was used as the modeling software to simulate the pressure ranges of the gas seen inside the

thruster body. Experimental testing was done to verify the validity of the *Fluent* modeling. Electric field intensity was used as a driving force for the design of the gas outlets and their locations.

The resulting thruster design demonstrated the successful ability to use LTCC as a substrate for a miniature thruster with fully embedded electrical components and gas channels. Experimental testing showed that a multiple hole gas injection concept created a higher localized pressure within the thruster cylinder, which increases plasma efficiency. The increase in localized pressure was as high as 49.8% larger than a single injection hole design. The experimental tests were also used as a method of validation for a CFD model that could be used in future iterations of the thruster to improve the locations of the thruster gas injection holes. Further work should be done with the external connections to the LTCC body to improve long-term durability.

These results imply that LTCC is a viable medium for creating miniature thrusters for micro-satellites. The LTCC creates a hermetically sealed fluidic pathway for neutral gas to travel through, which reduces the size of the overall thruster considerably. A thruster made out of LTCC is both small in size and has excellent qualities to survive the harsh environment of space.

## TABLE OF CONTENTS

ABSTRACT.....	iv
TABLE OF CONTENTS.....	vi
LIST OF TABLES.....	xi
LIST OF FIGURES .....	xii
CHAPTER 1: INTRODUCTION AND BACKGROUND .....	1
1-1 Micro-Satellites .....	1
1-2 Micro-Propulsion.....	1
1-3 Electric Propulsion .....	3
1-3.1 Plasma.....	3
1-3.2 Electrostatic Ion Thrusters.....	5
1-4 Materials Systems Used for Miniature Electric Propulsion Thrusters .....	7
1-4.1 Typical Material Used in Creation of Micro-Thrusters.....	7
1-4.2 Low Temperature Co-Fired Ceramic Material .....	7
1-5 Electric Propulsion at Boise State University.....	11
1-6 Propellant Delivery in Miniature Electric Propulsion Thrusters .....	15
1-7 Thesis Overview .....	18
CHAPTER 2: LOW TEMPERATURE CO-FIRED CERAMIC .....	20
2-1 LTCC at Boise State University .....	20
2-2 Overview of the BSU C-MEMS LTCC Fabrication Process .....	22

2-3 C-MEMS Lab Material and Equipment List .....	25
CHAPTER 3: DESIGN PROCESS .....	27
3-1 Initial Thruster Concept.....	27
3-2 Previous Prototype Thruster Design.....	28
3-3 Design Concerns and Limitations.....	30
3-4 Existing Design Evaluations.....	34
3-4.1 Pressure Tests .....	34
3-4.2 Pressure Test Conclusions .....	39
3-4.3 Antenna Electric Field - <i>COMSOL MultiPhysics</i> Module .....	39
3-5 Version 1 Thruster Design.....	41
3-5.1 Fluid Channel Design .....	42
3-5.2 Design of the Thruster Body Solid Model.....	46
CHAPTER 4: COMPUTATIONAL FLUID DYANAMICS MODEL.....	59
4-1 <i>ANSYS Fluent</i> Software .....	60
4-2 Thruster CFD Model .....	60
4-3 Choked Flow Verification and Critical Pressure Calculations.....	62
4-4 Verification of Continuous or Molecular Flow .....	69
4-5 Thruster CFD Model Boundary Conditions .....	74
4-6 Developing the <i>Fluent</i> CFD Model .....	76
4-6.1 Geometry Creation .....	77
4-6.2 Fluid Flow ( <i>Fluent</i> ) Analysis System Creation in <i>Workbench</i> .....	77
4-6.3 Geometry File Import .....	78
4-6.4 Mesh Creation.....	78

4-6.5 Naming Selections .....	79
4-6.6 CFD Model Conditions Setup .....	80
CHAPTER 5: THRUSTER FABRICATION.....	85
5-1 Thruster Version 1 .....	86
5-1.1 Thruster Version 1 Fabrication Results .....	90
5-1.2 Visible Defects .....	91
5-1.3 Gas Flow .....	92
5-1.4 Electrical Connectivity .....	93
5-2 Thruster Version 2 .....	94
5-2.1 Thruster Version 2 Fabrication Results .....	96
5-2.2 Visible Defects .....	97
5-2.3 Gas Flow .....	98
5-2.4 Electrical Connectivity .....	99
5-3 Thruster Version 3 .....	99
5-3.1 Thruster Version 3 Fabrication Results .....	101
5-3.2 Visible Defects .....	101
5-3.3 Gas Flow .....	102
5-3.4 Electrical Connectivity .....	103
5-3.5 Version 3 Thrusters: Post-Processing.....	103
5-4 Thruster Version 4 .....	107
5-4.1 Thruster Version 4 Fabrication Results .....	109
5-4.2 Visible Defects .....	109
5-4.3 Gas Flow and Electrical Connectivity .....	110



5-5 Final Thoughts on Fabrication Process .....	110
<b>CHAPTER 6: THRUSTER TESTING AND RESULTS .....</b>	<b>113</b>
6-1 Variable Mass Flow Rate Setup .....	113
6-2 Second Version Pressure-Testing Device.....	116
6-3 Single Hole Thruster Body Design.....	118
6-4 Experimental Test Setup and Process.....	119
6-4.1 Equipment Needed For Testing.....	119
6-4.2 Experimental Testing Process .....	120
6-5 Experimental Results .....	121
6-6 CFD Model Results .....	130
<b>CHAPTER 7: SUMMARY AND CONCLUSIONS .....</b>	<b>135</b>
7-1 Four Hole Thruster Design .....	135
7-2 CFD Modeling.....	136
7-3 Future Fabrication Concerns .....	137
7-4 Successful Plasma Generation.....	138
7-5 Conclusions .....	139
<b>REFERENCES .....</b>	<b>141</b>
<b>APPENDIX A.....</b>	<b>149</b>
A-1 Detailed Experimental Setup and Processes.....	149
A-1.1 Thruster Experimental Test Setup .....	150
A-1.2 Preparation of Vacuum Chamber for Testing Conditions .....	155
<b>APPENDIX B .....</b>	<b>160</b>
B-1 MATLAB Code for Argon Interpolation with Convectron Gauges .....	160

B-2 MATLAB Code Example Output.....	163
APPENDIX C.....	165
C-1 Additional Designs.....	165
C-1.1 Thrust Stand Adaptor Plate.....	166
APPENDIX D.....	168
D-1 Cryogenic Pump Gate Valve Operating Instructions .....	168

## LIST OF TABLES

Table 1: Materials List for Thruster Fabrication.....	26
Table 2: Equipment List for Thruster Fabrication .....	26
Table 3: Required Power to Generate Plasma as a Function of Background Chamber Pressure and Antenna Signal Frequency [33].....	30
Table 4: Summary of Thruster Design Concerns and Limitations and Derived Requirements .....	31
Table 5: Values Used in Analysis for Reservoir Pressure Calculations .....	67
Table 6: Calculated Critical and Reservoir Pressure Data for Various Flow Rates .....	68
Table 7: Parameter Values Used for Calculating the Knudsen Numbers.....	71
Table 8: <i>Fluent</i> CFD Model Simulation Chosen Settings .....	81
Table 9: Overview of Thruster Fabrication Results for Version 1 through Version 4 ...	112
Table 10: Thruster Configuration Experimental Delta Pressure Mean Percent Increase Over Full Flow Range.....	129
Table 11: Experimental and <i>Fluent</i> Delta Pressures for 100 sccm Argon Flow .....	132
Table 12: Experimental and <i>Fluent</i> Delta Pressures for 10 sccm Argon Flow .....	132

## LIST OF FIGURES

Figure 1: Plasma Created by a Plasma Ball [18] .....	4
Figure 2: Electrostatic Ion Thruster Firing at the Jet Propulsion Laboratory [21] .....	5
Figure 3: NASA Ion Engine Diagram [21].....	6
Figure 4: Bluetooth Radio Module (10.2 mm x 14.0 mm x 1.66 mm) [28] .....	8
Figure 5: Microfluidic Chemical Analysis Device (2 cm x 3.5 cm x 2 mm) [29].....	9
Figure 6: LTCC Heated Tubes with Thermistors [30].....	10
Figure 7: LTCC Micro-Plasma Generation Devices (Size Not Reported) [31].....	11
Figure 8: BSU Electric Propulsion Project Concept Micro-Satellite Drawing.....	12
Figure 9: BSU Electric Propulsion Project Concept Thruster .....	14
Figure 10: Micro-Combustor Concept in LTCC (Left) and Six Final Devices (Right). Successful high-temperature operation of embedded fluidic channels in LTCC [39].....	21
Figure 11: Miniature Ion Mobility Spectrometer Sensor in LTCC. All of the sensor electrical components are embedded in the ceramic substrate [27].....	22
Figure 12: LTCC Manufacturing Process and Flow [40] .....	23
Figure 13: Side View of Concept Thruster Detailing Components.....	28
Figure 14: Single Injection Hole Thruster Design with LTCC Spacer and Reservoir .....	29
Figure 15: Pressure-Testing Device showing Gas Injection and Tap Locations .....	35
Figure 16: Wall Pressure Tap for Static Pressure Measurement .....	36
Figure 17: Location of Wall Pressure Taps Relative to Antenna Location .....	37
Figure 18: Delta Pressure vs. Argon Flow Rate at Various Pressure Tap Locations .....	38

Figure 19: <i>COMSOL</i> Antenna Electric Field Intensity Model [32].....	40
Figure 20: Gas Distribution Manifold Drawing Distinguishing Parts of the Manifold and the Associated Cross Sections (Top). Rectangular Channel and the Equivalent Hydraulic Diameter of the Channel (Bottom) .....	43
Figure 21: Calculation Showing the Relationship between Number of Layers and Width of Channel for a Hydraulic Diameter of 0.84 mm .....	45
Figure 22: Separate LTCC Components of the Thruster Assembly .....	47
Figure 23: Top-Down View of the Gas Manifold Shape and Location Relative to the Antenna as Well as the Gas Inlet Port .....	49
Figure 24: SMA Connector Reference Geometry Pattern for Base Interconnects .....	50
Figure 25: SMA Connector and Gas Inlet Relative to Antenna .....	51
Figure 26: Thruster Body Showing the Four Alignment Holes Used for Grid Holder Attachment and Thrust Stand Mounting.....	52
Figure 27: Top View (Left) and Side View (Right) Displaying Location of Antenna and Traces with Respect to the Antenna Disc, Thruster Base, and SMA Connector.....	54
Figure 28: Top View of the Gas Injection Holes Relative to Antenna.....	55
Figure 29: Plot of <i>COMSOL</i> Electric-Field Intensity Including the Single Gas Injection Hole as well as the Repositioned Gas Injection Holes [32].....	56
Figure 30: Volume Averaged Electric-Field Intensity of 1 and 4 Injection Hole Antenna Designs [32].....	57
Figure 31: Solid Model of Thruster after Fabrication with Connectors (Left) and a Cross-Sectional View Displaying Gas Channels (Right).....	58
Figure 32: Fluid Flow Path Geometry Created for Analysis of the Four Gas Injection Hole Design .....	61
Figure 33: Converging Nozzle with Choked Flow Conditions Highlighting Fluid Flow Properties and Locations of the Nozzle Relative to the CFD Model.....	62
Figure 34: Reservoir Pressure and Critical Pressure Relationship versus Flow Rate (Valid Only During Choked Flow) .....	69

Figure 35: Plot of Knudsen Number versus Flow Rate for the Gas Injection Hole Exit Locations.....	72
Figure 36: Knudsen Number Plot of the Thruster Containment Cylinder Exit Plane for Pressures (0.01 mTorr to 1 mTorr) and Temperatures (100K, 220K, and 293K) .....	73
Figure 37: Screenshot of <i>DesignModeler</i> Displaying Imported Geometry .....	78
Figure 38: Basic Mesh (Left) and Refined Mesh (Right).....	79
Figure 39: Named Selections Highlighted by Mesh with the Inlet (Left), Outlet (Middle), and Walls (Right).....	80
Figure 40: Background Chamber Pressure versus Flow Rate Data.....	83
Figure 41: Flowchart for Thruster Fabrication Process .....	85
Figure 42: Exploded View of the Different Layer Patterns of the Thruster Base and Antenna Disc.....	86
Figure 43: Thruster Top View (Left) and Bottom View (Right) of Version 1 Thrusters Displaying Cracks that Propagated Through the Thrusters During Firing.....	91
Figure 44: Crack Propagation through the Length of an LTCC Cylinder .....	92
Figure 45: Close up View of a Crack through the Gas Inlet Hole .....	93
Figure 46: Close up View of a Crack through an Electrical Via .....	94
Figure 47: Second Version Thrusters Showing Antenna Shields Partially and Fully Removed (Left Thruster is Elevated Slightly) .....	96
Figure 48: Back Side of Second Version Thrusters Displaying Cracks (Left Thruster Has an SMA Connector Attached to Test Silver Epoxy Bond Strength) .....	98
Figure 49: Close Up View of Hairline Crack by Gas Inlet on a Version 2 Thruster.....	99
Figure 50: Crack Located on the Control Interface Side of a Version 3 Thruster.....	102
Figure 51: Version Three Thruster Crack Filled with Ceramic Epoxy .....	103
Figure 52: Close up View of SMA Connector Showing Silver Epoxy .....	104
Figure 53: SMA Connector Applied with Both Silver Epoxy and Ceramic Epoxy .....	105

Figure 54: Gas Fitting Attached to the Backside of a Version Three Thruster .....	106
Figure 55: Top View (Left) and Section View (Right) of the Area of High Stress Concentration during Pressing.....	107
Figure 56: Version 4 Thruster without Thruster Cylinder, Showing the Top View (Left) and the Bottom View (Right).....	110
Figure 57: Solid Model Design (Left) and Fabricated (Right) Whole Thruster Body Comparison.....	111
Figure 58: Comparison of a Sectional View of the Solid Model (Left) and the Fabricated Thrusters (Right).....	111
Figure 59: Simplified Flow Schematic from Argon Supply to Thruster or Pressure-Testing Device .....	114
Figure 60: Variable Range Mass Flow Controller Setup: Front View (Left) Back View (Right).....	115
Figure 61: Second Version of the Pressure-Testing Device .....	117
Figure 62: Finished Experimental Pressure-Testing Apparatus Shown from Above (Left) and from the Bottom (Right).....	118
Figure 63: Center Hole Single Injection Point Thruster Body Design .....	119
Figure 64: Convectron Gauge Conversion Curve for Argon Gas.....	122
Figure 65: Pressure Tests for 4 Hole Thruster at Various Spacer Heights .....	123
Figure 66: Pressure Tests for 1 Hole Thruster at Various Spacer Heights .....	125
Figure 67: Thruster Comparison of Localized Pressures at Various Spacer Heights.....	126
Figure 68: Low Flow Range (0-10 sccm) Thruster Pressure Test Comparison at Various Heights .....	128
Figure 69: <i>Fluent</i> Static Pressure Readings in Torr at the Corresponding Heights for the Pressure-Testing Device's Spacer Locations.....	131
Figure 70: Concept Drawing of Integrated Grids in the Thruster Cylinder.....	137
Figure 71: LTCC Thruster and Grids.....	138
Figure 72: Successful Plasma Generation Test for 4 Hole Thruster Design .....	139

Figure 73: BSU Electric Propulsion Thrust Stand.....	150
Figure 74: BSU Electric Propulsion Vacuum Chamber .....	151
Figure 75: Two-Stage Mechanical Vacuum Pump.....	152
Figure 76: Cryogenic Pump and Gate Valve .....	153
Figure 77: Thrust Stand Yoke for Thruster Attachment.....	166
Figure 78: Thrust Stand Adaptor Plate for New Thruster Design .....	167
Figure 79: Gate Valve Displaying Three Valves for Operation (A, B, C) .....	170



## CHAPTER 1: INTRODUCTION AND BACKGROUND

### 1-1 Micro-Satellites

Micro-satellites are continually in development around the world. These satellites are small in size in an effort to reduce the cost of putting a satellite into space and keeping it in orbit. Micro-satellites are advantageous for space missions because of their small size. The cost of materials as well as the cost of fuel is considerably decreased for micro-satellites compared to traditional satellites. These micro-satellites are classified by having a weight of less than 100 kg [1]. With these smaller satellites, additional restrictions are placed on their onboard propulsion systems, which are typically used for attitude control and station-keeping. By decreasing the mass of the satellite, less force is required to propel and maneuver the satellite. These micro-satellites use propulsion systems that are both light in weight and small in size to fit on the satellite. In order to achieve both of these goals, alternative propulsion systems are currently in development such as the solid propellant micro-thruster by Larangot et al. [2] and the chemical combustion system of Hydrogen-Oxygen in platinum tubes by Boyarko et al. [3].

### 1-2 Micro-Propulsion

Micro-satellites need a less conventional propulsion system than the traditional large-scale satellites seen in most space applications since the satellite propellant is mainly used as a method of attitude control and station-keeping. The micro-satellite's rotational inertia is much smaller because of the smaller mass and size of the satellite.

This decrease in rotational inertia requires less thrust for satellite maneuverability.

Micro-satellites have spawned a new distinction of low-thrust and small-scale propulsion known as micro-propulsion. A study by Yashko and Hastings shows a desired thrust for micro-propulsion thrusters as being larger than 1.5  $\mu\text{N}$  per kilogram of satellite mass [4]. Micro-propulsion designs include chemical [5, 6], digital [7], and electrical propulsion [8, 9, 10]. The most common type of propulsion techniques on this scale are electrical propulsion designs, because electric propulsion provides a high mass-utilization efficiency, as well as a large specific impulse [11]. Specific impulse, also known as propellant mass efficiency, is a ratio of thrust to mass flow rate times the gravitational constant as seen in Equation 1.

$$I_{sp} = \frac{T}{\dot{m}g} \quad (1)$$

Where:  $I_{sp}$  is specific impulse (s)

$T$  is thrust (N)

$\dot{m}$  is propellant mass flow rate (kg/s)

$g$  is the gravitational constant in ( $\text{m/s}^2$ )

The thrust in Equation 1 is a function of the propellant mass flow rate and the exit velocity of the propellant,  $v_{ex}$ , as seen in Equation 2.

$$T = \dot{m}v_{ex} \quad (2)$$

Larger specific impulses directly relate to larger thrust for the same amount of fuel consumption. The increase in thrust reduces the amount of fuel needed aboard satellites for station-keeping, and this significantly decreases the mass and size of satellites. Typical specific impulse values from thrusters range anywhere from 50 seconds to 3600 seconds [12]. Electric propulsion boasts some of the highest specific impulses and will be discussed next.

### **1-3 Electric Propulsion**

The energy for thrust with electric propulsion comes from an electric source. The electric source is used to accelerate the propellant away from the thruster body, producing thrust. There are currently multiple configurations of electric thrusters, which include resistojet [8], arcjet [13], electrostatic ion [14], hall [11], field emission [15], pulsed plasma [10], and magnetoplasmadynamic thrusters [16]. Two of the most common electric thrusters are the electrostatic ion thruster and hall thruster. Electrostatic ion thrusters are particularly interesting for micro-propulsion because they create specific impulses at the top end of the specific impulse range mentioned previously [12]. The propulsion for this thruster type is generated by the acceleration of plasma ions away from the thruster body. The electrostatic ion thruster will be examined in greater detail after first examining details on the background of plasma.

#### 1-3.1 Plasma

Solids, liquids, and gases are the most well-known of the states of matter, but another state, called plasma, exists and is the most abundant form of ordinary matter in the known universe [17]. Plasma is essentially a gas that has been elevated to a higher

energy state by heat, an electromagnetic field, or light. Ionization of a gas occurs when free electrons are passed through the gas. The electrons can bombard the gas molecules and disassociate electrons in the outer shell of the neutral gas, creating positively charged gas molecules known as ions. Figure 1 shows plasma created from a plasma ball [18].



**Figure 1: Plasma Created by a Plasma Ball [18]**

Once plasma has been formed, the plasma can be sustained so long as the system power input is sufficient to overcome particle and energy losses. Plasma has many practical applications in devices today from electronic displays [19], plasma cutters [20], and ion thrusters [21]. Plasma ions are able to respond to electrostatic fields, which makes them an ideal source for thrust generation. Positively charged ions will be attracted to negatively charged potentials; thus, the plasma ions will be drawn towards a source of a negative voltage [22]. A magnetic field can keep the plasma electrons confined; these electrons are then available for additional ionization. In addition, the electron loss rate to the walls creates a plasma potential that increases the ion loss rate;

therefore, the lower electron loss rate also decreases the ion loss rate. The net effect is an increase in the plasma density. A larger difference in voltage between the ion and negative voltage source can create additional attraction, which in a thruster produces more thrust. Controlling the plasma efficiently can result in a higher plasma density and, thus, optimal thrust production.

### 1-3.2 Electrostatic Ion Thrusters

An electrostatic ion thruster has three basic systems: the plasma generator, an accelerator, and a neutralizer. The electrostatic ion thruster has the largest typical specific impulse potential with the option of using an inert fuel [11, 12]. Figure 2 shows an ion thruster, 30 cm in diameter, firing at the Jet Propulsion Laboratory [21].

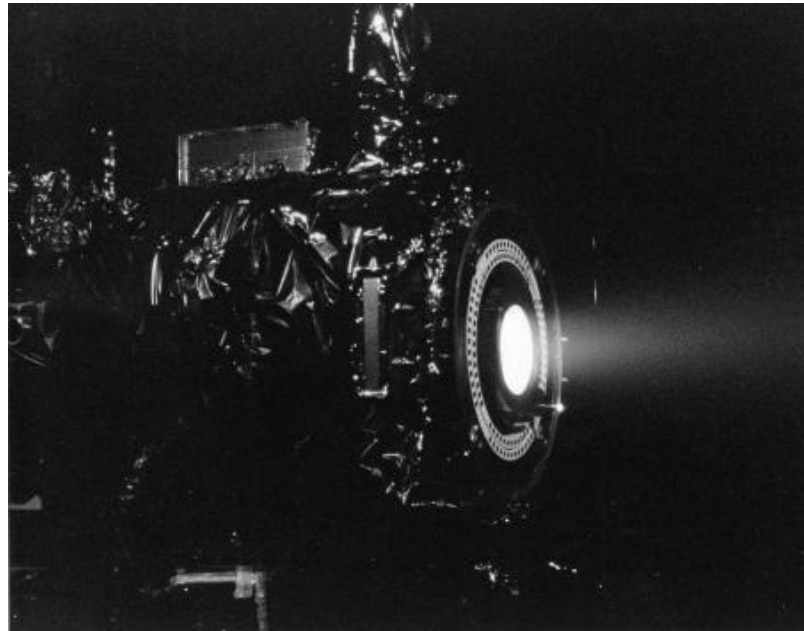


**Figure 2: Electrostatic Ion Thruster Firing at the Jet Propulsion Laboratory [21]**

The plasma generator, a hollow cathode discharge in this case, produces electrons to excite the neutral gas into plasma, as can be seen in Figure 3 [21]. The positive and negative accelerator grids generate a large voltage gradient to attract the plasma ions and expel them from the thruster body. The hollow cathode neutralizer at the top of the figure neutralizes the exiting ions [12]. Ideally, the best chemically stable fuel to use for these thrusters is xenon as it is the heaviest non-radioactive noble gas [21, 23]. Argon can be used in place of xenon in experimental testing due to its lower cost and availability [14].

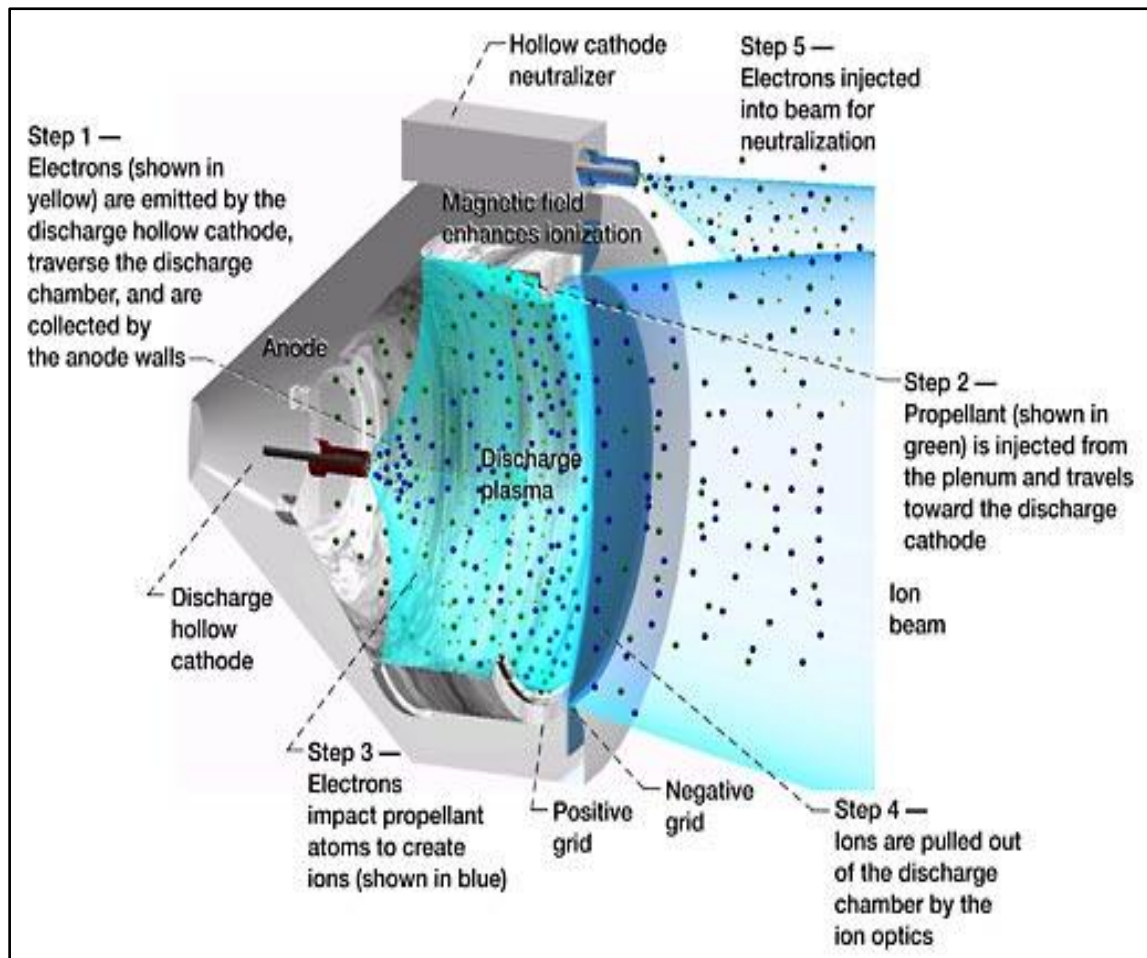


Figure 3: NASA Ion Engine Diagram [21]

## **1-4 Materials Systems Used for Miniature Electric Propulsion Thrusters**

### 1-4.1 Typical Material Used in Creation of Micro-Thrusters

Miniature electric propulsion systems are difficult to fabricate due to the small component size required for these systems. Silicon is used frequently with small-scale thrusters [7, 24, 25]. Silicon is able to provide small componentry for miniature thrusters, but has limits with fabrication techniques as thrusters developed using silicon are generally planar in nature. Silicon devices can be created with basic Micro Electro-Mechanical Systems (MEMS) techniques such as photolithography, micro milling, and Deep Reactive Ion Etching (DRIE) [26]. The silicon devices use a single layer of the silicon for electrical and fluidic connections and require protective layers for exposed electrical traces and seals for the fluidic channels. This fabrication approach is undesirable as complex electrical and fluid delivery systems may be required for these thrusters.

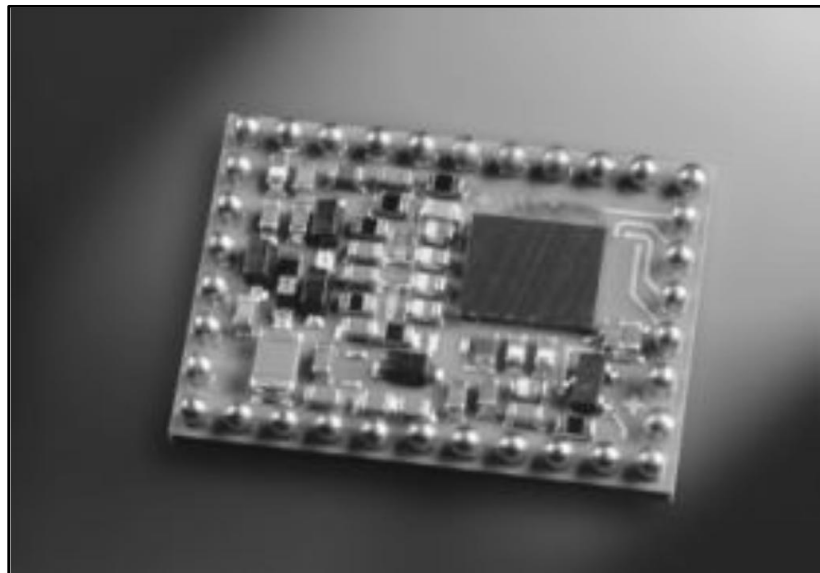
A better material system is needed for development of micro-thrusters that can provide the ability to deviate from planar designs for complex electrical circuit elements and fluidic channels. This material system will also require plasma erosion resistance for long-term use and for the ability to create hermetic seals for the fluid delivery through the thruster.

### 1-4.2 Low Temperature Co-Fired Ceramic Material

Low Temperature Co-Fired Ceramic (LTCC) in its “green” (unfired) state is comprised of a matrix of alumina, glass frit, and organic binder. LTCC comes in thin sheets that can be stacked and laminated to create a ceramic device. Prior to being

stacked and laminated, the LTCC layers can be routed and printed with conductive pastes to create embedded electrical and fluidic features. Embedded passive electronic components such as electrical conductors, inductors, capacitors, as well as resistors, can all be created with the specially formulated metal pastes. LTCC allows vertical integration by stacking layers and is an integral part of making electronic devices smaller and more compact.

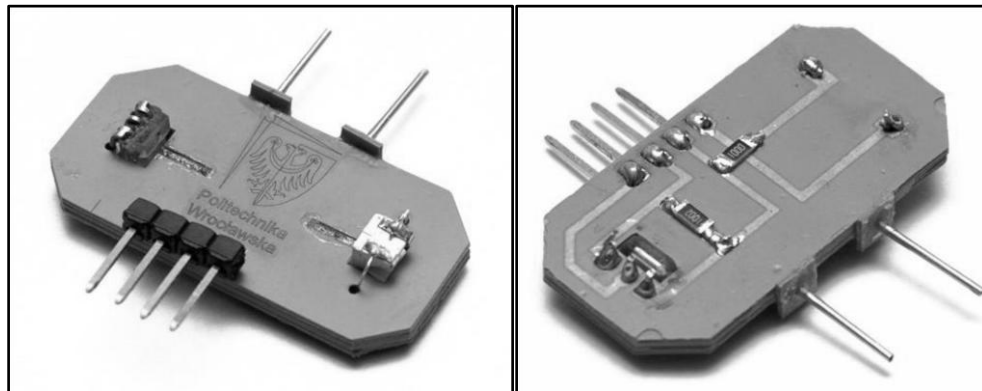
The excellent electrical characteristics of being a stable dielectric, having a low loss tangent, containing integrated passive components, and having a high circuit density (multi-layer capability) make LTCC a great choice for electrical devices [27]. LTCC has been effectively used in wireless applications such as Bluetooth Module communication [28]. Bluetooth devices are very small wireless devices that communicate using short-wavelength radio transmissions. The telecommunications vendor, Ericsson, created Bluetooth in the mid-1990s and an example of their LTCC module is shown in Figure 4. This module is 10.2 mm wide, 14.0 mm long, and 1.66 mm thick.



**Figure 4: Bluetooth Radio Module (10.2 mm x 14.0 mm x 1.66 mm) [28]**



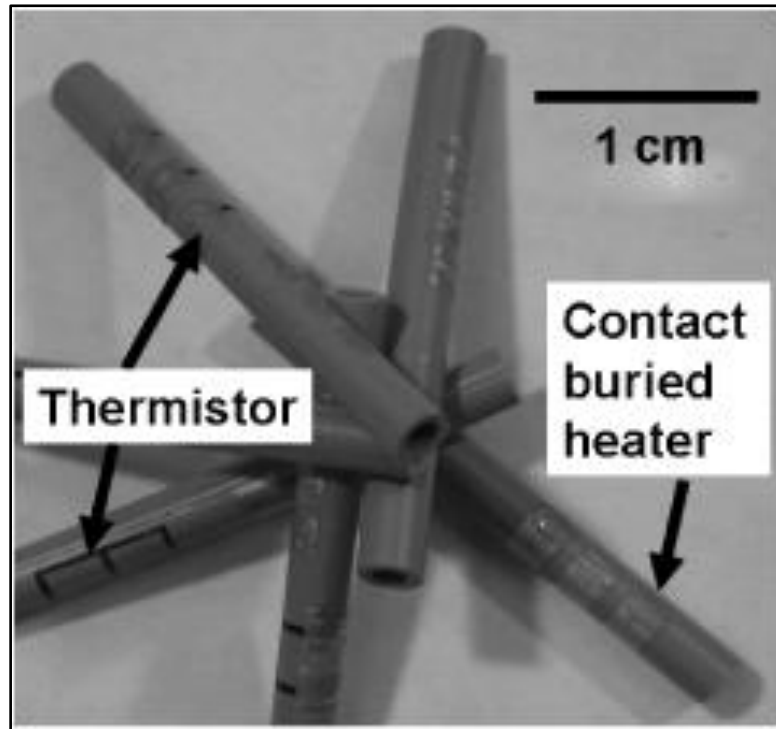
LTCCs benefits of being highly workable in the “green” state, having a high mechanical strength in the fired state with multi-layer structures, and having hermetic seal capabilities make it an excellent choice for devices, mechanically. These mechanical benefits can be combined with electronics in the same substrate to make microfluidic devices with integrated electronics such as the optical absorbance ceramic structure created and tested in Poland [29]. The device was used to perform a chemical analysis on distilled water containing heavy metals using optoelectronic components. The overall device size was approximately 2 cm wide, 3.5 cm long, and 2 mm thick (excluding external components). The fluid flow channels were 150 microns wide at their smallest locations and had a maximum fluid flow of approximately 0.7 mm/s. Both sides of the small device can be seen in Figure 5.



**Figure 5: Microfluidic Chemical Analysis Device (2 cm x 3.5 cm x 2 mm) [29]**

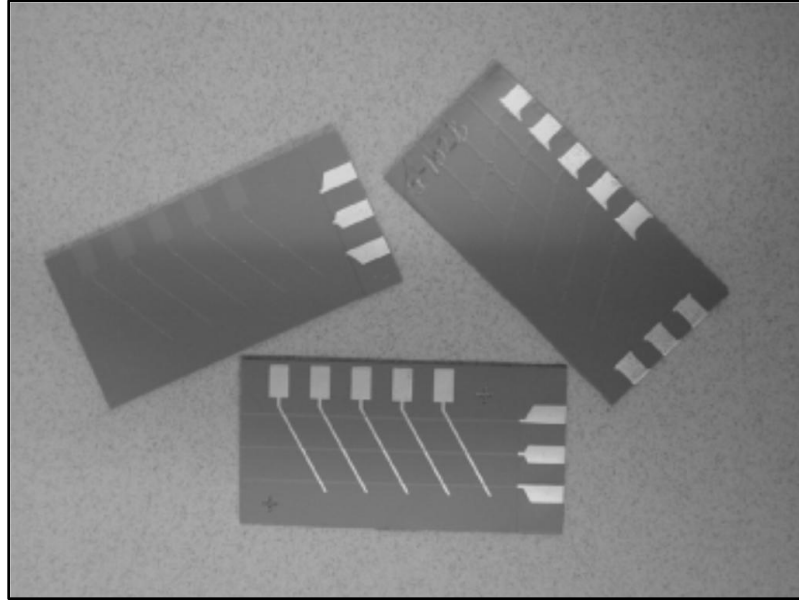
Non-planar designs have been realized in LTCC as a result of the flexible fabrication process. Rolled structures have been demonstrated in LTCC [30]. These structures can be used to create devices such as the ion mobility spectrometers seen in

Figure 6. These spectrometers demonstrated that LTCC can successfully be rolled into cylindrical shapes and include features such as thermistors and contact heaters, which demonstrates new fabrication approaches for LTCC device design.



**Figure 6: LTCC Heated Tubes with Thermistors [30]**

LTCC also has the ability to withstand the harsh environment created by high temperatures produced during plasma generation [31]. Micro-plasma devices were made and tested that underwent continuous plasma generation and can be seen in Figure 7. The tests proved that the LTCC was able to handle 100 hours of uninterrupted plasma generation with no negative effects to the LTCC.



**Figure 7: LTCC Micro-Plasma Generation Devices (Size Not Reported) [31]**

The electrical and mechanical benefits of LTCC make it a good material choice for many systems. These benefits directly apply to micro-thrusters created in LTCC. A thruster created with LTCC can have embedded miniature electrical and fluid pathways ( $< 1$  mm), which would make the thruster smaller and lighter. The ability to generate plasma with these electrical and fluidic components within an LTCC body that resists the harsh effects of plasma makes LTCC a good choice for electric propulsion.

### **1-5 Electric Propulsion at Boise State University**

A thruster is currently in development at Boise State University (BSU) that could produce enough thrust to control a micro-satellite in space in an effort to maintain attitude as well as for station-keeping. A concept drawing of a micro-satellite is shown in Figure 8. This satellite is proposed to be 40 kg in weight and 40 cm in length on each side.

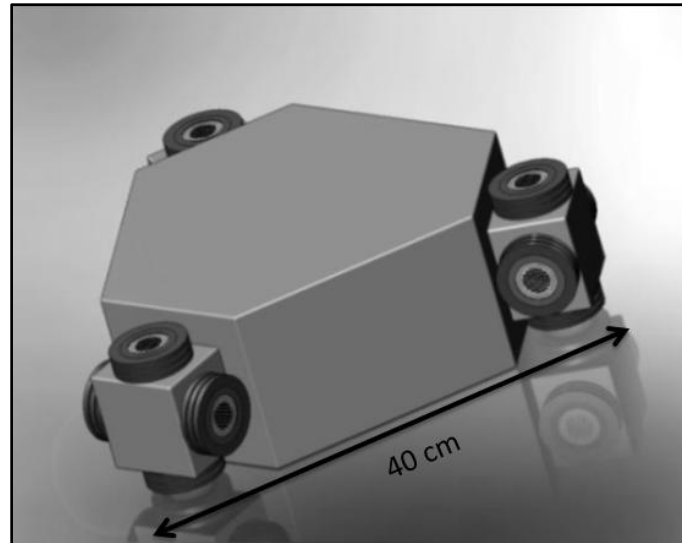


**Figure 8: BSU Electric Propulsion Project Concept Micro-Satellite Drawing**

This satellite has twelve miniature thrusters with an approximate outer diameter of six centimeters each, including the ring magnets. The inner diameter of each thruster is 2 centimeters.

The BSU electric propulsion team is a multi-disciplinary engineering group that has been working on a miniature electrostatic inductively coupled plasma (ICP) thruster [32, 33]. Inductively coupled plasma thrusters are able to operate with very low neutral gas pressures. The inductively coupled plasma generator source uses a planar spiral antenna with a signal from a radio frequency amplifier. The alternating current input provided from the amplifier and power source produces a time-varying electromagnetic field. The electromagnetic induction creates plasma from the base molecules of an inert gas [34]. The positive plasma ions are then extracted from the thruster body with a voltage gradient generated by electrostatic grids. The extraction of ions at high velocity creates a thrust to move a spacecraft the opposing direction due to Newton's third law of

motion. The process of converting the gas to plasma and extracting the ions creates a high specific impulse by developing high ion exhaust velocities. The high ion velocities combined with a low mass flow rate allow for less fuel needed aboard the satellite relative to chemical propulsion. For an assumed one axis 30° rotation of this concept satellite design in 180 seconds, a kinematic analysis was performed that assumed three out of the twelve thrusters firing to make this move. In the 180 seconds, an initial impulse and restorative impulse would be performed. The analysis resulted in each thruster having an operating range of 200  $\mu\text{N}$  of thrust.

The concept thruster for the BSU Electric Propulsion group, which can be seen in Figure 9, has a gas inlet into the center of the antenna, which is centered within the base of the thruster cylinder. The goal of the group is to develop an integrated micro-propulsion device using LTCC that is resistant to harsh plasma environments. The thruster body could be surrounded by several ring magnets, which aid in the efficiency of the plasma generation by confining electrons within the cylinder. At the end of the thruster body are two electrical grids that extract the ions from the thruster. The screen grid has a charge near ground that attracts the positive ions, creating a flow of plasma out of the cylinder. The accelerator grid then expels the ions due to its large negative charge.

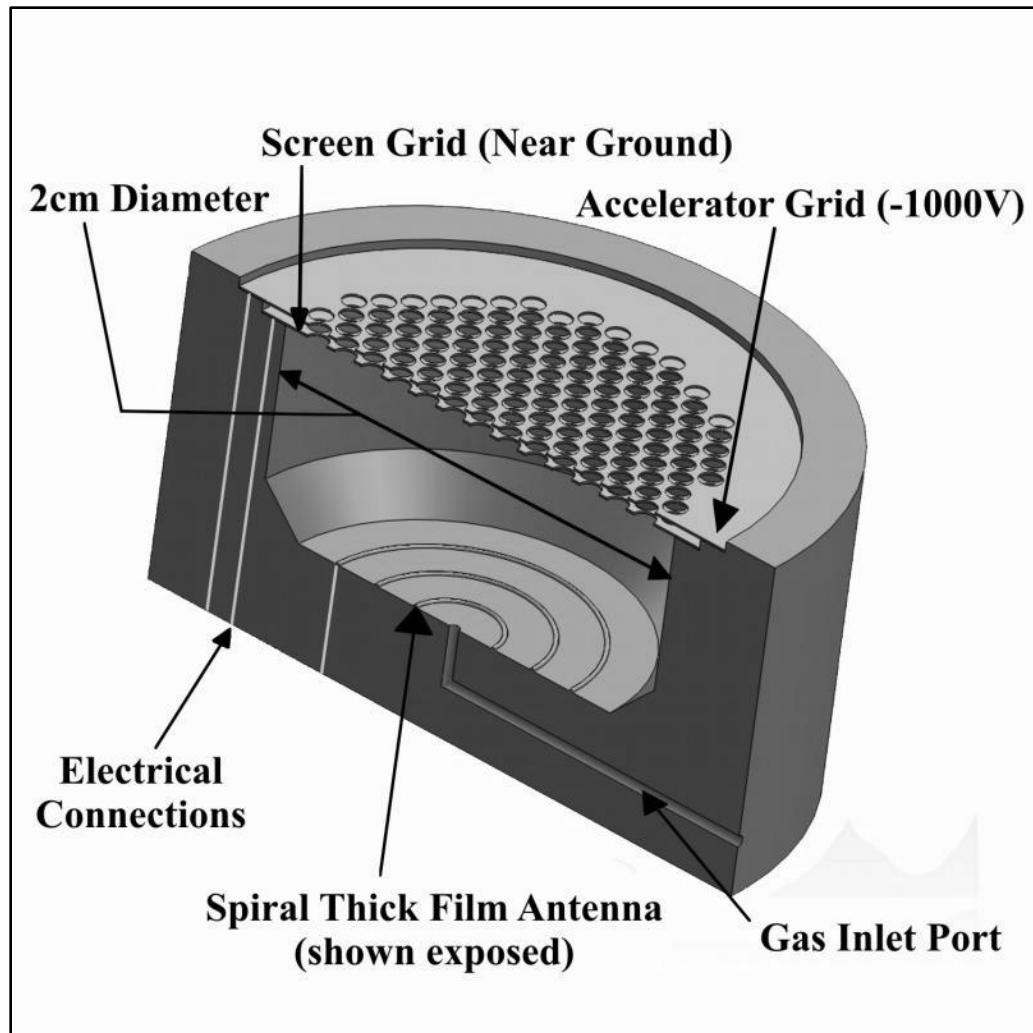


**Figure 9: BSU Electric Propulsion Project Concept Thruster**

The purpose of the research related to this thesis is to optimize the propellant delivery system inside the thruster used in the BSU electric propulsion project; this optimization will reduce the mass of propellant required onboard the satellite. This goal of optimization will be attained by creating a gas flow delivery apparatus for experimental testing as well as creating a unique thruster body out of LTCC that incorporates fluidic channels within the substrate. This task is unique in that the BSU team is using LTCC to fabricate the entire thruster system. For testing, a variable flow

rate system was created for this project that incorporates multiple mass flow controllers to cover a broad range of gas flows with high accuracy. This multi-range system will provide experimental flow control covering ranges from below 1 standard cubic centimeter per minute (sccm) up to several hundred sccm. A sccm is a method of providing a standardized mass flow rate from a volumetric flow rate of a gas based on its density at standard pressure and a standard temperature.

The details of design and fabrication of the thruster and the internal propellant delivery system are discussed in this thesis as well as results from experimental pressure testing of the thruster. The spiral antenna dimensions as well as the thruster containment cylinder dimensions were already designed at the onset of the research for this thesis, but the rest of the thruster dimensions were designed as part of the research for this thesis.

### **1-6 Propellant Delivery in Miniature Electric Propulsion Thrusters**

In order to better understand the operations of a propellant delivery system for a miniature electric propulsion thruster, it is important to review current systems in use. A propellant delivery system is an essential part to a successful electric propulsion thruster. The main function of the propellant delivery system is to provide a precise amount of propellant from a pressurized tank on the satellite into the thruster plasma generation region. Factors of concern for the propellant delivery system are the localized pressure entering the thruster cylinder, the type of propellant, and the mass flow rate of the propellant. This section will review multiple designs for these systems to estimate mass flow rates and thrust capabilities for micro-propulsion thrusters. Propellant distribution of the thrusters is also noted for comparison.

Holt et al. at the University of Texas at Austin created a microdischarge plasma thruster that used a single micro-valve that leads to a microdischarge chamber [35]. This chamber is injected with xenon that will be ionized and channeled through a converging-diverging micro-nozzle, increasing the velocity of the plasma to 4.5 times the speed of sound in xenon. This thruster utilized a mass flow rate of 0.015 kg/s and produced a 10 N thrust force used for station-keeping. This thruster provides a low specific impulse of approximately 68 seconds. The thruster nozzle is made of an unspecified dielectric material. The pressure seen inside the thruster is 1 atm of xenon gas, which is quite large and could result in a low specific impulse as the gas may not be fully ionized prior to discharge.

A miniaturized cylinder Hall electric propulsion thruster from Smirnov et al. at Princeton University used a Boron Nitride ceramic channel for propellant routing and distribution [36]. A mass flow rate of  $0.4 \times 10^{-6}$  kg/s of xenon was used to produce a specific impulse of approximately 1250 seconds (at 110 W), which translates to approximately 5 mN of thrust. Smirnov's thruster has a larger specific impulse than Holt's and requires a lower propellant mass flow rate into the thruster. Smirnov's thruster produced a maximum thrust of up to 12 mN, but required 300 V of discharge voltage (approximately 320 W of discharge power). The efficiencies of Smirnov et al.'s thruster ranged from 14% to 33%, but this efficiency only took into account the gas at the anode injection area. Pressure of the neutral gas inside the containment cylinder was not recorded in the paper.

A third propellant delivery system by Surrey Satellite Technology, Ltd., incorporated a resistojet thruster [37]. The propellant system had a wet mass (system



mass with fuel included) of 7.22 kg using xenon gas. The thrust provided using a variety of propellants was 20 to 50 mN. Xenon was used as a propellant and produced a specific impulse of 42 seconds at 300°C. Four cool gas generators were used to maintain a gas supply temperature of 300°C. This delivery system used a series of solenoid valves to isolate the propellant in the storage tank. The pressure sent to the thruster is regulated by a control that continually opens and closes the valves until the desired pressure is reached. Additional information about mass flow rate, bang-bang frequency, or required pressure for the thruster was not provided. This propellant delivery system and thruster also has a relatively small specific impulse. The materials in this system were mostly comprised of metals.

A final propellant delivery system for a micro-discharge microarcjet thruster by Slough and Ewing was reviewed [13]. Slough and Ewing's system used Argon gas as the propellant with a mass flow rate of  $2 \times 10^{-6}$  kg/s. The pressure upstream from the nozzle ranged between 10 and 20 kPa (75 and 150 Torr). A 5 W discharge power resulted in 1.1 to 1.8 mN of thrust with a specific impulse of 90 seconds. The highest efficiencies seen by this system were around 40%. This system utilized a 300 micron flow channel diameter at the throat of the propellant delivery system. The thruster in this system had a combined material system that incorporated a macor ceramic with a pyrex gas feed tube. The macor had to be machined to allow the electrode and gas to pass through the center. This thruster had multiple interfaces between materials and used two separate pieces of macor for separate thruster bodies. The application of multiple materials and multiple sealing points is not desirable in thrusters as the opportunity for gas leaks is larger with multiple seals between materials.

Three of the four systems had thrusters that provided thrust in the mN range. These systems used ceramic, metal, or silicon for propellant delivery to the thruster. These materials are all able to be machined, but lack the ability to have complex integrated fluidic channels without using additional sealing mechanisms such as O-rings between adjoining pieces of material. These materials also have limited capabilities with electrical connections. The connections require straight through holes or external attachment points. These wires also require protective coating to avoid conduction to thruster materials. These systems had a variety of mass flow rates between  $2 \times 10^{-6}$  kg/s and 0.015 kg/s, which produced thrust in the range of 1.1 mN to 10 N. The smaller satellites of these four systems required less thrust, which also required a smaller mass flow rate. A material system that allows internal distribution of the propellant would increase the efficiency of the propulsion system by producing localized pressure as well as limiting the complexity of interfacing components.

### 1-7 Thesis Overview

With the modern era of micro-satellites becoming more prevalent, micro-propulsion systems are increasingly necessary. Micro-propulsion systems to date are reliant on extensive internal sealing surfaces or external propellant distribution. These systems also tend to have planar fluid and electrical features. This thesis combines the two worlds of the LTCC material system and micro-propulsion to alleviate some of the limitations as well as decrease the size of propellant delivery systems.

This thesis will present, in Chapter 2, how the LTCC material system is used in the Ceramic Micro Electro-Mechanical Systems (C-MEMS) laboratory at Boise State University. Chapter 3 will present the design of the propellant delivery system for the

thruster as well as the optimization of the thruster body itself to use less propellant (neutral gas) when producing thrust by maximizing ionization efficiency. The design of a Computational Fluid Dynamics (CFD) model incorporating various fluid flow theories will be presented in Chapter 4. The fabrication process will be shown in Chapter 5, which includes the development of the thruster as a solid model and the iterative process required to optimize the fabrication techniques for this specific design. This thesis will also cover experimental pressure testing of the thruster in a vacuum chamber simulating space conditions in Chapter 6. The experimental data will be compared to the CFD model that can be used in the future to further improve the design of the gas injection locations of the thruster. This CFD model should aid in development by decreasing the need to fabricate all iterations of any future proposed designs. A final thruster design will be produced that will undergo future testing with an active plasma source. Significance of the final design and results will be presented in Chapter 6, as well as conclusions drawn from the work done for this thesis in Chapter 7.

## CHAPTER 2: LOW TEMPERATURE CO-FIRED CERAMIC

This chapter will demonstrate examples of LTCC devices created at the C-MEMS laboratory. An overview of the LTCC device process will then be described, detailing the design process as well as the fabrication of LTCC devices. Lastly, a list of lab materials and equipment used in device fabrication will be provided.

### 2-1 LTCC at Boise State University

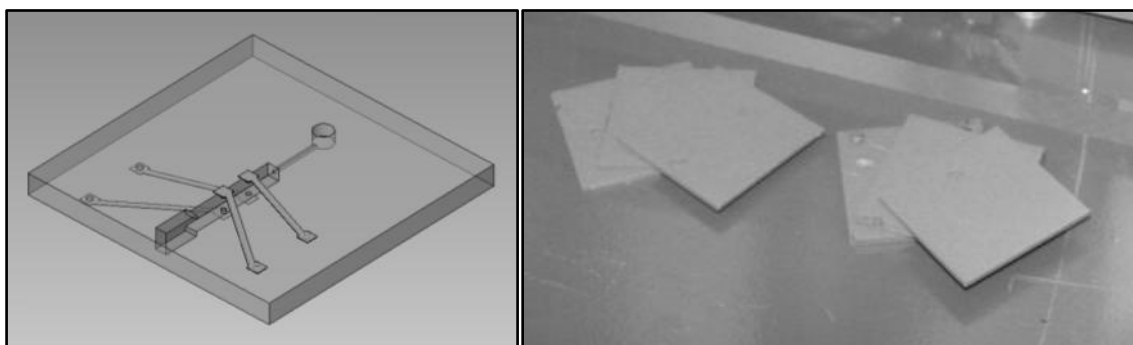
Prior to presenting examples of LTCC devices at BSU, a few important details will be presented. The LTCC used at Boise State University is provided by DuPont in the “green” or unfired state. The organic binding element in the LTCC allows it to be pliable while it is cut and manipulated. LTCC in this state can be cut with great precision down to +/- 0.1 mm with a laser-milling machine. Metallic pastes can also be printed on the layers of LTCC to create the electrical conductor networks throughout the LTCC body. The individual layers can then be stacked and the openings cut in the stacked layers are used as fluid flow channels. The stacked layers of LTCC are laminated and then finally fired.

During a proper firing profile, the LTCC is heated at nearly 3°C per minute to allow for the binder to burn out and then the glass begins to flow through the matrix. An initial dwell occurs at 360°C, which allows for the LTCC to reach an even heat throughout the part and burn off the organic binder. The temperature is ramped again at 2°C per minute until an additional dwell at 860°C. This temperature allows for the

liquid phase sintering process to proceed. Liquid phase sintering occurs when the glass frit softens and begins to flow, which encapsulates the alumina grains. During the sintering process, the LTCC densifies, causing the substrate to shrink by approximately 13% in both the lateral directions and 15% in the height of the LTCC structure [38]. Once fired, LTCC creates a hermetically sealed device, which can withstand harsh environments. The fired LTCC takes on the characteristics of being vacuum compatible and resistant to temperatures less than the sintering temperature of 860°C. It is also a dielectric material with a stable dielectric constant of 7.8 over frequencies up to 1 GHz.

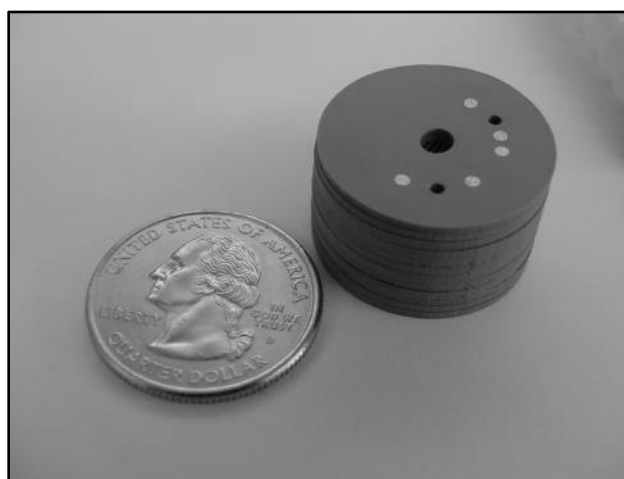
Several LTCC devices have been developed at Boise State University's C-MEMS laboratory, including a micro-combustor [39] and an ion mobility spectrometer [27].

Figure 10 shows the design concept of the micro-combustor (left) and the final fabricated devices (right). The micro-combustor was approximately 4 cm in length and was designed as a mobile power generation device using the combustion of hydrogen and air in a micro-channel as an energy source. This device demonstrated the operation of high temperature fluidic channels embedded in an LTCC substrate. The substrate was exposed to long-term surface temperatures in excess of 250°C.



**Figure 10: Micro-Combustor Concept in LTCC (Left) and Six Final Devices (Right). Successful high-temperature operation of embedded fluidic channels in LTCC [39].**

Figure 11 shows an Ion Mobility Spectrometer in LTCC created in the C-MEMS laboratory. This sensor device was used to determine chemical species that are present in a sample of gas by measuring the time of flight of unknown sample ions. This device demonstrated high multilayer LTCC structures (>100 layers) with embedded electrical conductors and resistors.



**Figure 11: Miniature Ion Mobility Spectrometer Sensor in LTCC. All of the sensor electrical components are embedded in the ceramic substrate [27].**

## 2-2 Overview of the BSU C-MEMS LTCC Fabrication Process

The design and fabrication process listed in this section is the standard BSU C-MEMS process [40] and was originally derived from the fabrication instructions provided by DuPont [41]. Figure 12 shows the typical manufacturing process for LTCC devices. This process was developed to produce three dimensional features in the LTCC substrate and circuit elements.

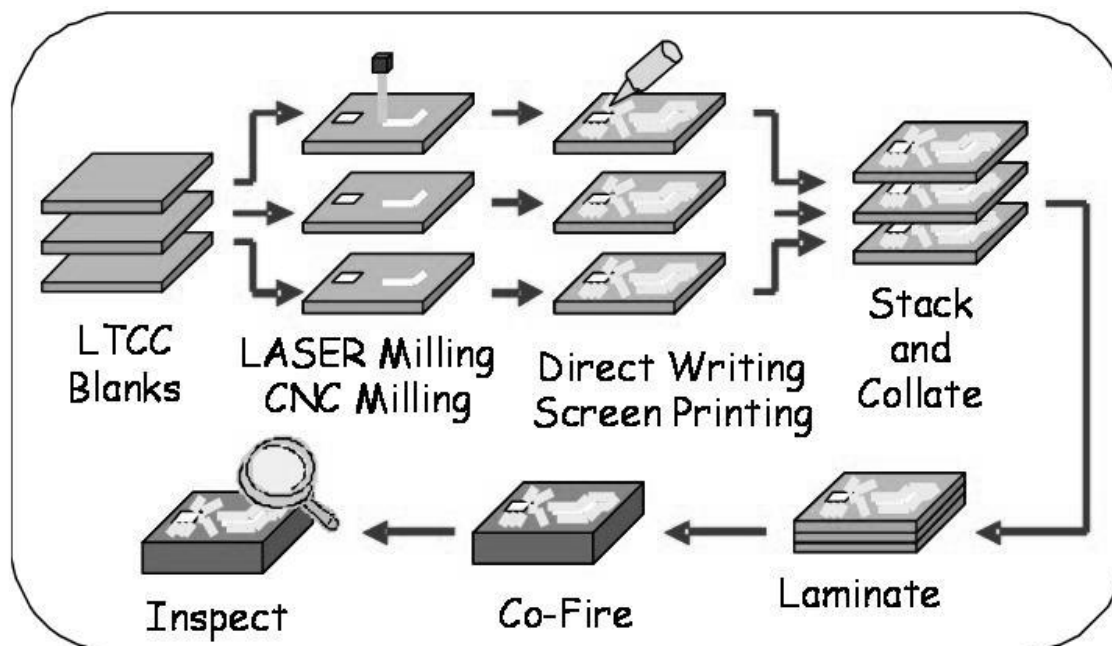


**Figure 12: LTCC Manufacturing Process and Flow [40]**

Initially, a device is designed in *SolidWorks* that incorporates all the via (vertical electrical connection) holes, electrical traces, and internal cavities as a single part. The part is then split into individual sections representing each individual layer of LTCC. Each of these parts is saved as a DXF file, which is imported to *CorelDraw*. The DXF files consist of patterns created by lines that describe the part geometry. Once imported into *CorelDraw*, these parts are used to create stencil files for screen printing and LTCC layer geometry files. The stencil files are used as “screens” for printing electrical components onto the surface of the LTCC.

To begin LTCC fabrication, features such as fluidic cavities, vias, alignment holes, and part boundaries are cut into the blank “green” LTCC sheets from the LTCC files. A CNC laser-milling machine, which makes precise cuts in the LTCC substrate as

small as 0.1 mm, is used to fabricate layer patterns. This minimum feature size is based on the focal point spot size of the laser.

Once the features have been cut into the “green” LTCC sheets, the conductive pastes for electrical pathways and carbon for fluidic channel integrity can be applied to the substrate. The electrical traces can be applied to the LTCC by a screen printer, or manually with screens or stencils. The screen is placed over the LTCC sheet and a squeegee with the paste is pulled across the screen, applying the paste uniformly to the substrate. Thin sheets of carbon are also cut with the laser and then carefully placed into the internal cavities of the device. The carbon is used as a sacrificial material to preserve the shape of the cavity during pressing and firing by burning out after the LTCC has started its initial sintering process.

When the electrical component pastes have dried, the layers of LTCC are collated and laminated in a uniaxial lamination press. The lamination of the LTCC occurs by applying 20.68 MPa (3000 psi) of pressure at 70°C for 10 minutes. If the geometry of specific parts is difficult to laminate with a lamination fixture and the press, Poly-2-ethyloxazoline (PEOX) can be used between layers with a light pressure to bond the layers. If rolled LTCC structures are desired, an isostatic lamination press can be used with the same settings as the uniaxial press. A dowel rod is needed for lamination of rolled structures to preserve internal cavities [42].

After lamination, a final inspection is made and the device is then placed in a programmable box furnace. The firing process creates a dense material structure that contains embedded electrical and fluidic components. The metallic pastes co-fire within the ceramic substrate to create a single integrated structure.



A variety of post-firing materials are available for device post processing. To connect the device to external electrical sources, silver epoxy can be used as well as pastes for soldering electrical wires to the device substrate. A ceramic epoxy can also be used as an adhesive material for attaching metal tubing and other components. Brazing paste may also be used to attach metal fittings with a secure connection that can reach higher temperatures than connections using solder or epoxy.

Green LTCC sheets can be ordered in a variety of lengths and thicknesses. The main thickness of LTCC used in this project is the 0.254 mm thick sheet, which is classified as 951PX by DuPont. Standard unfired LTCC sheet thicknesses in the C-MEMS laboratory are 0.051 mm (951C2), 0.114 mm (951PT), and 0.254 mm (951PX). These sheets normally come in 152.4 mm or 203.2 mm square sheets, which allow for large device fabrication.

### **2-3 C-MEMS Lab Material and Equipment List**

This section of the chapter details in two tables the materials and mechanical equipment needed in the fabrication of these thrusters in the LTCC materials system. The materials, seen in Table 1, are used while working with LTCC at the BSU C-MEMS laboratory, and the equipment needed for thruster fabrication can be seen in Table 2.

**Table 1: Materials List for Thruster Fabrication**

<b>Materials</b>	<b>Description/Part#</b>	<b>Brand</b>
LTCC Tape	951 PX, 951 C2	DuPont
Conductor Paste	6141, 6145	DuPont
Carbon Tape	TCS-CARB-1	Thin Film Technologies
Silver Conductive Epoxy	8331-146	MG Chemicals
Ceramic Epoxy	Hysol 1C	LOCTITE
PEOX	372846	Aldrich

**Table 2: Equipment List for Thruster Fabrication**

<b>Equipment</b>	<b>Description/Part#</b>	<b>Brand</b>
Uniaxial Lamination Press	20-Ton	PHI
Isostatic Lamination Press	ILS-66S	KEKO
Laser-Milling Machine	30 Watt	Universal Laser Systems
Furnace	M Box Furnace	Lindberg/Blue

Using the LTCC material system in the design of the thruster body makes sense because of the benefits the LTCC provides for an electric micro-thruster. The material system allows for small features ( $< 1$  mm), which is ideal for micro-propulsion. The material also has benefits for a vacuum environment as well as a plasma environment such as low out-gassing and resistance to ion degradation. The LTCC can incorporate embedded fluidic and electrical components that reduce the size of the thruster as well as the interface with external components. The next chapter will discuss the design process of the thruster propellant delivery system and electrical conductors within the LTCC substrate.

## CHAPTER 3: DESIGN PROCESS

The design of the propellant (Argon gas) delivery system has been split into multiple sections including the previous thruster design, the initial requirements and limitations, the previous design evaluations, and the design of the thruster for this research, which will be referred to as Version 1. Future design iterations beyond the first version of the thruster were developed during the fabrication process and will be discussed in Chapter 5 with an iterative approach.

### **3-1 Initial Thruster Concept**

An initial concept of the thruster will be described in this section. Figure 13 displays the components of the concept. These components are the thruster containment cylinder, radio frequency (RF) antenna, SubMiniature version A (SMA) connector, gas fitting, and the thruster base. The thruster base will be the attachment interface for the SMA connector and the gas fitting. These two items are the control inputs to the thruster for electrical and gas flow. The side of the thruster base where the control inputs are attached will be known as the thruster control interface side as shown in Figure 13, for later descriptions of the components.

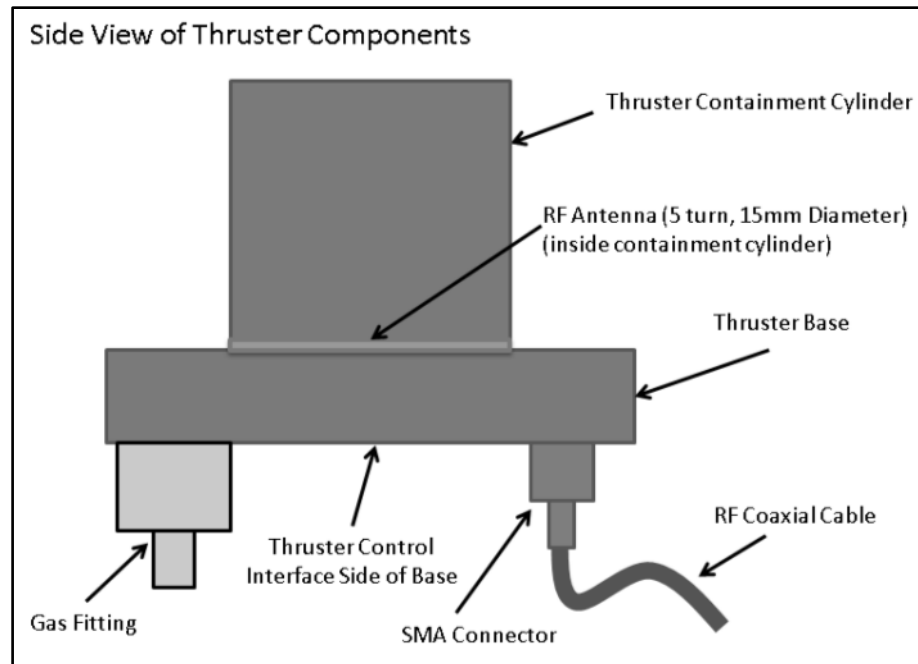


**Figure 13: Side View of Concept Thruster Detailing Components**

### 3-2 Previous Prototype Thruster Design

The previous prototype thruster used to verify antenna performance included an LTCC thruster base seated on an aluminum plate. The aluminum plate had a machined reservoir fitted with an O-ring seal. The antenna base was created with an additional spacer that created separation between the antenna and the gas reservoir to avoid backlighting plasma. The antenna and spacer combo was then held against the aluminum plate with machine screws, which created the seal with the O-ring. The plasma is started by supplying the antenna with a desired frequency, causing an electric field. When the localized pressure of the gas is large enough and the RF power high enough, plasma can be generated and sustained. This design was created in *SolidWorks* and can be seen in Figure 14.

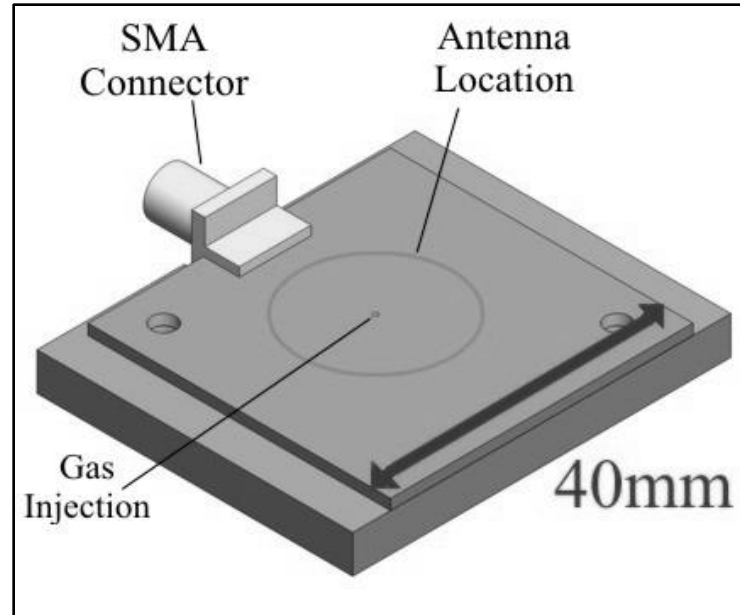


**Figure 14: Single Injection Hole Thruster Design with LTCC Spacer and Reservoir**

This design had troubles lighting plasma at lower pressures similar to pressures in space. The plasma would not strike until a background pressure of at least 10 mTorr was reached inside the vacuum chamber. The single gas injection hole did not appear to create a large enough ambient pressure relative to the antenna for plasma generation at lower background pressures. This pressure concern generated the need for a better design of the propellant delivery system. Table 3 shows the power required to initiate plasma generation as a function of the background chamber pressure and frequency of the RF signal. The table demonstrates how the lower pressures were not allowing plasma initiation unless a high RF input power was used [33]. The empty table cells represent unsuccessful plasma generation. This prototype thruster helped the development of many of the design requirements for the Version 1 thruster described in this thesis. The design requirements can be seen in the next section.

**Table 3: Required Power to Generate Plasma as a Function of Background Chamber Pressure and Antenna Signal Frequency [33]**

Frequency (MHz)	Start Power (W)					
	Pressure (mTorr)					
	10	50	100	200	500	1000
481.4			47	30	18	18.4
548.5			32	15	16.5	19
615.7			37	26	18.5	20
636.8					50	
685.5			45	18	14.4	18.2
752.2			50	22	11	13
818.7	50	50	49	15	7.5	7.7
909.5	50	50	42	6.3	3.2	3
935.7			32	6.2	2.8	2.6
998.9			50	17	6.1	5.2

### 3-3 Design Concerns and Limitations

There were a number of concerns and limitations that were considered during the design process. These concerns helped form the requirements of the thruster and were used to direct the design of the thruster. A brief summary of these concerns and limitations are displayed in Table 4 with a more detailed explanation of the reasoning behind these selections located after the table.

**Table 4: Summary of Thruster Design Concerns and Limitations and Derived Requirements**

Design Concerns and Limitations	Design Requirements
Integrate and Miniaturize Thruster Systems	Thruster Created out of LTCC Material System
Limit Fluid Substrate Interfaces	Fluid Delivery Integration into LTCC Substrate
Edge Mount SMA Connector Limiting Electrical Access	Incorporate a Surface Mount SMA Connector
Thruster Control Interface Should be Placed to Internally Isolate Connections in Satellite	Back of Thruster Base Contains the Control Interface for Satellite Integration
Minimize Metal Interface Components in Antenna Region, Avoiding Electric Field Distortion	Avoid Placing Metal Fittings on Back of Thruster Behind Antenna
Glow Discharge of External Metal Objects	Limit Metal on External Thruster Surfaces
Plasma Generation Limited to Inside of Containment Cylinder	No Large Internal Fluid Reservoirs Under Antenna Region
Sufficient Ambient Neutral Gas Pressure for Plasma Generation	Cylinder Pressure has to be Large Enough for Plasma Generation
Limit Out-gassing	Use Vacuum Compatible Materials and Devices
Cylinder Size Must Accommodate Antenna	Cylinder Must be Larger than Antenna

The primary concerns for this thruster were that the thruster systems needed to be integrated and miniaturized. Using the LTCC materials system would accomplish these concerns as the material system can address both of them. The thruster systems include the thruster base, antenna disc, and the thruster containment cylinder. A fully integrated LTCC thruster decreases the size and complexity of a thruster by removing many interfacing boundaries between materials, which was a concern for thruster gas leakage. In addition, the fluid channels and electrical pathways could be incorporated into the part

with the LTCC materials system. The hermetic ceramic substrate will be used to provide effective propellant flow throughout the thruster system.

The thruster control interface on the outside of the thruster would include the metal gas fitting as well as the metal electrical connection. The thruster control interface is required to be on the back side of the thruster to provide a single fluidic and electrical control interface that can be isolated inside the satellite structure. The previous prototype design used the edge-mount SMA connector mounted on the edge of the ceramic thruster base. This connector connects the thruster ICP antenna to a coaxial RF cable that delivers the input power from an external amplifier. The coaxial cable is rated above 1 GHz, which is within the maximum antenna operating frequency of 1 GHz. The edge connection created a size limitation of 7 layers for the thruster base design, because of the gap between the connector prongs that allowed it to fit over an edge of a device. The number of layers limited the ability to embed internal propellant channels and additional shielding dielectric material on the base of the thruster. Moving the SMA connector to a surface mount device on the back side of the thruster would address both of these design constraints.

Metal components located in electric field regions on the control interface side had proven with previous designs to affect the electric field by changing the electric field pattern. The metal gas fitting and electrical connector had to avoid being placed directly behind the antenna on the control interface side of the thruster base as metal in that region could alter the antenna's electric field.

Fastening the gas fitting securely to the thruster with a leak-free seal was a concern as a leak would limit the gas pressure and ultimately reduce thruster



functionality. A ceramic epoxy was selected as a sealing method for the gas fitting to the LTCC body while ceramic brazing options were evaluated for future iterations. The connection of the SMA connector to the thruster also had to be secure to avoid loss of conductivity by disconnection. A silver epoxy was planned for making the electrical connection to the thruster and a ceramic epoxy would be used for structural support of the RF connector.

Plasma generation inside the gas channels could prevent effective plasma formation inside the cylinder. Therefore, plasma generation within the LTCC cavities should be avoided, and the creation of large gas reservoirs within the LTCC base beneath the antenna should be considered an inadequate design for fluid handling. Sufficient neutral gas pressure local to the antenna inside the thruster cylinder is required for successful plasma generation. The neutral gas molecules should be sufficiently dense for electrons in the containment cylinder to collide with the gas molecules, creating ions; therefore, the gas inlets into the thruster must create a high gas pressure near the base of the thruster cylinder in relation to the ambient vacuum pressure in the chamber. A relationship of pressure required to strike plasma based on a collisional probability of electrons with gas molecules is presented in Chapter 6. This relationship demonstrates pressure requirements of the thruster.

Out-gassing in a vacuum is the process of trapped gases slowly migrating out from within closed locations or materials due to a pressure differential. This process can limit the capability of the vacuum system and create a lengthy pump-down process. Out-gassing should be minimized or avoided altogether to achieve low vacuum pressures. The thruster will need to be designed with no closed cavities that could trap pressure

inside the thruster to avoid out-gassing. The materials used in the fabrication of the thruster such as the LTCC, ceramic epoxy, silver epoxy, fittings, and silver paste should avoid or minimize out-gassing as well.

The dimensions of the thruster containment cylinder are dictated primarily by the size of the ICP antenna and the desired thrust. The ICP antenna diameter must be smaller than the thruster cylinder diameter to make full use of the electric field within the region of gas containment. This means that the thruster cylinder must be larger than 1.5 cm, which is the size of the current ICP antenna diameter. The final design requirement is that the thruster cylinder must not be too large to adequately contain the plasma for thrust generation.

### **3-4 Existing Design Evaluations**

#### **3-4.1 Pressure Tests**

An experimental apparatus was created to simulate and evaluate the local pressure inside of the thruster body during argon gas injection. The purpose of this device was to validate the injection hole design for developing a higher pressure inside the thruster containment cylinder than the ambient chamber pressure. The data from the pressure tap locations were also used to draw conclusions about how the gas was behaving as it moved through the cylinder and entered the vacuum. The data obtained from this device was the localized pressure (cylinder pressure minus the ambient chamber pressure) and was compared to the flow rate of the gas entering the system. The injection hole pressure-testing device was made out of an aluminum cylinder with a bored-out central

cavity to simulate the thruster cylinder and can be seen in Figure 15. Aluminum was used for this device for ease of pressure tap fabrication and mounting.

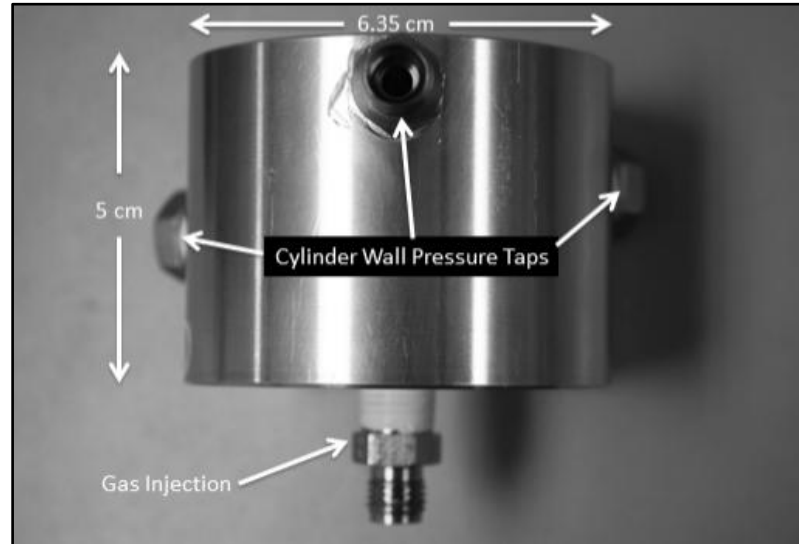


**Figure 15: Pressure-Testing Device showing Gas Injection and Tap Locations**

The device was created with three different pressure taps along the length of the thruster cylinder and a gas injection port at the base of the cylinder. A pressure tap is a hole located in the wall of a device that allows gas to reach an attached pressure sensor. The pressure tap is inserted perpendicular to the gas flow to prevent disruption of the primary flow pattern. It is called a pressure tap because the static pressure of the flow can be measured by connecting a pressure gauge to the tap (“tapping” into the flow). These taps provided attachments for a convectron gauge at any of those points to read the localized pressure near that tap.

The design of the pressure taps was based on the conditions shown in Figure 16. For a wall pressure tap, wall thickness at the tap ( $L$ ) has to be greater than 1.5 times the diameter of the hole in the wall,  $d$ . The tap fitting should have an internal

diameter of approximately two times the hole diameter. These values are based on experimental data provided by Shaw that showed incorrect sizing of the pressure tap could result in false pressure readings [43].

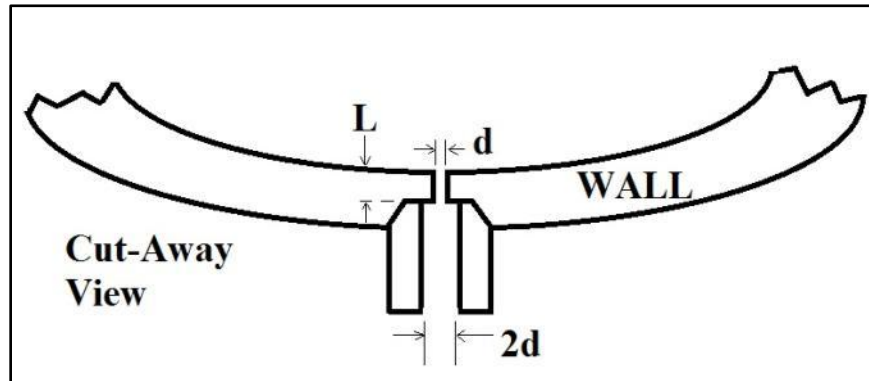


**Figure 16: Wall Pressure Tap for Static Pressure Measurement**

The locations of the three taps were determined by the cylinder diameter as well as the location of where the antenna would be located in the cylinder. These pressure tap locations relative to the cylinder can be seen in Figure 17. The first tap located at the antenna level was referred to as “0d” as it was zero cylinder diameters above the antenna. The next tap location was labeled “0.5d” because it was a half diameter above the antenna level. The same naming convention was chosen for the last tap, which was one diameter above the antenna. These three pressure taps were located on the cylinder walls and were evenly spaced angularly around the circumference of the cylinder (120 degrees). The spacing was specified to prevent the taps from interference with each other.

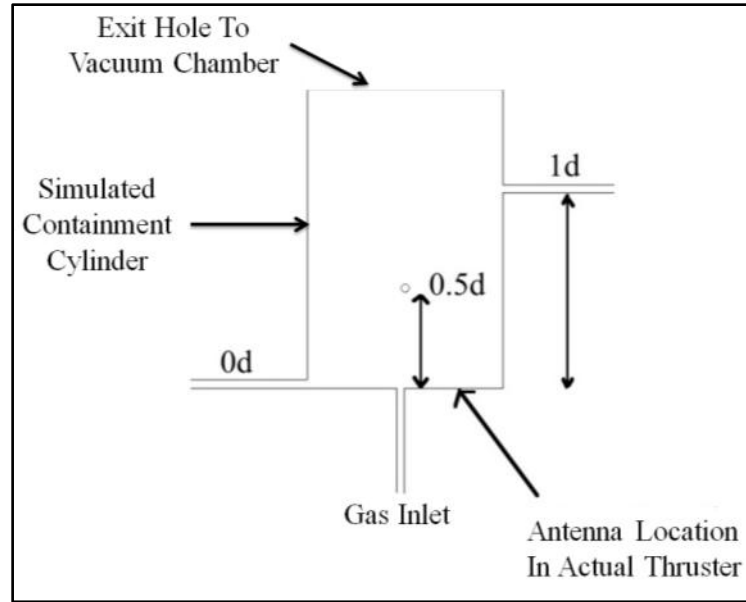


**Figure 17: Location of Wall Pressure Taps Relative to Antenna Location**

A gas line was attached to the base of the cylinder, and pressure measurements were taken at each of the other taps. The pressure data was only read one tap at a time, so three pressure tests were performed. Each pressure test consisted of running the device through a flow range of 1 to 20 sccm in 1 sccm increments.

The three tests were analyzed together to determine local cylinder pressures resulting at each pressure tap. The results, shown in Figure 18, display the median delta pressures (tap pressure minus vacuum chamber background pressure) versus the argon injection flow rate. This plot shows the pressure readings at each of the tap locations as a function of gas flow rate into the thruster cylinder from the base. The delta pressure increases with flow rate for each tap location. There is also a larger difference in delta pressure between taps at the upper end of the flow range. The figure indicates that the median delta pressure, in mTorr, at each flow rate was the largest for the 0.5d pressure tap. The lowest pressures in the cylinder occurred at the 0d pressure tap. It appears the

1d pressure tap saw a smaller pressure than the 0.5d tap because the gas near the top of the cylinder was not as confined by the cylinder, which allowed it to diffuse into the chamber before pressure could build.

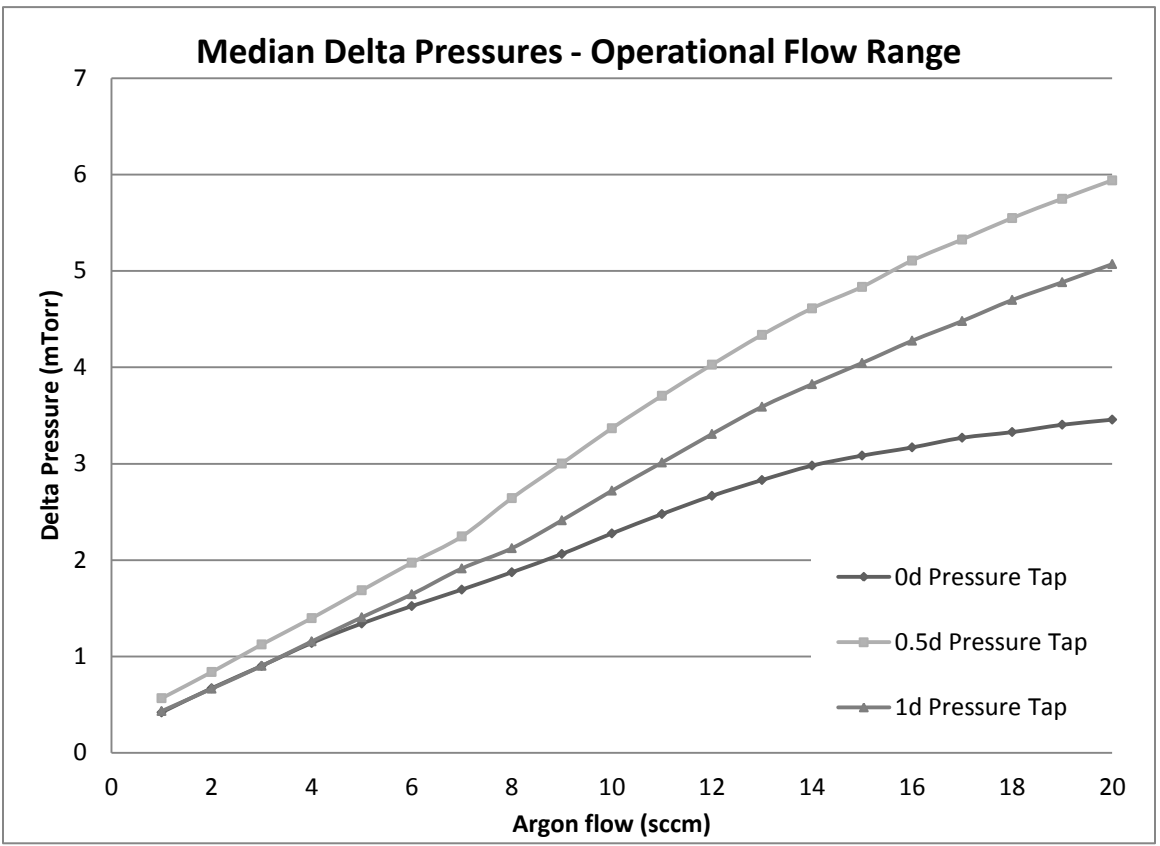


Figure 18: Delta Pressure vs. Argon Flow Rate at Various Pressure Tap Locations

The results from the pressure testing showed that a maximum delta pressure of approximately 6 mTorr was achieved in the cylinder. The lowest delta pressure seen from the maximum flow rate was around 3.5 mTorr and occurred at the base of the cylinder. With the gas injection hole in the center of the base, it appeared the gas was carried out of the cylinder by momentum before the diffusive effects were able to spread the gas in the base of the cylinder.

### 3-4.2 Pressure Test Conclusions

The pressure tests proved that there was a difference in pressure between the thruster cylinder and ambient chamber pressure. Even with the demonstrated pressure difference, the prototype thrusters did not generate plasma well in this pressure range as seen previously in Table 3. It appeared that a better injection configuration was needed to create plasma as the electric field may not have been large enough where the gas was injected. The gas injection location would have to be compared to electric field data to determine the optimal approach for placement of gas injection points.

### 3-4.3 Antenna Electric Field - *COMSOL MultiPhysics* Module

To improve the plasma generation of the design, the electric field intensity of the antenna was modeled. The antenna model was created to demonstrate where the locations of high electric field intensity were located with respect to the antenna. If the center of the antenna was not a region of a high electric field, the injection hole would need to be placed in a region of larger electric field intensity. This option would place a more dense supply of gas in a region where it had a better chance to ionize as more electrons would be available.

The computer model of the antenna was created using *COMSOL Multiphysics*. The antenna model was created by a member of the electric propulsion group, Sonya Shawver, as a means of quickly comparing electric field intensities of various antenna designs without having to build each one [32]. The antenna model incorporated the loss tangent and dielectric constant of LTCC to match a physical device. The antenna model simulation compared experimental data of a prototype with the simulated data for electric field values and peaks. The COMSOL simulations were found to be a good fit with the

experimental data for electric field measurements. The results of this model showed that the largest field occurred beyond a radius of approximately 5 mm from the center of the spiral, which corresponds to the outermost spiral [33]. This antenna electric field model showed the electric field at 1 mm above the antenna with an input frequency of 850 MHz is shown in Figure 19 [32].

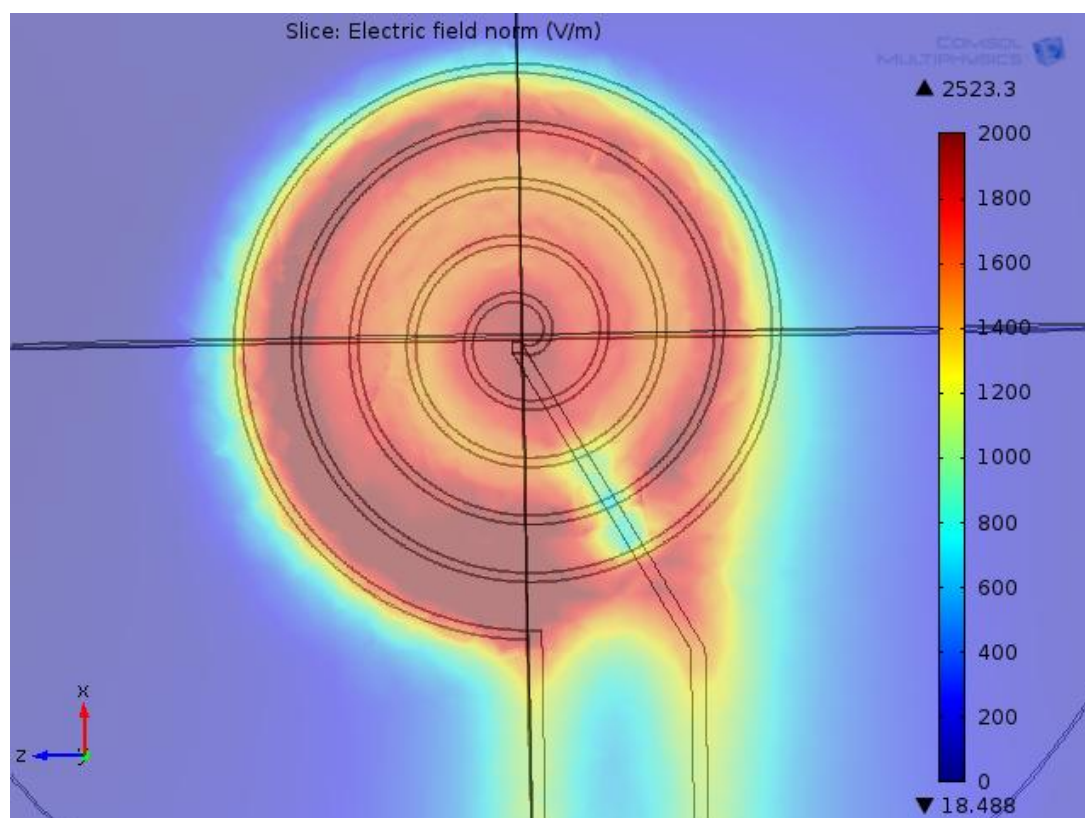


**Figure 19: COMSOL Antenna Electric Field Intensity Model [32]**

The data in this plot (viewed from above) was presented as electric field magnitude rather than a specific directional component. Red values on the plot refer to areas containing the strongest electric field, whereas blue values refer to areas with little to no field. The magnitude of the electric field, or intensity, showed a maximum intensity



of 2,523 V/m, which occurred towards the bottom of the antenna in the figure. The lowest fields occurred near the outside edge of the antenna as well as near the center. The existing gas inlet design, with the inlet located in the center of the antenna, did not make use of the largest electric field intensity of the antenna.

The pressure-testing results in conjunction with the electric field intensity data indicated a change in the gas injection location away from the center was a necessary step in the design [33]. The gas could be injected at a location of high electric field to create a higher pressure of gas in a strong portion of the electric field.

### **3-5 Version 1 Thruster Design**

The initial design of the integrated thruster with containment cylinder was based on factors identified in the prototype evaluation described previously. Design of the gas delivery system of the thruster started with the need to place the propellant injection port at a location of high electric field intensity to improve ionization initiation. This design was further assessed to consider the possibility of adding multiple injection holes to the thruster within the antenna spirals. Having more injection locations would better distribute the gas in the cylinder as well as take advantage of multiple locations of high electric field. A design using four holes placed symmetrically in the antenna coils was chosen as a way of having uniform gas delivery. Four holes would be inherently balanced as well as straightforward to fabricate within the LTCC substrate.

To maintain an even gas distribution at the gas injection holes, a method of choking the flow at the injection hole locations was employed. Choked flow occurs when the velocity of a fluid through a restriction no longer increases with increasing pressure gradient and sonic velocity is reached. Choked flow is reached when the ratio of

downstream pressure to upstream pressure is less than 0.49 for fluids with a specific heat ratio of 1.67 [44]. The mass flow rate of the fluid is fixed during choked flow as long as the upstream pressure is constant. The path of the gas through the LTCC body was designed to ensure choked flow occurred precisely at the injection locations by limiting the injection hole size.

### 3-5.1 Fluid Channel Design

As stated earlier, a design was needed with fully embedded gas channels in the LTCC. With multiple gas injection holes, a gas distribution manifold needed to be formed inside the LTCC. The manifold received a single gas inlet connection on the control interface side of the thruster and split the flow along internal lateral channels to each injection hole. To ensure choked flow conditions, a drop in hydraulic diameter throughout the thruster was needed. Hydraulic diameter is used as a way of calculating fluid flow properties in rectangular channels typically used in LTCC devices. Figure 20 displays the parts and associated cross-sections that made up the gas distribution manifold (Top) and an example rectangular channel with the equivalent hydraulic diameter associated with the channel (Bottom).

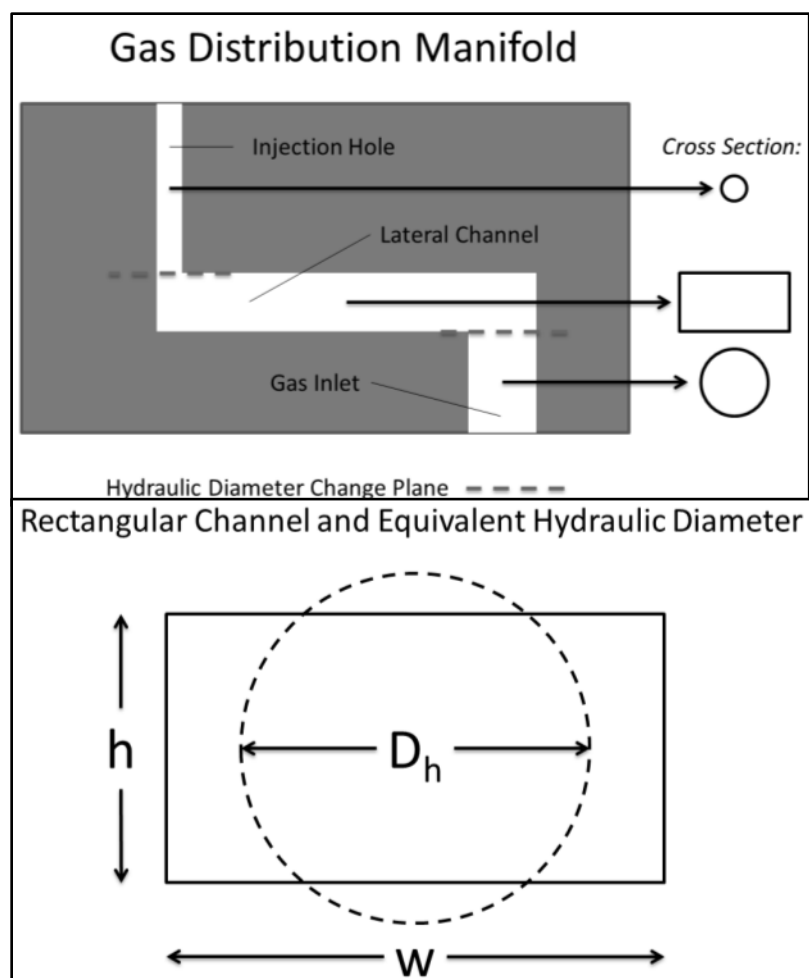


**Figure 20: Gas Distribution Manifold Drawing Distinguishing Parts of the Manifold and the Associated Cross Sections (Top). Rectangular Channel and the Equivalent Hydraulic Diameter of the Channel (Bottom)**

Hydraulic diameter was necessary because circular cross-sections were compared to rectangular cross-sections for fluid flow. The equation for hydraulic diameter,  $D_h$ , is shown in Equation 3, where  $A$  is the area of the cross-section,  $P$  is the perimeter of the cross-section,  $h$  is the height of the cross-section, and  $w$  is the width of the cross-section [45].

$$D_h = \frac{4A}{P} = \frac{4hw}{2h + 2w} \quad (3)$$

Using this equation, the size of the internal channels was calculated to ensure the choked flow occurs at the injection holes. A drop in size of half the hydraulic diameter in each section of the internal LTCC manifold was targeted to ensure the largest restriction of the flow (throat) was located at the gas injection location. The gas inlet size on the control interface side of the thruster was based on the inner diameter of a typical Swagelok eighth-inch gas fitting. The inlet hole was sized at 1.68 mm, which was approximately 70% of the fitting inner diameter to allow for possible misalignment. Given the inlet hole size, the calculations at various sections of the fluid delivery channels were made. The first step in hydraulic diameter occurs at the transition from the circular gas inlet section to the rectangular channels travelling laterally through the thruster body. The new diameter size was calculated to be 0.84 mm based on the 50% drop in hydraulic diameter. To calculate the width of the channels, Equation 3 is solved for width as a function of height and hydraulic diameter. This new simplified equation is shown as Equation 4.

$$w = \frac{h}{\frac{2h}{D_h} - 1} \quad (4)$$

As hydraulic diameter is a known value for this step and the width of a single LTCC layer is 0.215 mm (fired size), the width can be solved for based on the number of layers. A relationship for channel height in layers versus channel width based on the hydraulic diameter value of 0.84 mm is shown in Figure 21.

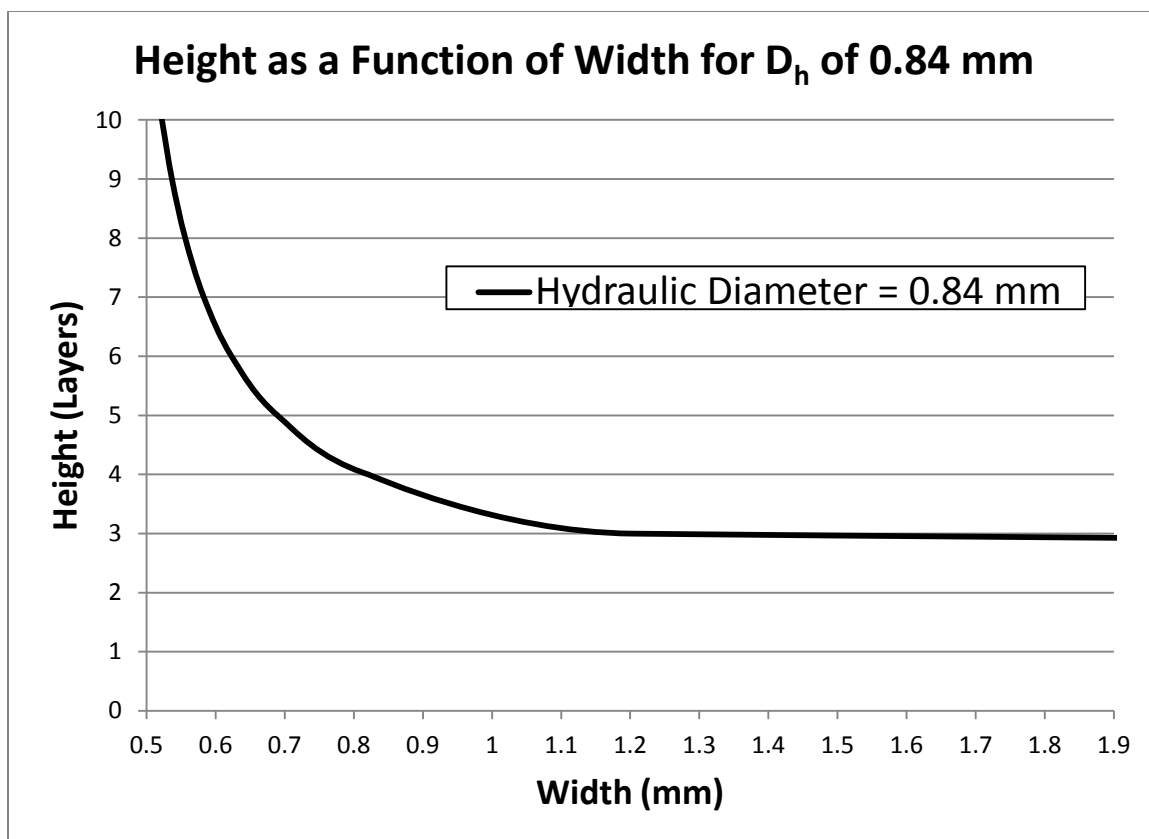


**Figure 21: Calculation Showing the Relationship between Number of Layers and Width of Channel for a Hydraulic Diameter of 0.84 mm**

The figure shows that a height of three layers of LTCC requires a width of at least 1.2 mm to have the hydraulic diameter of 0.84 mm. Width values larger than 1.2 mm would make a small increase to the hydraulic diameter as long as three layers are used. A lateral channel height of four LTCC layers or more would decrease the width of the channel below one millimeter, which could cause fabrication issues when cutting and handling the sacrificial carbon tape needed to fill the channels. The lateral channel height was set at three layers of LTCC due to these limitations. Since the width of the lateral channel could vary without a large change in hydraulic diameter, a width was chosen as 2

mm. These two values for height and width created a hydraulic diameter of 0.98 mm, which is well below the 1.68 mm gas inlet diameter.

The next step in hydraulic diameter comes from the jump from the lateral channel through the manifold to the vertical gas injection holes. The gas injection holes are circular; therefore, a hydraulic diameter is equal to the diameter of the channel. With a previous value of 0.98 mm, the new channel should have a maximum diameter of 0.49 mm. The value for this design was chosen to be 0.4 mm to ensure the injection points have the smallest hydraulic diameter in the fluid path to create choked flow. Now that the gas manifold sizing was calculated to ensure choked flow, a solid model of the thruster design was created with these determined or calculated values.

### 3-5.2 Design of the Thruster Body Solid Model

The solid model development discussed in this section will be the basis of the thruster body design. The geometry was altered in future designs to correct fabrication issues. An iterative approach to the final design will be discussed further in the fabrication section of the thesis. The thruster body was made up of several bodies of LTCC fired together. These bodies consist of the thruster base, the antenna disc, and the gas containment cylinder as seen in Figure 22. The design of these bodies will be discussed in more detail in this section.

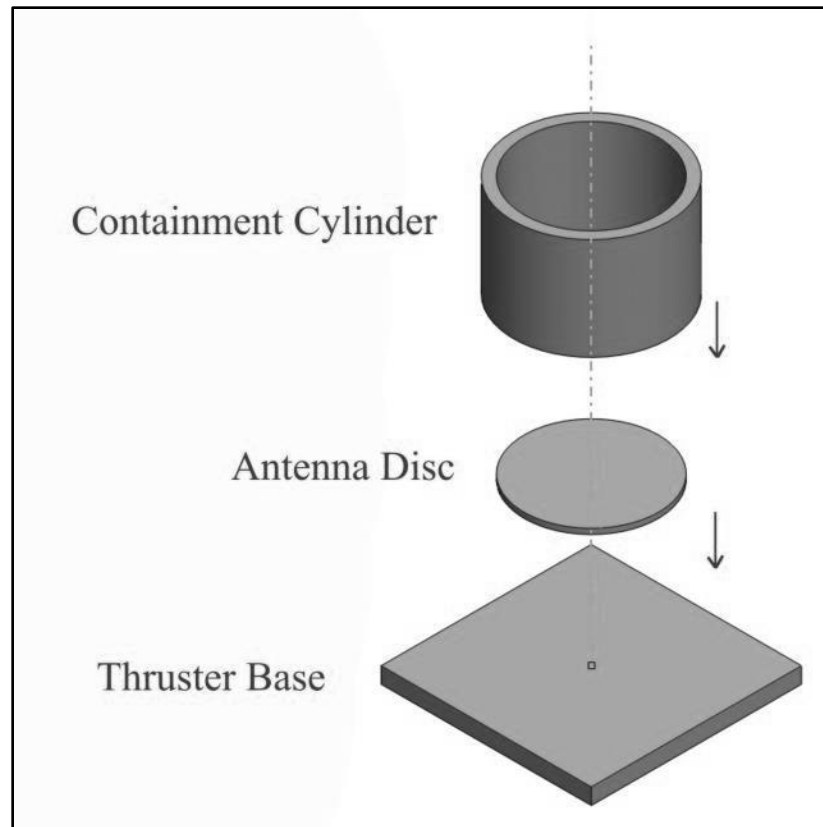


**Figure 22: Separate LTCC Components of the Thruster Assembly**

### Thruster Base Design

Multiple factors were considered for the development of the thruster base design. These factors included the channel design, the placement of the gas fitting and electrical connector on the control interface side of the thruster base, and the location of the alignment holes used for mounting purposes. The base needed to incorporate all the mentioned factors with clearance room for external attachments that would hold the thruster base on the thrust stand for measurement and testing purposes. These factors were achieved in a pre-fired thruster body size of 45 mm by 45 mm. The *SolidWorks* design was developed with post-fire dimensions to account for shrinkage. Unless

otherwise noted, all stated dimensions in this document were based on fired devices. Unfired dimensions are occasionally presented as fabrication constraints with the design. Each factor that guided the footprint will now be discussed in greater detail.

The propellant delivery system needed in the thruster was one of the primary factors for the thruster base design. The sizing of the gas manifold channel cross-sections was previously discussed in Section 3-5.1. Another important factor when designing the lateral channels was the consideration of the shape and placement of them within the thruster base. These channels were positioned near the control interface side of the thruster base to provide separation between the antenna and the gas flow. This separation provided by increasing the number of LTCC layers was used to discourage any plasma generation within the lateral channels by increasing the thickness of the dielectric material separating the channels and antenna. This same concept of creating dielectric separation distance was incorporated for the electric pathways within the device. Two layers of separation were utilized between the antenna's return trace and the lateral gas channels.

The gas manifold had to supply equal pressure gas to all gas injection holes without locating the lateral channels directly below the antenna. This design consisted of a main channel located outside the perimeter of the antenna with several branches protruding inwards toward the gas injection hole locations as shown in Figure 23.



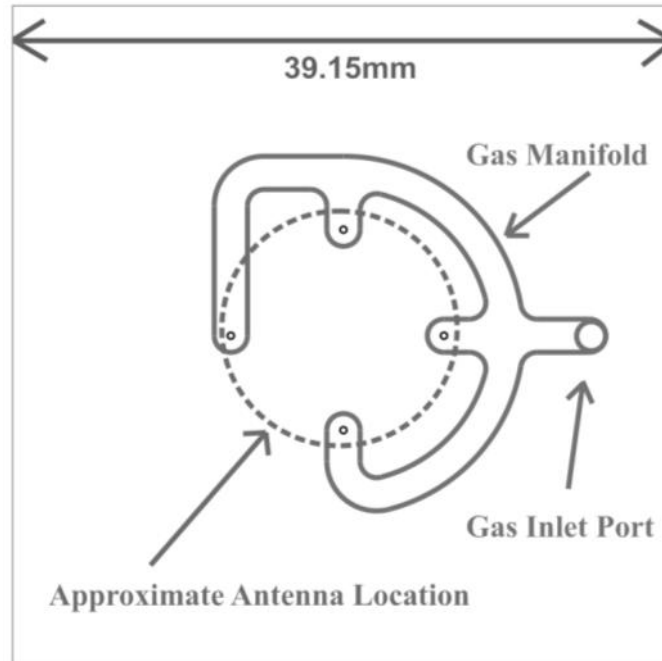


**Figure 23: Top-Down View of the Gas Manifold Shape and Location Relative to the Antenna as Well as the Gas Inlet Port**

Based on the earlier analysis, the design lateral channels were two millimeters wide and three LTCC layers thick. The design also utilized rounded channel corners to allow for smooth gas flow and to minimize internal stress concentrations.

Another factor considered at this stage of the design of the thruster was the location of any metal located behind the thruster antenna. The gas line fitting for the thruster base was made of stainless steel because of its availability and vacuum compatibility.

As shown in Figure 23, this fitting would have to be located radially out from the antenna centerline and beyond the perimeter of the coil to avoid interference with the antenna's electric field. The location of the gas inlet into the thruster was therefore placed near an edge of the thruster base.

As discussed earlier, a new type of SMA connector was incorporated in this design, which could be placed on the control interface side of the thruster. A surface-mount SMA connector made by Linx Technologies Inc. (CONSMA001-SMD) was selected. Reference geometry was created for the SMA connector that consisted of four squares where the legs of the connector attach as well as the central pin, referenced with a circle, and can be seen in Figure 24. The reference geometry was placed in the design and allowed for a visual representation of the connector footprint location after the thruster was fired. The reference geometry was also incorporated as a guide for the SMA connector legs as a stencil with the design and was used to apply silver paste to the location of attachment to the thruster base.

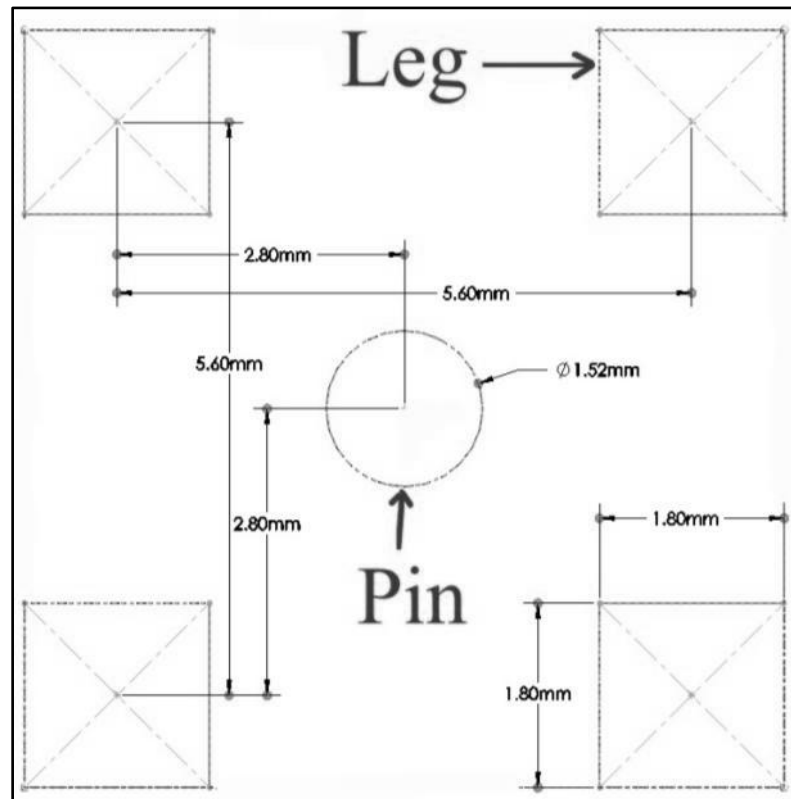


**Figure 24: SMA Connector Reference Geometry Pattern for Base Interconnects**

Metal located on the control interface side of the device could interact with the SMA connector and create a plasma glow discharge from the high frequency RF signal. The gas fitting and SMA connector were located on opposite sides of the thruster control interface. Also, to prevent interference with the antenna electric field, both electric and fluidic connectors were positioned radially outward from the axis centerline and beyond the perimeter of the antenna, as seen in Figure 25.

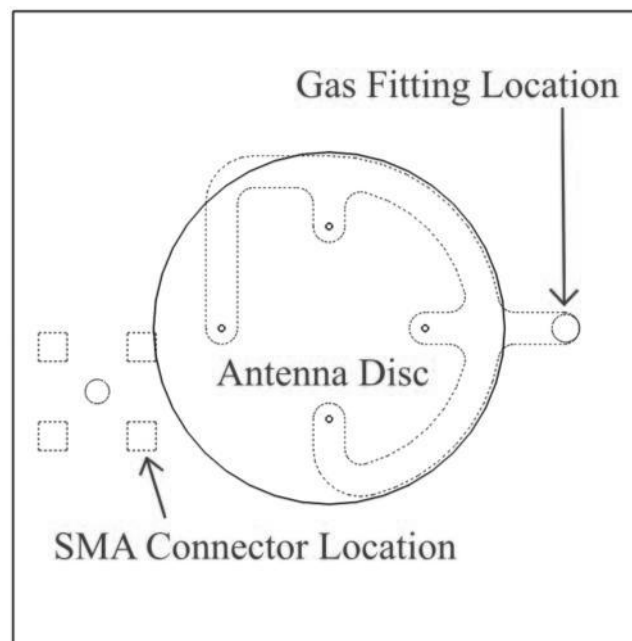


**Figure 25: SMA Connector and Gas Inlet Relative to Antenna**

Lastly, the alignment holes seen near the four corners of the thruster base in Figure 26 were designed. These holes were designed to match an existing design of the electrostatic grid holder that was in development for the thruster. The grid holder will hold the thruster's accelerator and screen grids together (separated by an LTCC washer) as well as clamp the grids to the thruster body. The grid holder uses two alignment holes diagonal from each other. Two additional alignment holes were included for use as

attachment points for a mounting fixture that would connect the thruster to a thrust stand used to measure thrust [46]. These holes were sized to a diameter of 3.1 mm to provide a modified close fit for the size 4 nylon all-thread shafts used to locate and install the grid holder. The modified close fit was determined by averaging the close fit and free fit clearance values found for the #4 screw size on a drill chart. This averaging was used to account for any variable shrinkage as well as allow a secure fit for the threading. With the thruster base defined and setup in *SolidWorks*, design of the antenna disc for the thrusters could begin.

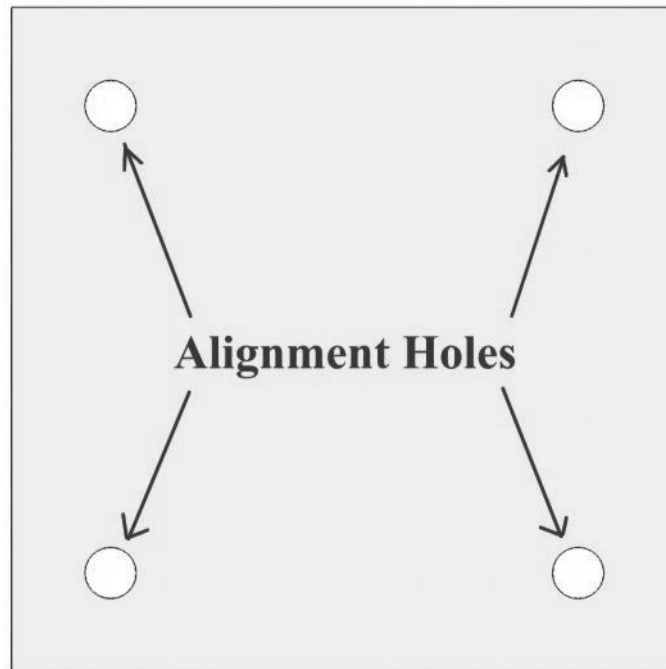


**Figure 26: Thruster Body Showing the Four Alignment Holes Used for Grid Holder Attachment and Thrust Stand Mounting**

### Antenna Disc Design

The antenna disc was designed to incorporate multiple layers of LTCC with the top layer including the antenna. This feature was comprised of circular layers for the thruster cylinder to encompass. An existing lamination fixture for rolled LTCC thruster cylinders was a guiding factor for the diameter of the disc layers. This fixture has a diameter of approximately 25 mm and this was used as the design guideline for the LTCC disc. Four circular layers of LTCC were chosen in the design to create an adequate bonding area with the cylinder during firing. The antenna disc serves as a structural support for the thruster cylinder as well as a means of creating a hermetic seal at the base of the thruster cylinder.

A *COMSOL* simulation was performed that showed stronger electric field intensities were achieved when the return trace of the antenna was only two LTCC layers deep before it was directed radially outward from the centerline of the antenna [32]. The design of the return trace, seen in Figure 27, dropped to the third layer of the antenna disc, before it extended outward, and then dropped into the thruster base. Once the return trace was in the thruster base, it was placed two layers deep before it extended to the final via location that connected to the control interface side of the thruster base. The antenna trace was placed two layers into the thruster base to ensure only a weak electric field occurred outside the thruster cylinder from the traces.

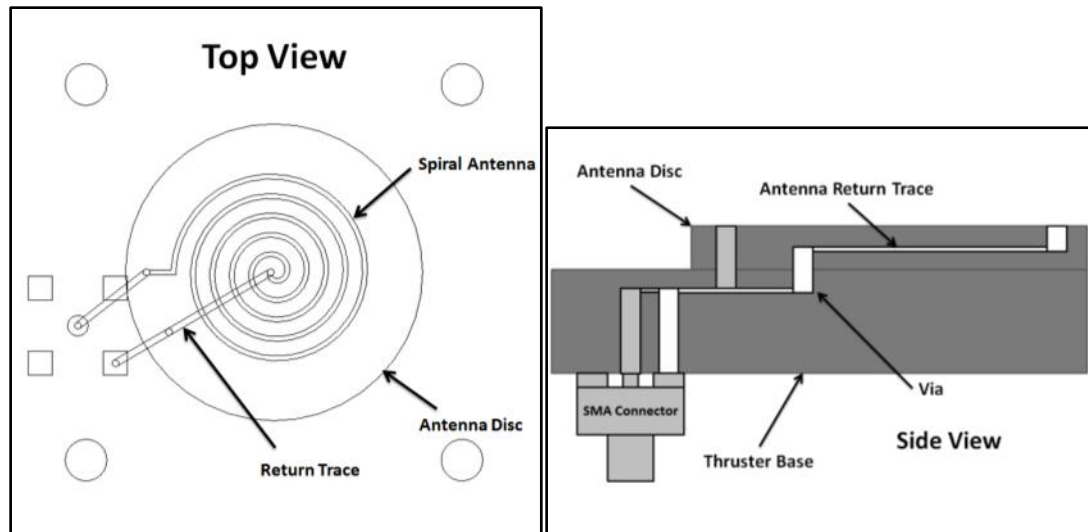


**Figure 27: Top View (Left) and Side View (Right) Displaying Location of Antenna and Traces with Respect to the Antenna Disc, Thruster Base, and SMA Connector**

The next factor to consider with the design of the antenna disc was the location of the gas injection holes relative to the center of the antenna. As mentioned earlier, a mapping of the electric field intensity was used to position the gas inlets in regions of strongest electric field [32, 33]. The electric-field mapping demonstrated a large field roughly in between the two outermost revolutions of the antenna. The antenna was placed directly in the center of the disc layers and four gas injection holes were positioned inside the outer antenna coil. The holes were placed as close to the center of the two outer coils as possible, as seen in Figure 28.

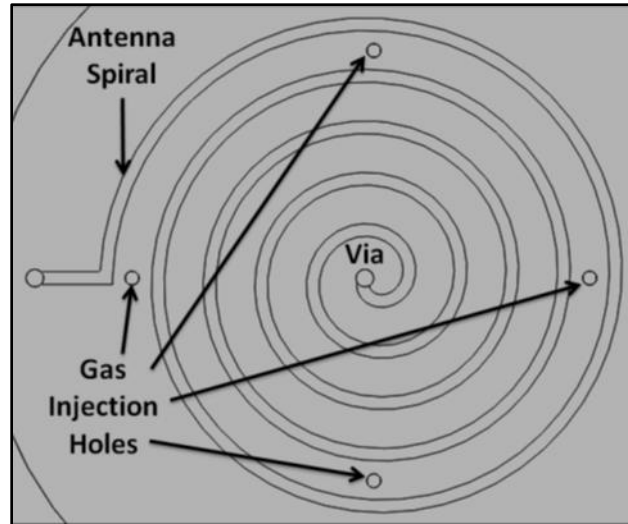


**Figure 28: Top View of the Gas Injection Holes Relative to Antenna**

The high pressure of the gas as it leaves the injection holes should improve plasma start power in these regions where the propellant gas density and electric field converge at maximum values.

After the gas injection holes were repositioned into the high electric-field intensity regions, an updated *COMSOL* antenna model that included the new gas injection hole locations was created [32]. *COMSOL* can calculate an average electric-field intensity inside the injection hole locations. After the *COMSOL* model was revised to include the injection holes, the electric field in the vicinity of the new injection holes could be compared to the electric field in the vicinity of the single center injection hole design. The updated *COMSOL* model results 1 mm above the antenna can be seen in Figure 29.

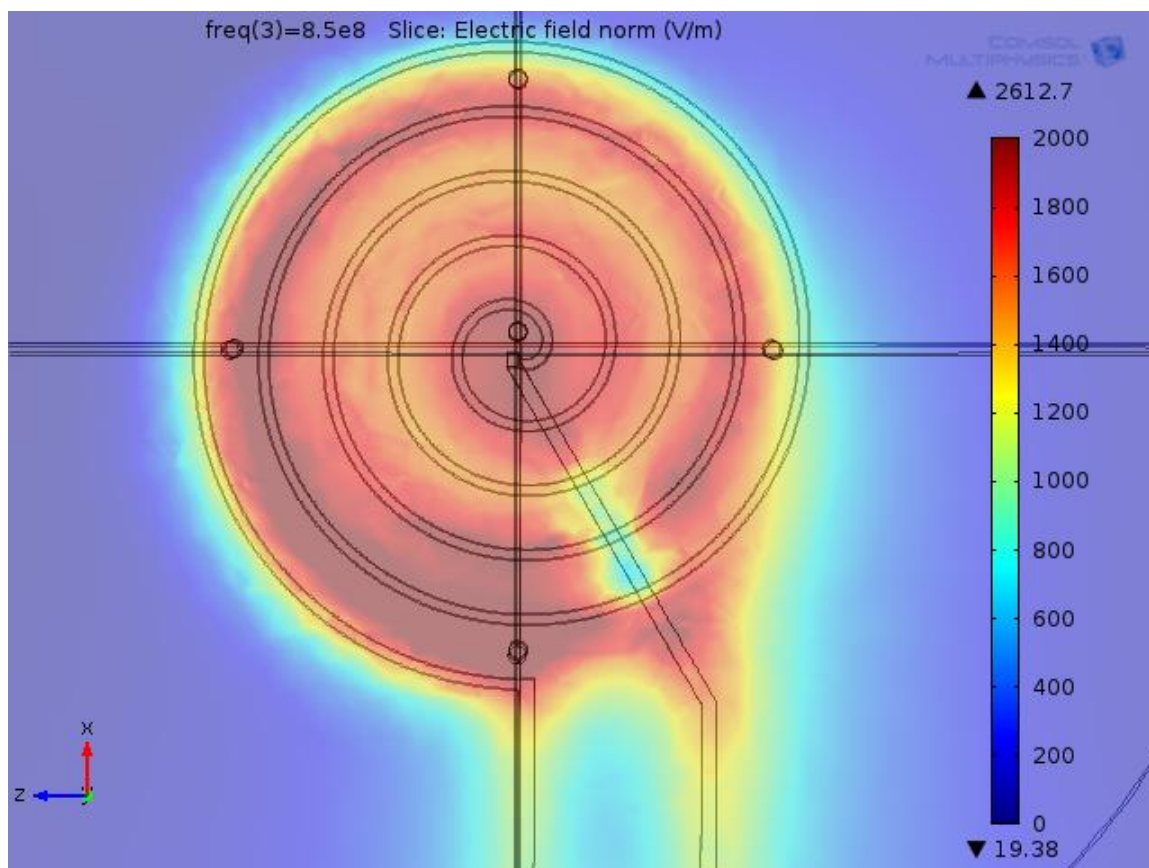


**Figure 29: Plot of *COMSOL* Electric-Field Intensity Including the Single Gas Injection Hole as well as the Repositioned Gas Injection Holes [32]**

This figure shows the location of all five gas injection holes between the two thruster designs (one injection hole and four injection hole) on a single plot. The electric-field intensity data generated by *COMSOL* between each of the thruster injection hole designs was compared to determine which design has a larger magnitude electric-field in the hole locations. Figure 30 shows a plot of the volume averaged electric field intensities for the two different injection hole configurations versus a range of frequencies. To calculate the volume averaged electric-field intensity, *COMSOL* finds the average electric field in each domain (hole), and in the case of the four injection hole design, it finds a single average for all four holes.



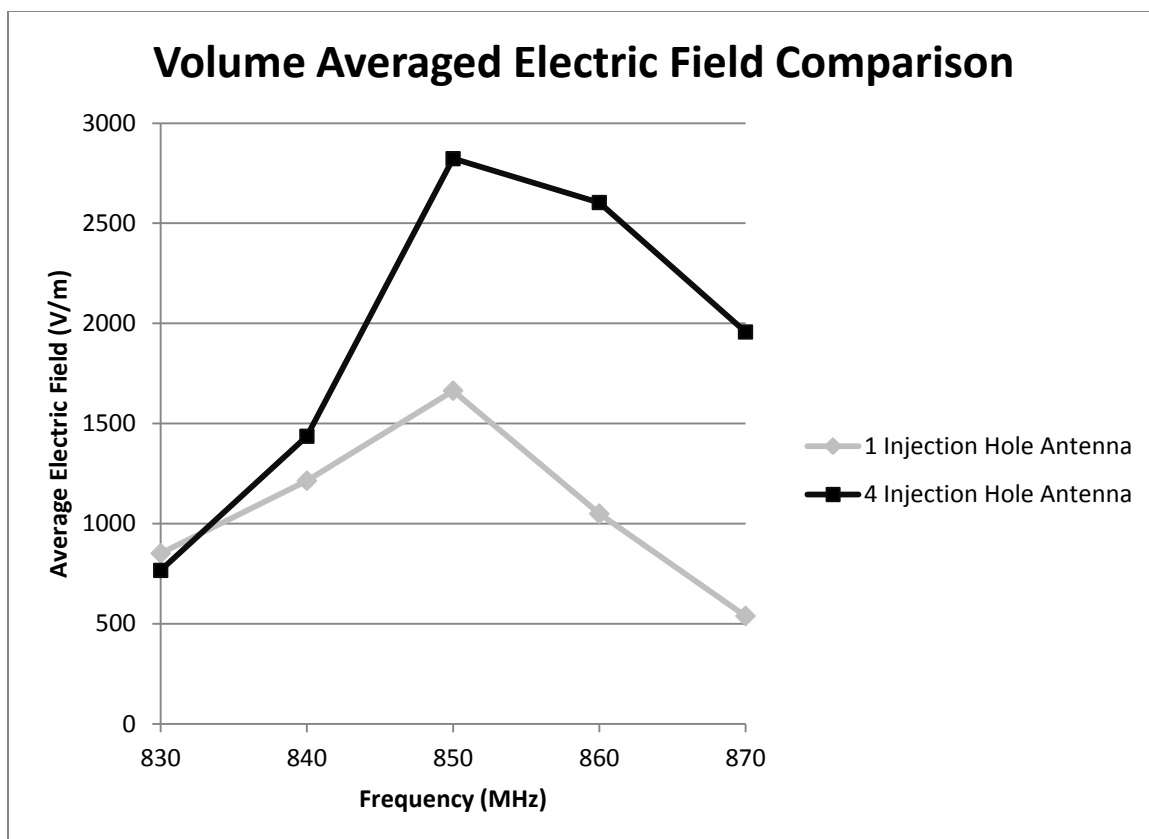


**Figure 30: Volume Averaged Electric-Field Intensity of 1 and 4 Injection Hole Antenna Designs [32]**

The one injection hole design has a slightly higher simulated electric field than the four hole design at 830 MHz. The four injection hole design has a higher volume averaged electric-field intensity throughout the rest of the frequency range. The two antennas both performed the best at the 850 MHz frequency with a difference of 1159 V/m. This result shows that the electric field must be slightly higher at the center of the antenna at lower frequencies, and as the frequency is increased the large electric-field regions tend to localize around the outer part of the antenna. This information supports the idea of using the four injection hole configuration around the edge of the antenna versus the single center injection hole design.

### Thruster Cylinder Design

The thruster cylinder was designed to properly seat around the circular layers of the antenna disc and create a seal when fired. For optimal efficiency, the thruster cylinder was designed with a 0.75 cylinder height to cylinder diameter ratio [47]. Using the established diameter of the thruster cylinder and the antenna disc size of 25 mm, the cylinder length was calculated to be 18.75 mm. The thickness of the LTCC cylinder wall was five layers. The attachment of the cylinder to the antenna disc and thruster base will be done with PEOX to create a seal. The bottom of the cylinder will sit on the thruster base and the thruster cylinder will be aligned with the antenna disc [42].

The final solid model design of the thruster can be seen in Figure 31. This figure includes the containment cylinder, antenna disc, thruster base, gas fitting, and SMA connector. The left picture of the figure displays the full design with connectors while the right picture of the figure displays a cross-sectional view of the thruster, which shows the internal gas channels.

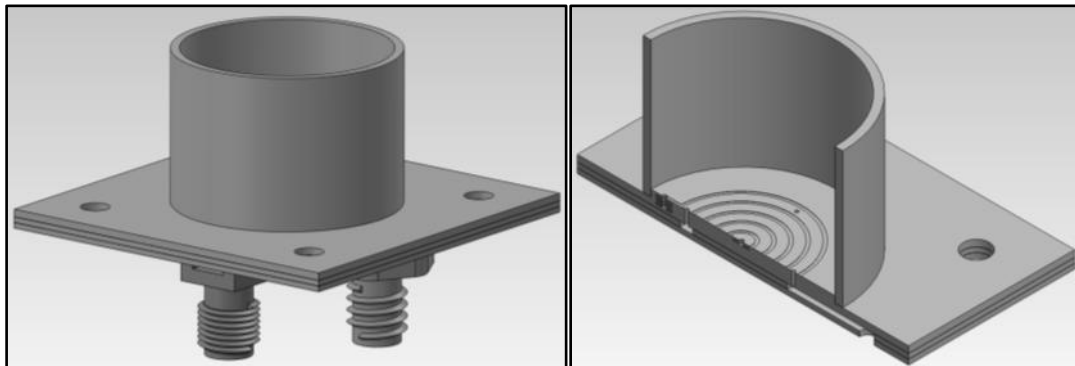


**Figure 31: Solid Model of Thruster after Fabrication with Connectors (Left) and a Cross-Sectional View Displaying Gas Channels (Right)**

## CHAPTER 4: COMPUTATIONAL FLUID DYNAMICS MODEL

The creation of a computational fluid dynamics model of the propellant flow was desired to simulate any gas injection configuration considered for future designs. A CFD model of the propellant flow was developed to simulate various flow rates through the four gas injection hole configuration. The generated CFD model could be validated using a pressure-testing device to experimentally measure pressure at the wall of the containment cylinder. If the model proved to be valid against experimental data, future gas injection configurations could be modeled and conclusions then drawn as to which injection point configurations were optimal for creating a high localized pressure region inside the thruster cylinder. The pressure data at the gas injection holes and 1 mm above the antenna in the high electric-field locations could then be used to evaluate other gas injection hole configurations simulated by a CFD model. These comparisons would then be used to determine the best possible gas injection configuration to maximize efficiency of the thruster. One concern with this approach is the assumption that the flow throughout the thruster body and containment cylinder is in the continuum regime. At lower pressures, the continuum assumption begins to break down, but without knowing the gas pressure, it is not clear where the CFD modeling approach becomes invalid. The development of the CFD model will be discussed in this chapter of the thesis while the results of the CFD model will be presented in Chapter 6.

#### 4-1 ANSYS Fluent Software

The software used to develop the CFD model in this thesis was *ANSYS Workbench* with *Fluent* [48]. This software is a fluid dynamics package that uses a finite volume analysis approach to solving complex fluidic models. *Fluent* can model viscous effects, thermal effects, pressures, temperatures, velocities, and more. This software is only capable of handling fluid flow in the continuum regime due to the inherent solver equations used in the software. The calculations performed in this software are based on Navier-Stokes equations, which are only valid for fluids that are considered infinitely divisible rather than particles or molecules.

#### 4-2 Thruster CFD Model

The CFD model for this thesis was a full 3D representation of the propellant flow paths through the LTCC thruster body designed in the previous chapter. The CFD model fluid flow geometry contained the propellant delivery system of the thruster, starting with the gas inlet hole of the gas manifold through the containment cylinder of the thruster, as seen in Figure 32.

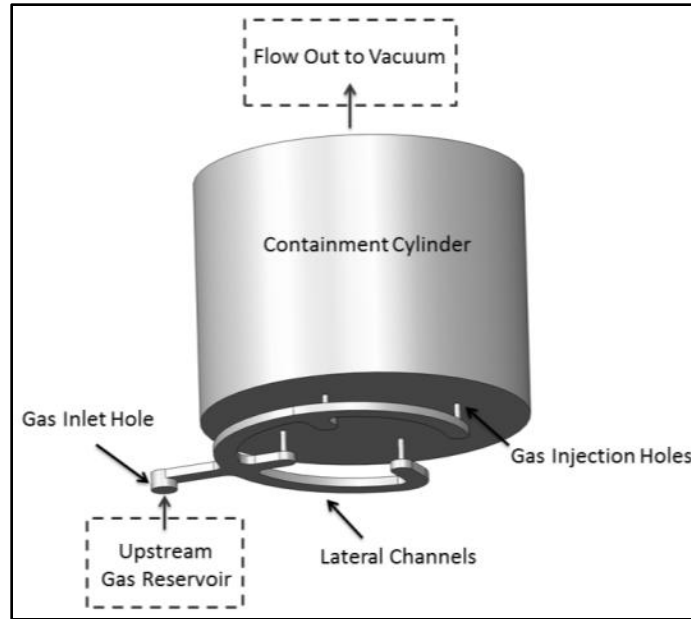


**Figure 32: Fluid Flow Path Geometry Created for Analysis of the Four Gas Injection Hole Design**

In the CFD model, the gas transitioned from a larger pressure at the gas inlet hole to a very small pressure as it enters a low back pressure outflow region simulating the chamber or operation in space. This transition from higher pressure to near-vacuum could cause the flow within the thruster to be out of the continuum regime, which would invalidate the CFD model. The gas flow for this CFD model was assumed to be continuum if the propellant molecules in the flow were dense enough that the mean free path (the average distance a gas molecule will travel before colliding with another molecule) of a gas molecule was much smaller than the diameter of the body containing the molecule. Calculations of various input parameters were required during creation of the CFD model and are presented in the next two sections.

### 4-3 Choked Flow Verification and Critical Pressure Calculations

Choked flow was used as a design parameter while generating the thruster geometry and was originally presented in Chapter 3. The propellant flow was choked at the injection holes to ensure equal gas distribution through the ports into the chamber. Calculating choked flow conditions was necessary for the CFD model setup, because the CFD model required gas inlet temperature, pressure, and velocity to initialize the flow. With choked flow known, these values can be calculated.

The decrease in area seen by the gas as it moves from the gas inlet through the gas injection holes of the thruster can be approximated simply as a converging nozzle. A converging nozzle representing the CFD model with choked flow conditions can be seen in Figure 33.

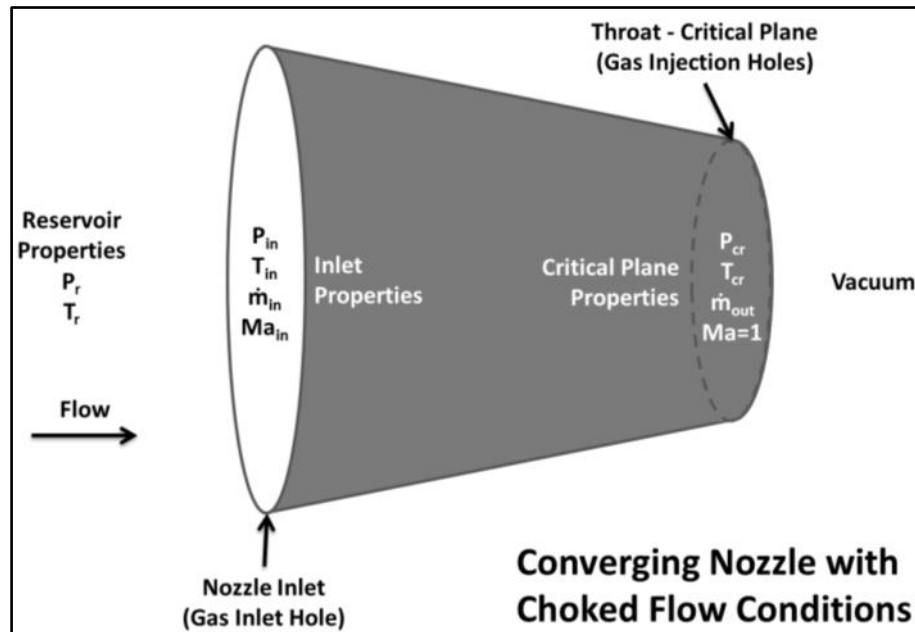


**Figure 33: Converging Nozzle with Choked Flow Conditions Highlighting Fluid Flow Properties and Locations of the Nozzle Relative to the CFD Model**

The dimensionless Mach number is a ratio of the speed of a fluid to the speed of sound in the fluid at the same state. The critical plane of a converging nozzle with choked flow conditions occurs at a location where the flow faces the largest restriction (known as the throat). This is defined as a Mach number of 1. Critical plane pressure and temperature could be calculated with the choked flow conditions. The results of the critical plane analysis were used to calculate the boundary conditions at the gas inlet hole. The analysis presented in this section assumed one-dimensional isentropic flow and was based on concepts and equations presented in *Thermodynamics: An Engineering Approach* [44].

The temperature and pressure at the critical plane are denoted as critical temperature and critical pressure. The pressure upstream from the gas manifold was much larger than the ambient pressure in the vacuum chamber. The upstream pressure will be referred to as reservoir pressure throughout this analysis. To verify that choked flow existed in the CFD model, the critical pressure ratio across the gas injection exit was calculated in an analytical model.

$$\frac{P_{cr}}{P_r} = \left( \frac{2}{\gamma + 1} \right)^{\frac{\gamma}{\gamma - 1}} \quad (5)$$

Equation 5 shows the critical pressure ratio for isentropic flow of ideal gases. In this equation, the variable  $\gamma$  represents the ratio of specific heats of the gas,  $P_{cr}$  represents the critical pressure, and  $P_r$  represents the reservoir pressure. Argon is a monatomic gas with a specific heat ratio of 1.67. Substituting this value into the equation, the pressure

ratio is calculated to be 0.49. This demonstrates that as long as the reservoir pressure is at least 2.05 times the critical pressure, choked flow occurs. With the system having a near-vacuum downstream of the thruster, it is assumed the pressure ratio across the gas injection exit is always greater than 2.05. This is because even a small pressure such as 1 mTorr is still at least an order of magnitude greater than typical pressures seen in the chamber during argon flow.

To calculate the reservoir pressure upstream from the choked plane, an additional set of equations was needed. The first equation is a form of the continuity equation and states that mass flow,  $\dot{m}$ , is constant as long as there are no other inputs or outputs as can be seen in Equation 6.

$$\dot{m}_{in} = \dot{m}_{out} \quad (6)$$

The next equation necessary for this analysis is the velocity of the gas at the critical plane,  $V_{cr}$ . Equation 7 is the critical plane velocity equation, which is derived from the speed of sound equation. With a Mach number of 1 at the critical plane for choked flow, the critical velocity is equal to the speed of sound,  $c$ , in the gas being used.

$$V_{cr} = c = \sqrt{\gamma RT_{cr}} \quad (7)$$



Note that the constant  $R$  in this equation is the specific gas constant of argon rather than the universal constant.  $T_{cr}$  is the critical temperature at the exit plane and  $V_{cr}$  is the critical velocity at the choked plane. The ideal gas equation solved for density at the critical plane,  $\rho_{cr}$ , was also needed and is seen as Equation 8.

$$\rho_{cr} = \frac{P_{cr}}{RT_{cr}} \quad (8)$$

In addition to the critical pressure ratio equation listed earlier, Equation 5, the critical temperature ratio, Equation 9, was used to determine the critical temperature at the nozzle exit.

$$\frac{T_{cr}}{T_r} = \frac{2}{\gamma + 1} \quad (9)$$

$T_r$  in the equation is the reservoir temperature, which is the temperature of the gas upstream of the gas inlet hole of the thruster. Finally, Equation 10 describes the nozzle mass flow rate at the critical plane as a function of density, area, and velocity.

$$\dot{m}_{out} = \rho_{cr} A_{cr} V_{cr} \quad (10)$$

As shown in Equation 6, describing continuity of the flow through the nozzle at steady-state conditions, the inlet mass flow rate is equated to the mass flow rate at the critical plane (throat of the nozzle). The mass flow rates are equal; therefore, the mass flow rate will be described as the variable  $\dot{m}$  without any subscripts. The remaining equations, 5, 7, 8, and 9, were combined into a single mass flow rate equation with only reservoir pressure as an unknown. The resulting equation is solved for reservoir pressure,  $P_r$ , and then simplified.

$$P_r = \frac{\dot{m}}{A_{cr}} \left( \frac{RT_r}{\gamma} \right)^{\frac{1}{2}} \left( \frac{\gamma + 1}{2} \right)^{\frac{\gamma+1}{2(\gamma-1)}} \quad (11)$$

Equation 11 presents the reservoir pressure upstream of the gas manifold as a function of known values. The critical plane area was calculated as the total area of all four gas injection holes and the mass flow rate is the total flow of all the holes as well. The values used in the calculations for the reservoir pressure can be seen in Table 5.

**Table 5: Values Used in Analysis for Reservoir Pressure Calculations**

<i>Values for Reservoir Pressure Calculations</i>		
Argon Properties at 300K		Units
$c_p$	520.3	J/kg*K
$c_v$	312.2	J/kg*K
R	208.1	J/kg*K
$\gamma$	1.667	None
Argon Density at Standard Conditions		Units
$T_{\text{standard}}$	293	K
$P_{\text{standard}}$	101325	Pa
$\rho_{\text{standard}}$	1.662	kg/m <sup>3</sup>
Gas Inlet Dimensions		Units
(Inlet Diameter) $D_{\text{in}}$	1.75	mm
(Inlet Area) $A_{\text{in}}$	2.405	mm <sup>2</sup>
Critical Flow Plane (throat) Properties		Units
(Injection Hole Diameter) $d$	0.4	mm
(Injection Hole Area) $A_{\text{cr}}$	0.126	mm <sup>2</sup>

The reservoir pressure calculations require a specific flow rate; thus, calculations were done for various gas flow rates. Results of a few calculations can be seen in Table 6. Critical plane velocity and temperature can both be calculated from Equations 7 and 9, and are equal to 276.1 m/s and 219.8 K, respectively.

**Table 6: Calculated Critical and Reservoir Pressure Data for Various Flow Rates**

Argon Flow Rate (sccm)	Critical Pressure, $P_{cr}$ (Torr)	Reservoir Pressure, $P_r$ (Torr)
1	0.068	0.140
5	0.341	0.700
10	0.682	1.401
50	3.411	7.003
100	6.823	14.006
200	13.646	28.011
500	34.115	70.029

Figure 34 demonstrates the critical pressure as well as the reservoir pressure as functions of flow rates from 0.1 sccm to 500 sccm. Pressure increases as the flow rate is increased. The reservoir pressure and critical pressure both have a linear relationship and the reservoir pressure is always greater. This figure is a useful tool for quickly figuring out approximately what the critical pressure value will be for any given flow rate within a flow range of up to 500 sccm. Figure 34 is only valid during choked flow. If the reservoir pressure and mass flow rate into the gas inlet hole drop to the point where the flow is not choked, the assumption of a Mach number of one is not valid.

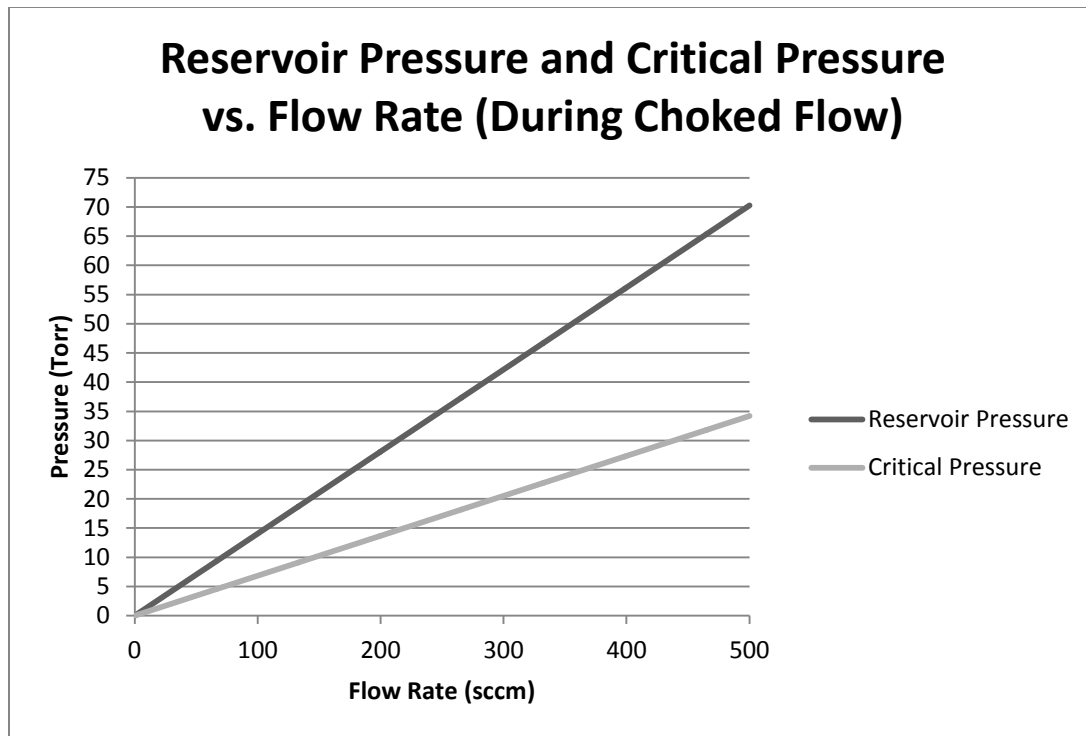


**Figure 34: Reservoir Pressure and Critical Pressure Relationship versus Flow Rate (Valid Only During Choked Flow)**

#### 4-4 Verification of Continuous or Molecular Flow

Modeling the behavior of gases at low pressures can potentially violate the assumption of continuum flow used in finite difference techniques. The Knudsen number is a non-dimensional number that is used to describe if the gas flow is in the molecular or continuum regime. Knowing the Knudsen number is important because the simulation assumes continuum flow. If the Knudsen number doesn't fall within the continuum regime, the simulation results will not be valid. The Knudsen number is defined as a ratio of the molecular mean free path to a representative physical length scale and is presented in Equation 12. The following Knudsen number equations and analysis were based on a similar nozzle analysis [49].

$$Kn = \frac{\lambda}{L} \quad (12)$$

The Knudsen number was considered at two locations in the CFD model to validate whether or not the flow regime was considered continuum. The first location was at the critical plane (gas injection hole location). The second location was inside of the cylinder of the thruster. If these two locations could be verified as continuum flows, the CFD model would be considered valid.

A separate mean free path for argon was calculated for both locations based on local pressure. The mean free path calculation requires the Boltzmann constant and the hard-shell diameter of argon. Equation 13 is the mean free path equation used in this analysis.  $T$  represents the absolute static temperature of the gas,  $P$  is the absolute local static pressure, and  $\lambda$  is the mean free path.

$$\lambda = \frac{k_B T}{\sqrt{2} \pi \sigma^2 P} \quad (13)$$

The hard-shell diameter of argon,  $\sigma$ , is based on the atomic radius of the molecule and has many different values based on how the radius is calculated. For these calculations, the mean Van der Waals radius will be used and has a value of 1.88 Angstroms [50]. The Boltzmann constant,  $k_B$ , is derived from both the Avogadro's number,  $N_A$ , and the universal gas constant,  $R_u$ , as seen in Equation 14.

$$k_B = \frac{R_u}{N_A} \quad (14)$$

If the Knudsen number is greater than 10, the flow is considered molecular [49]. In addition, for a nozzle analysis the hard-shell diameter should be much smaller than the mean free path, and the mean free path should be much smaller than the critical plane (throat) diameter,  $d_{\text{nozzle}}$ . The diameter of the fired ceramic cylinder,  $D$ , was used as the characteristic length scale for the second Knudsen number. Table 7 displays the values used in these calculations.

**Table 7: Parameter Values Used for Calculating the Knudsen Numbers**

Parameter	Parameter Symbol	Value	Units
Avogadro's Number	$N_A$	$6.022 \times 10^{23}$	$\text{mol}^{-1}$
Argon Gas Constant	$R_u$	8.314	J/mol*K
Boltzmann Constant	$k_B$	$1.381 \times 10^{-23}$	J/K
Argon Hard Shell Diameter	$\sigma$	3.76	Angstroms
Critical Plane (Throat) Diameter	$d_{\text{nozzle}}$	0.4	mm
Containment Cylinder Diameter	$D$	21.75	mm

Using the Knudsen number calculation and a typical range of argon flow rates, a plot was created to show the range of flow rates at which the gas achieves molecular flow at the injection holes. When the Knudsen number is greater than 10, as described previously, the flow was considered molecular. The flow rate that corresponds to this value is shown in Figure 35. The figure demonstrates how the Knudsen number drops exponentially towards a value of 1 as the flow rate increases.

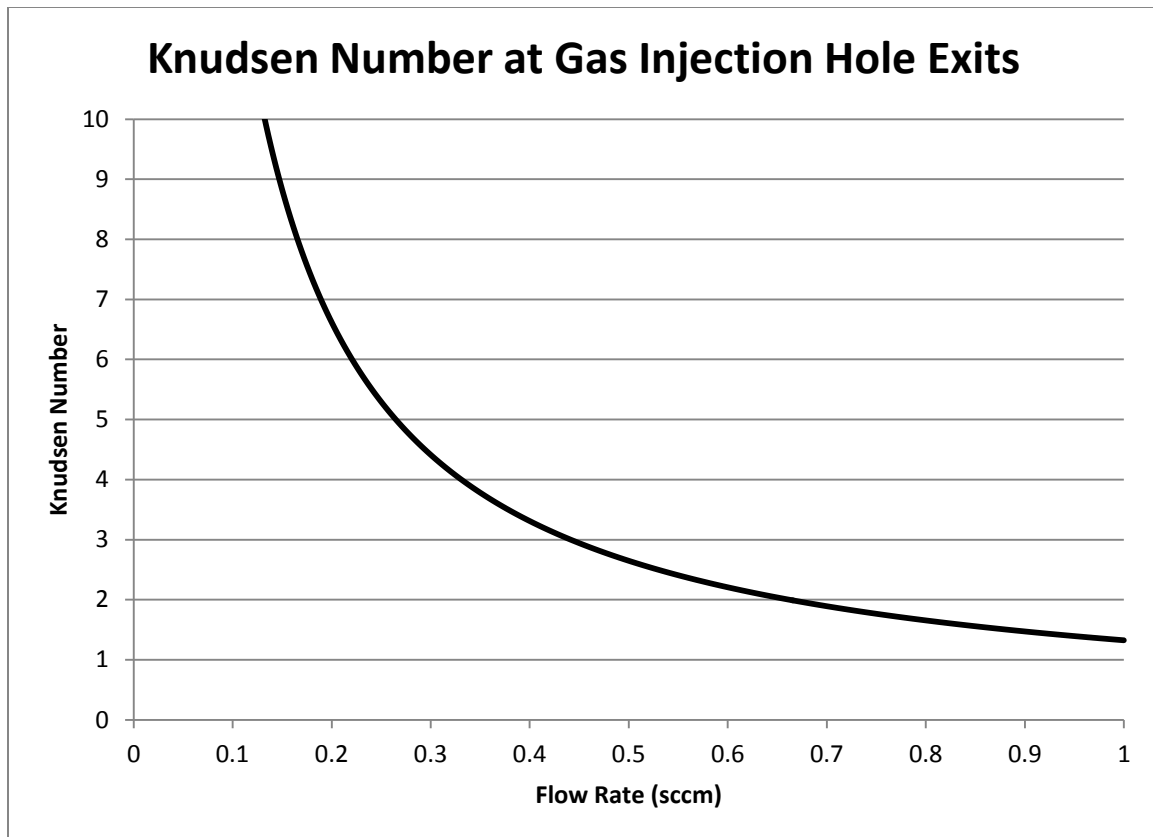


**Figure 35: Plot of Knudsen Number versus Flow Rate for the Gas Injection Hole Exit Locations**

This plot shows that for a flow rate lower than 0.2 sccm, the flow rate would have molecular flow leading into the thruster. The flow rate value for a Knudsen number of 10 was calculated as 0.132 sccm by using a mean free path value of 4 mm in conjunction with Equation 11 and Equation 13. Below this flow rate, the flow will be considered molecular and the equations used for continuity in deriving critical pressure will not hold true, thus a simulated CFD model should not have a flow rate below this value to maintain continuity.

The second location considered for continuum flow as mentioned previously was the exit plane of the cylinder to the vacuum, as it will have the lowest pressure in the



cylinder (nearest location to vacuum). This larger cylinder has an internal diameter of 21.75 mm, which was used as the characteristic length in the Knudsen number calculation. Both the pressure and temperature of the gas in the exit plane location are unknown, thus a range of temperature and pressure values was used to see how the Knudsen number varied with temperature and pressure inputs. A pressure range of 0.01 to 1 mTorr was used for calculations as well as temperatures of 100 K, 220 K, and 293 K. Figure 36 displays the effects of temperature and pressure on the Knudsen number in the thruster containment cylinder. For a constant temperature, as pressure was increased, the Knudsen number decreased. Also, as the temperature was decreased with constant pressure, the Knudsen number decreased.

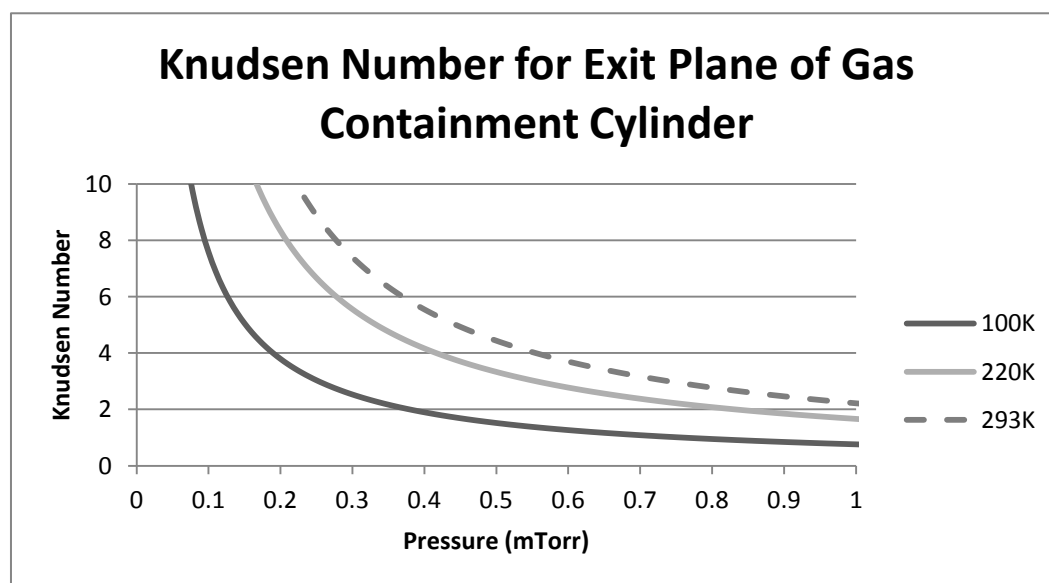


**Figure 36: Knudsen Number Plot of the Thruster Containment Cylinder Exit Plane for Pressures (0.01 mTorr to 1 mTorr) and Temperatures (100K, 220K, and 293K)**

Assuming isentropic flow, the temperature of this region could not be elevated above the reservoir temperature, which explains the maximum temperature of 293 K used

for these calculations. By calculating the Knudsen number at the exit plane, it was seen that molecular flow was reached with gas pressures below 1 mTorr. Equations 12 and 13 as well as the temperature and pressure ranges mentioned at the exit plane of the thruster cylinder were used to calculate the Knudsen number. The mean free path was limited to a function of temperature and pressure, because the characteristic length of the cylinder was a known constant. As can be seen from the figure, the largest temperature value for gas at the exit plane of 293 K is the determining factor for these calculations as it has the largest pressure correlating to the Knudsen number of 10. For a temperature value of 293 K, a calculated pressure value of 0.22 mTorr was found to correlate to a Knudsen number equal to 10. This plot shows that the minimum pressure for continuum flow to be considered in the thruster cylinder is 0.22 mTorr. If experimental pressure data measured inside the thruster containment cylinder is above 0.22 mTorr, it can be assumed that the flow through the thruster up to the measurement point is in the continuum regime. Knowing whether or not the physical thruster is in the continuum regime can help determine whether or not the CFD model at this point in the flow is valid and will be done in Chapter 6.

#### **4-5 Thruster CFD Model Boundary Conditions**

In order to make sure the CFD model adequately portrays the experimental setup, the boundary conditions of the CFD model must be set to match the experimental input conditions. Boundary conditions are requirements of specific regions of a problem that determine how variables are controlled in these regions. They stipulate thermal and fluid flow conditions of the CFD model's inputs and outputs such as mass flow rate, pressure, and temperature. These conditions control the CFD model simulation and also determine

values for solution initialization. The boundary conditions for the CFD model were set at the inlet of the fluid flow as well as the outlet to best match the experimental conditions. A mass flow inlet boundary condition was used for the CFD model, which required temperature and pressure values at the inlet to the thruster. Calculations in the previous sections related a reservoir pressure to the critical plane pressure. The gas inlet location was actually located physically between the reservoir representing stagnant pressure and the critical plane pressure; thus, conditions at the gas inlet location were calculated to better approximate the actual flow. To calculate this intermediate value, a *Mathcad* solver block was used [51]. The equations needed for this calculation were the property relations for isentropic flow of ideal gases for subsonic flow ( $Ma < 1$ ) [44]. The first equation was the ratio of the stagnation pressure in the reservoir to the static pressure in the inlet as seen in Equation 15. The second equation, the ratio of stagnation temperature in the reservoir to static temperature at the gas inlet hole plane, is seen in Equation 16.

$$\frac{P_r}{P_{in}} = \left[ 1 + \left( \frac{k-1}{2} \right) Ma^2 \right]^{\frac{k}{k-1}} \quad (15)$$

$$\frac{T_r}{T_{in}} = 1 + \left( \frac{k-1}{2} \right) Ma^2 \quad (16)$$

The Mach number equation is shown as Equation 17 with known functions for the actual and sonic velocity incorporated. The sonic velocity, Equation 7, is first substituted into the Mach number equation. Density from the ideal gas law, Equation 8, is

substituted into the mass flow rate equation, Equation 10. The mass flow rate equation is then solved for velocity and substituted into the Mach number equation, creating the final form of the equation. In all three of these equations, gas inlet hole notations ( $T_{in}$ ,  $A_{in}$ ,  $P_{in}$ ,  $V_{in}$ ) are used because that is the location of interest.

$$Ma_{in} = \frac{V_{in}}{c} = \frac{\dot{m}RT_{in}}{P_{in}A_{in}\sqrt{kRT_{in}}} \quad (17)$$

The system of equations (Equations 15-17) was solved inside a solver block in *Mathcad* for the inlet properties ( $M_{in}$ ,  $P_{in}$ , and  $T_{in}$ ). Based on a mass flow rate of 100 sccm, known values for the inlet area ( $2.405 \text{ mm}^2$ ), reservoir temperature (293 K), reservoir pressure (14.054 Torr), and critical plane temperature (219.8 K) were used in the solver block. The solver works by taking initial user-supplied guesses for the inlet conditions and slowly changing each of the values until a solution converges. Initial estimates of  $M_{in}$  (0.5),  $P_{in}$  (10 Torr), and  $T_{in}$  (275 K) were used. The solver calculated a gas inlet hole pressure of 13.89 Torr and a temperature of 291.6 K. With the mass flow rate, gas constant, inlet temperature, inlet pressure, and inlet hole area known, a velocity of the gas at the inlet plane could be calculated. This value was calculated to be 37.7 m/s. An initial CFD model was developed with these values as inlet boundary conditions.

#### 4-6 Developing the *Fluent* CFD Model

To develop the CFD model, multiple steps are needed within the program. The first step requires the creation of a physical geometry for analysis. After the geometry is

created, it must be imported into an ANSYS *Fluent* model. With the geometry imported, a mesh, required for finite volume analysis, has to be applied to the geometry. Creating named geometry selections during the meshing process aids in setting up model conditions, which is done next. With the completion of the model conditions, the model can then be run and evaluations of the model made. Properly developing the CFD model is critical to accurately assessing the model against experimental testing.

#### 4-6.1 Geometry Creation

When creating a CFD model in *Fluent*, a physical geometry is required for the CFD model to analyze. This geometry can be created directly in the *ANSYS Workbench DesignModeler* software or in an outside program and imported into *ANSYS Workbench*. For this thesis, the model geometry was created in *SolidWorks* and then imported to *ANSYS*. The geometry was used to represent the region of fluid flow inside the thruster body. The flow regime through the device starts at the LTCC thruster gas hole inlet, travels through the gas manifold and the injection channels, and finally out of the device through the inside of the thruster containment cylinder. This geometry was shown in Figure 32. The flow field geometry, created as a *SolidWorks* part file, was directly imported into *ANSYS Workbench*.

#### 4-6.2 Fluid Flow (*Fluent*) Analysis System Creation in *Workbench*

The fluid flow geometry was imported to *ANSYS Fluent* and the fluid flow model was created. To start the model in *Workbench*, a Fluid Flow (*Fluent*) analysis system was selected. The analysis system was placed into the project schematic in the center of

the workspace. Next, geometry was added with the geometry component system and then linked to the analysis system.

#### 4-6.3 Geometry File Import

*DesignModeler* was used to import the *SolidWorks* part file. Figure 37 shows the *DesignModeler* window displaying the imported *SolidWorks* part file geometry. Once the geometry was imported, the Mesh could be created in the *Workbench Fluent* analysis system.

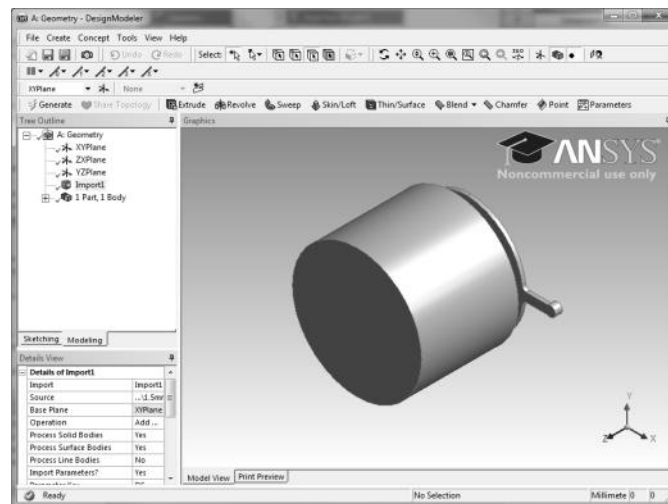


**Figure 37: Screenshot of *DesignModeler* Displaying Imported Geometry**

#### 4-6.4 Mesh Creation

An analysis mesh was created from the imported geometry. A refined mesh based on the default mesh that *Fluent* created for the CFD model was used. The default mesh only had a single element across the height of the distribution channels, which would not accurately capture the boundary layer flow in those regions. With only a single element height, the model will only calculate a single pressure and temperature value per element. Better resolution is needed to accurately see property differences along the height of the

channel. The mesh was refined to allow for more elements in these areas of concern inside the channels. Figure 38 shows a comparison of the regular curvature mesh (left) and refined curvature mesh (right). The refined mesh exhibited a higher density of mesh elements in important locations such as the curves of the rectangular channels as well as the gas injection cylindrical channels. The increase in element resolution allows the model to pick up on finer differences in fluid flow properties.

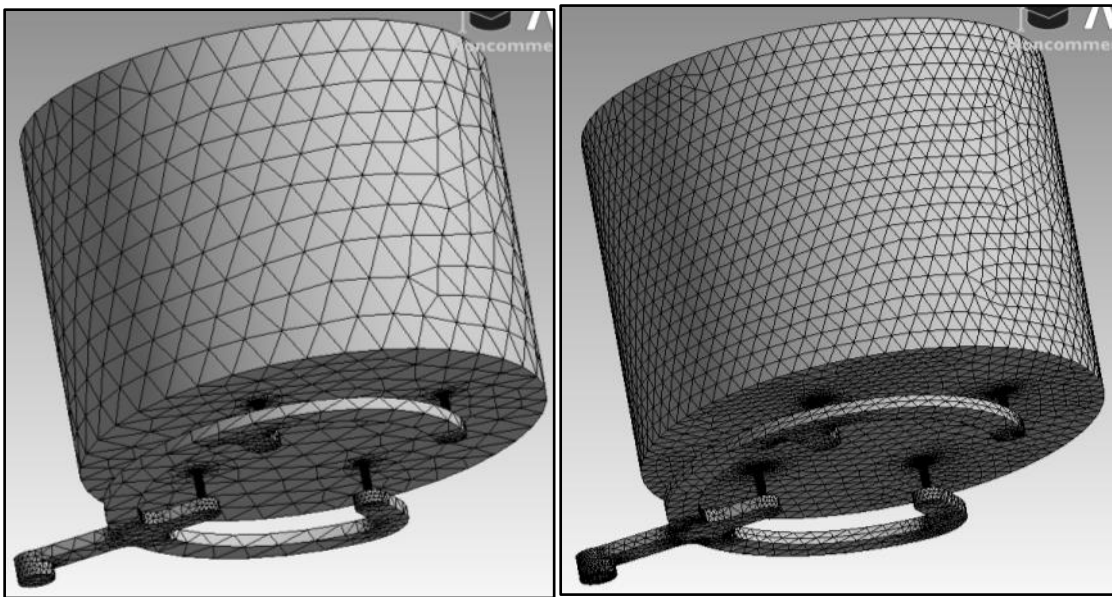


**Figure 38: Basic Mesh (Left) and Refined Mesh (Right)**

#### 4-6.5 Naming Selections

During the meshing stage of the CFD model, named selections were applied. These named selections translated to the setup of the CFD model and made it easier for the classification of specific boundary conditions such as an inlet or outlet. For this CFD model, three named selections were used: inlet, outlet, and walls. These locations can be seen in Figure 39 with the meshed faces showing the named selections. The inlet selection was the face of the gas inlet into the gas manifold and is seen on the left side of

the figure. The outlet was the face at the top of the cylinder that was exposed to the vacuum pressures (center of figure), and the walls were all of the faces of the CFD model that fluid cannot pass through (right side of figure) representing solid structures within the design.

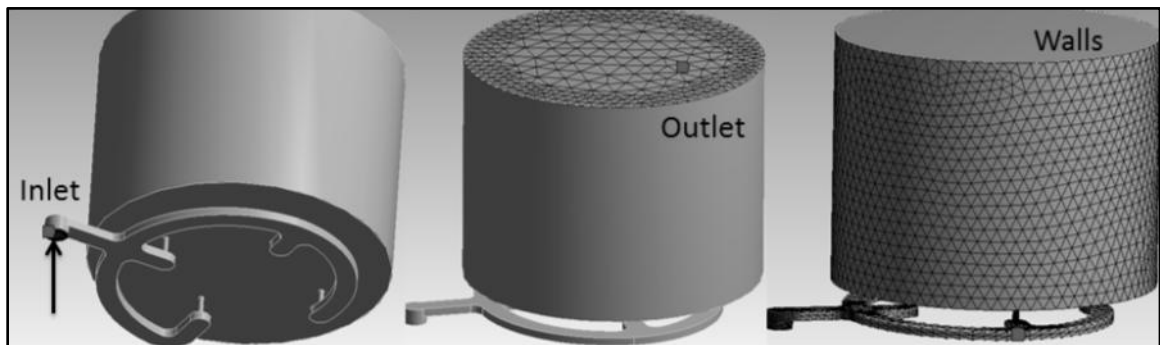


**Figure 39: Named Selections Highlighted by Mesh with the Inlet (Left), Outlet (Middle), and Walls (Right)**

#### 4-6.6 CFD Model Conditions Setup

The next item that required input in the *Workbench* analysis system was the computational model setup. The computational model setup is where the *Fluent* software is introduced into the design of the CFD model. One of the first things done with the setup of *Fluent* was the change of pressure units to Torr, which displayed all pressure data for the CFD model in Torr rather than the regular unit selection of pascals. The following table, Table 8, displays the parameters of the fluid flow model in the *Fluent* simulation. An explanation of the choices will be made after the table.



**Table 8: *Fluent* CFD Model Simulation Chosen Settings**

Section	Parameter	Setting
General	Solver Type	Density-based
Models	Energy	On (Check box)
Materials	Create/Edit	Argon added from <i>Fluent</i> Database
	Density of Argon	Ideal Gas
Cell Zone Conditions	Operating Conditions	0 Torr
	Type	Fluid
	Edit Material Name	Argon
Boundary Conditions (inlet)	Inlet:	Mass-Flow-Inlet
	In the Edit tab: Mass Flow Rate (kg/s)	Set to whatever flow rate is being modeled. (100 sccm is 2.771e-6)
	Initial Gauge Pressure (torr)	Set to whatever value is analytically calculated ( $P_{in}$ value) (13.89 for 100 sccm)
	Flow direction	Set to appropriate direction for the inlet flow (normal to the boundary) ( $x = 1$ in this CFD model)
	In the thermal tab: Total Temperature (k)	Set to the calculated inlet temperature value ( $T_{in}$ value) (291.632 K for 100 sccm)
Boundary Conditions (outlet)	Outlet:	Pressure-Far-Field
	In the Edit tab: Gauge Pressure (torr)	Set to experimental data value for a specific flow rate
	Mach Number	Set fairly low (0.2 used in CFD model)
	Flow direction	Set to the appropriate direction for the outlet flow (normal to boundary) ( $x=1$ in this CFD model)
	In the thermal tab: Total Temperature (k)	Set at least at least as low as the temperature at the critical plane (219 for 100 sccm)

Settings were selected to effectively model the physics of the flow through the device. A density-based CFD model was chosen to make use of the changes in density that will be seen as the fluid makes its way through the system. The energy equation was used to incorporate energy and heat transfer parameters in the CFD model. In the materials section, argon was defined as the working fluid in the CFD model. The ideal gas equation was applied for argon to make use of the compressible flow capabilities that *Fluent* offers. The “Operating Conditions” within *Fluent* were set to 0 Torr because absolute pressure was desired as an output. The cell zone conditions type was set to fluid and argon was selected as the fluid for the cell zone conditions.

Setting boundary conditions correctly was essential to effectively simulate the CFD model. Mass-flow-inlet was chosen for the inlet condition because the inlet in the real system was based on a constant mass flow rate. For the example simulation in this thesis, 100 sccm was used and converted to kg/s. The value of the initial gauge pressure and temperature for the inlet was determined in previous calculations and was required to try to match the conditions of the analytical model. The CFD model needed a flow direction to know which way the flow was approaching the inlet boundary. For a flow starting in a single direction, one value (x,y, or z) has a value of one.

The outlet boundary condition was set to “pressure-far-field” to simulate the background vacuum chamber pressure. An average background vacuum chamber pressure reading was calculated from multiple experimental test runs of gas flow into the chamber with various input flow rates. This data was used when setting a background gauge pressure in the CFD model. This was done to properly simulate the pumping rate of the actual vacuum chamber system used for experimental testing. The CFD model would take a single constant flow rate and attempt to solve a steady-state condition; therefore, the input background pressure was varied only if the flow rate was changed between simulations. This data was based on the pressure readings of the convectron gauge gas pressure. The experimental data for the background pressure versus flow rate can be seen in Figure 40.

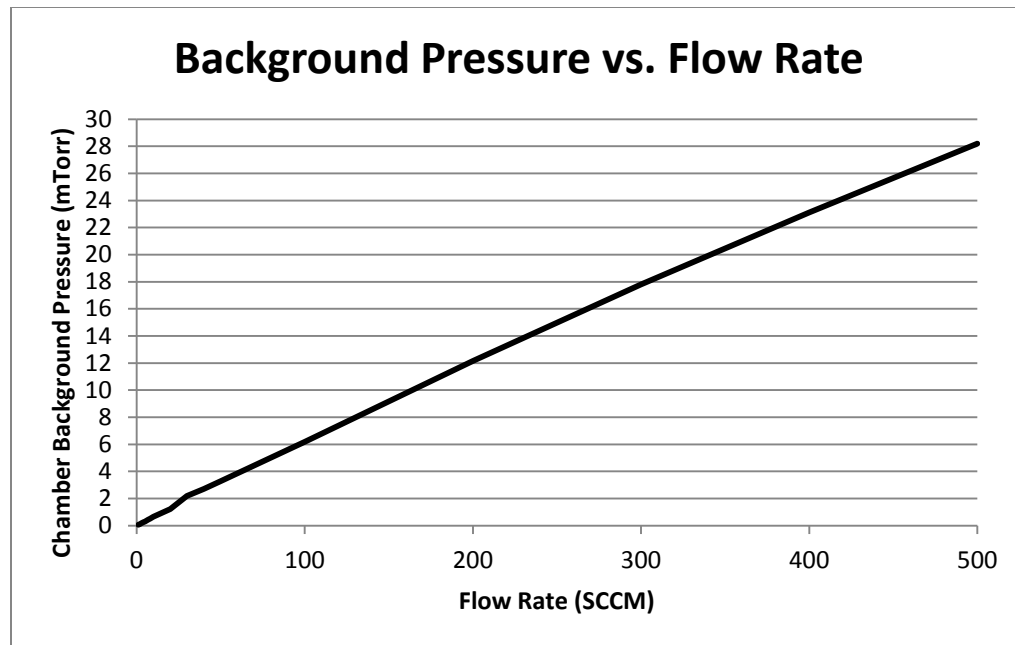


**Figure 40: Background Chamber Pressure versus Flow Rate Data**

The Mach number was set at an arbitrarily low value since the flow would slow down considerably once it encountered the larger area of the thruster cylinder. Flow direction was set similarly to the inlet flow direction. Finally, the temperature of the outlet was set below the critical temperature since the gas will be exhausting into a lower pressure region.

Formulation was set to “explicit” within the solution controls. An explicit approach to the CFD model meant that reference values at the inlet were used to step through the rest of the CFD model at each time step. This was a faster method as it was much simpler than the implicit method, which included a multitude of unknowns rather than a single unknown at each step [52]. The explicit solver is also used when rapid variation in a solution can occur and small time steps are needed. In the case of this simulation, the pressures can quickly change and small time steps are necessary. The

spatial discretization was set as third-order Monotone Upstream-centered Schemes for Conservation Laws (MUSCL). This third-order discretization method for flow gave a more accurate final solution than the first-order or second-order options. The gas inlet values were used to initialize the simulation. The initialization at the gas inlet set where the CFD model began solving for the explicit approach.

To determine convergence of the CFD model, *Fluent* uses residual values for continuity, energy, x velocity, y velocity, and z velocity. A residual is the difference between the sample value and an estimated value of a function. As the residual values converge on the estimated function value, the closer they get to zero. Once the values are all converged, the CFD model is considered to be at steady state. The convergence criteria for these parameters are set at a default value of  $10^{-3}$ .

With all of the parameters and conditions set within the *Fluent* model, multiple simulations could be run at various flow rates. The results of particular CFD models of interest will be presented with other information in the Results section of this thesis.

## CHAPTER 5: THRUSTER FABRICATION

Upon completion of the main design phase, the thruster was fabricated in LTCC. The development of the physical thruster body was an iterative approach, including fabrication, inspection, and design. The first iteration of thruster fabrication will be discussed in greater detail while the later iterations will just describe changes to the fabrication process. An overall flowchart for the thruster fabrication process can be seen in Figure 41.

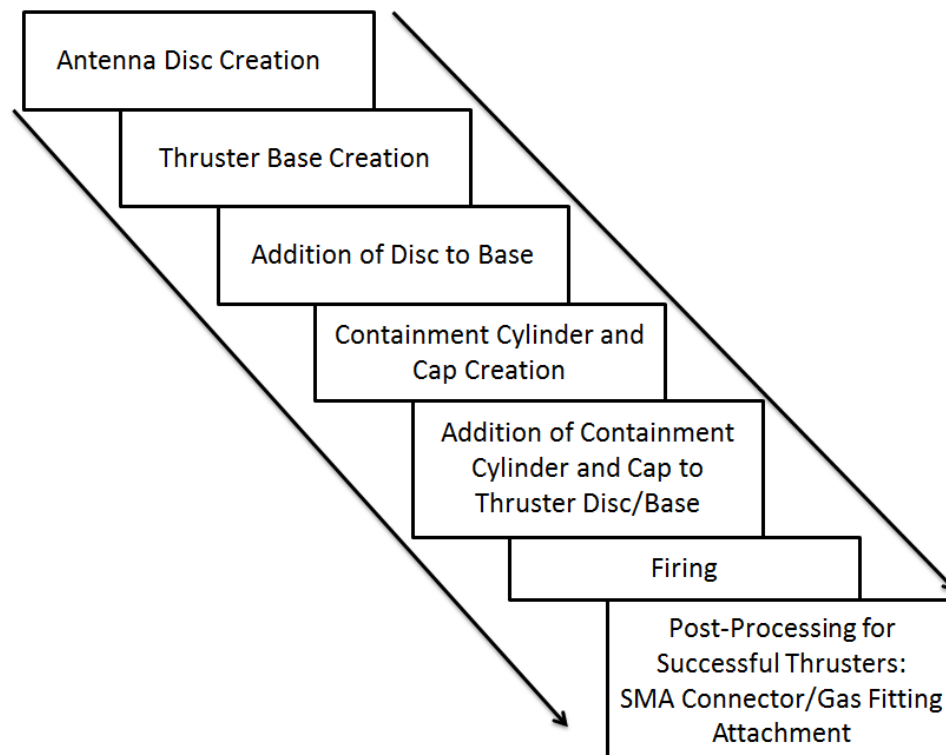


**Figure 41: Flowchart for Thruster Fabrication Process**

### 5-1 Thruster Version 1

The design of the thruster base and antenna disc consisted of 14 layers of Dupont 951 PX LTCC. The antenna disc had four layers (layers 1-4), and the planar base had 10 layers (layers 5-14). An exploded view of the individual layer patterns can be seen in Figure 42. Layers in the figure that are grouped together have the same electric and fluidic features. The thruster fabrication process had multiple stages: creation of the antenna disc, creation of the thruster base, attachment of the antenna disc to the thruster base, installation of the antenna shield layer, creation of the containment cylinder, installation of the containment cylinder to the thruster base, and finally the firing of the thruster body.

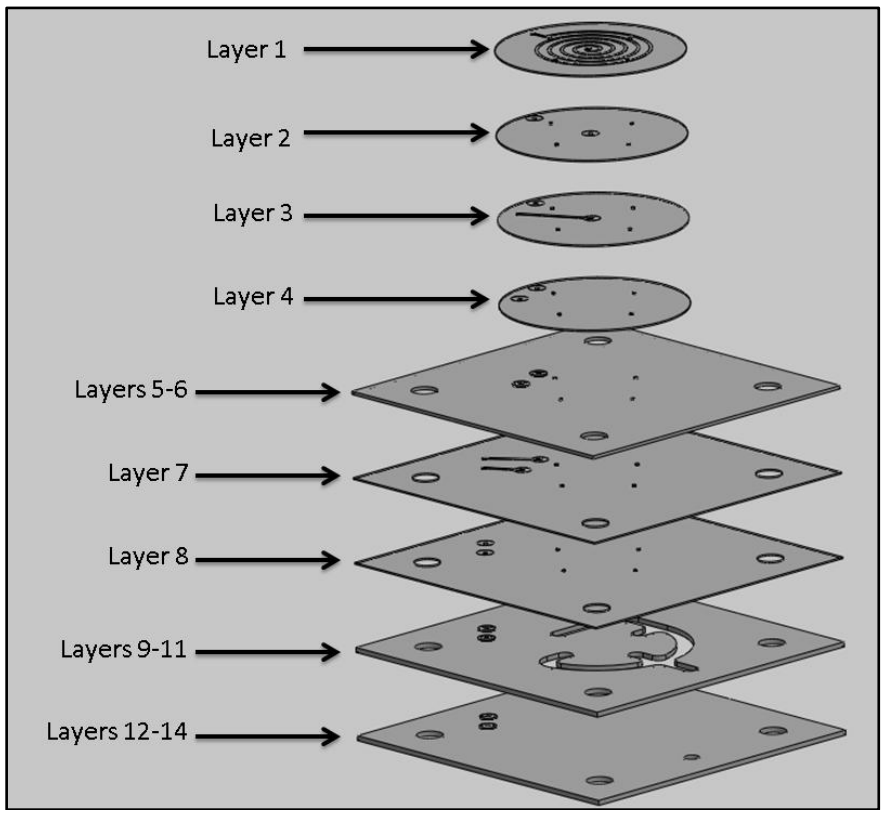


**Figure 42: Exploded View of the Different Layer Patterns of the Thruster Base and Antenna Disc**

The first step in fabrication involved the preparation of the antenna disc. The antenna disc was comprised of four layers of 0.254 mm thick 951 PX LTCC. LTCC layers for the antenna disc were cut with a Universal Laser Systems 30 W laser-milling machine. Once the layers were cut, they were then cleaned and DuPont 6141 (vias) and 6145 (traces) silver conductive pastes were added. The layers were then stacked and pressed in the 20-ton PHI uniaxial lamination press at 70°C and 20.68 MPa. These pressed antenna discs were then stored while the thruster base was fabricated.

The thruster base layers were initially cut with the laser-milling machine. These 10 layers were then cleaned before silver conductive paste was added to each layer. Once the paste was applied, 0.254 mm thick sacrificial carbon (TCS-CARB-1) by Thin Film Technologies was added to the layers containing the lateral channel cavities while stacking and collating the layers. The bottom six layers of the thruster base had a light lamination pressure of 2 MPa applied to create a rigid base with channels to add the carbon. Upon completion of the sacrificial carbon addition, all 10 of the thruster base layers were heated and pressed together. These laminated thruster base layers were then readied for the application of the antenna disc.

The antenna discs were added to the thruster base by using the gas injection holes as alignment holes. These discs had PEOX applied to the back with a lint-free swab while avoiding the holes and silver paste locations. The antenna discs are pressed with light finger pressure to the base while 0.37 mm alignment rods are inserted vertically through the gas injection holes. After 3 minutes, the drill rods were removed from the injection holes. The assembly could now be heated and pressed in the uniaxial lamination press. The desired pressure for this lamination was based on the antenna disc

area. The initial press for 5 minutes was 10% total lamination pressure and then a full lamination press was applied for 10 minutes.

Once the thruster base and antenna disc assembly was laminated, an antenna shield (not shown in Figure 42) was installed. The antenna shield was made from DuPont 50.8  $\mu\text{m}$  thick 951 C2 LTCC (unfired) and was meant to ensure inductive versus capacitive coupling of the plasma. The antenna shield layer also protects the antenna from ion bombardment during plasma generation. This layer was added by cutting out a section of LTCC by hand and then carefully placing the LTCC layer over the antenna. This layer was laminated using a light press with the uniaxial press of 10 percent of the original antenna disc pressure. This pressure was only applied for 5 minutes before the assembly was removed from the press. Once laminated, the assembly was removed from the press and the individual thruster assemblies were separated with the laser-milling machine. The laser only cut through half of the base layers with a fixed height and a utility knife was used to cut through the remaining layers. The separated thruster base and antenna disc assemblies were then placed aside while containment cylinders were created.

The thruster containment cylinders were created by wrapping LTCC around a cylindrical fixture [42]. Two layers of wax paper were wrapped around the fixture prior to the LTCC to allow for easy separation between the LTCC and fixture after lamination. The LTCC had PEOX applied and was wrapped with no visible gaps around the fixture until a desired five-layer thickness was achieved. After wrapping the LTCC around the fixture, the assembly was placed in a vacuum seal bag, which was then vacuum sealed using a KEKO automatic stand vacuum sealer. This bag was then placed into a KEKO



ILS Isostatic Lamination press, which applied 70°C and 20.68 MPa to the LTCC for 10 minutes to laminate it within the bag. The laminated containment cylinder was removed from the fixture and was ready for the addition of an end cap.

The containment cylinder end cap was created to maintain cylinder circularity during firing. The cap consisted of two discs with diameters of 25 mm and 35 mm. Each disc was comprised of four layers of 951 PX LTCC. After the cap layers were cut and laminated, the smaller disc was attached to the center of the larger disc using manually applied PEOX as an adhesive. Boron nitride was then applied to the cap before the cap was placed on one end of the open cylinder. The boron nitride was used to avoid bonding between the cap and the cylinder during firing.

The remaining open end of the containment cylinder was placed on the thruster base and antenna disc assembly. PEOX was applied to the thruster base as well as the antenna disc where the containment cylinder would make contact with the antenna disc. The cylinder was pressed over the disc and a light hand pressure was added to the top of the cylinder to engage the PEOX at the thruster base.

The entire thruster assembly was fired following a standard LTCC firing profile [27]. This firing profile was originally outlined in Section 2-1. The available uniaxial lamination fixture allowed for a total of four thruster bases to be fabricated at one time, therefore Version 1 consisted of four fired thrusters for evaluation.

Fired thrusters were evaluated for verification of a successful fabrication process. When evaluating fabrication results in this thesis, three criteria were used and are listed as follows:

- Visible defects at any point in the fabrication process
- Gas channel leakage
- Electrical connectivity through the thruster

Visible defects of the thrusters included any defects such as cracks in the LTCC substrate. Visible defects were noted and were not considered acceptable as they demonstrated a flaw in the design or fabrication process of the thrusters. The gas channels were considered acceptable if little to no loss in pressure was seen during testing. The electrical conduction through the silver paste of the vias and antenna was considered acceptable only if a continuity test was passed. These criteria will be discussed in the Results sections before ultimately discussing which events may have attributed to the failure of the thrusters.

Successfully fabricated thrusters were post-processed. This process included the application of the external gas fittings and SMA connectors with silver epoxy and ceramic epoxy. This process will be discussed in sections of the applicable thruster versions.

#### 5-1.1 Thruster Version 1 Fabrication Results

Four thrusters were fabricated using the Version 1 design. All four thrusters displayed visible defects after firing, as can be seen in Figure 43. The left side of the figure shows a top view of the thrusters looking down the containment cylinders, while the right side of the figure displays the thrusters from the bottom (control interface) side. The antenna on the top-right of the top view was not covered with the antenna shielding

layer of LTCC because the cylinder was placed on the base before the layer could be added and laminated.

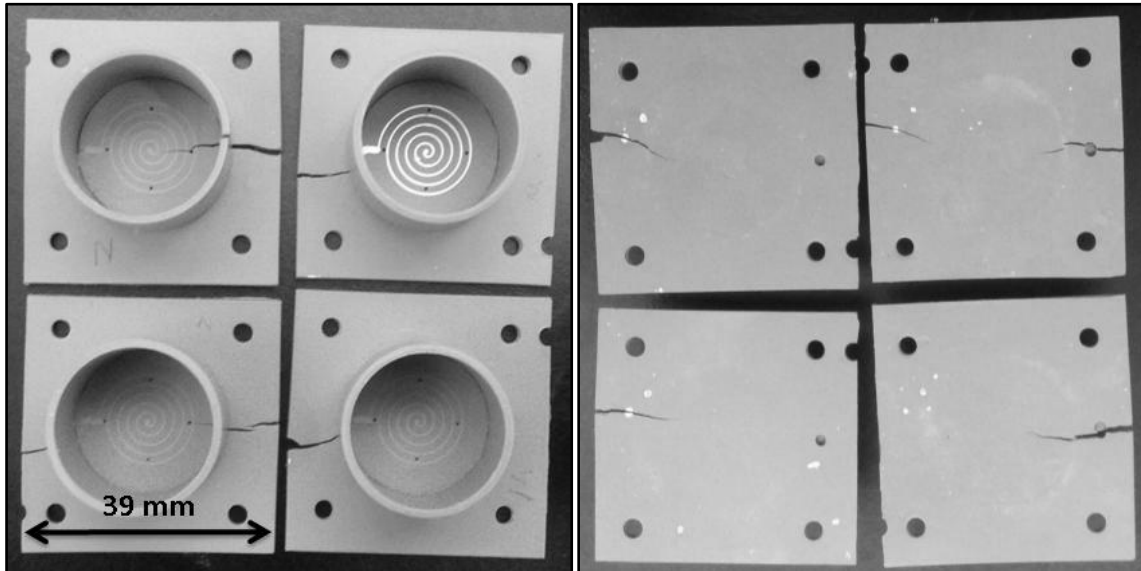


**Figure 43: Thruster Top View (Left) and Bottom View (Right) of Version 1 Thrusters Displaying Cracks that Propagated Through the Thrusters During Firing**

### 5-1.2 Visible Defects

Visible defects were seen during the fabrication process as well as after firing. During the fabrication process, one thruster cracked prior to adding the antenna shielding LTCC layer and two more thrusters cracked after adding the shielding layer. These three thrusters all displayed pre-fired cracks on the thruster base that were between 0.5 and 1 mm wide and at most 5 mm long. All four thrusters displayed cracks after the firing process was complete. Once a crack is formed, the LTCC pulls apart due to the shrinking of the LTCC and the crack is made larger. These cracks propagated through the gas holes as well as through the electrical vias on the bottom of the thruster base. One of the

thrusters had a crack propagate into the antenna disc, which in turn created a crack through the length of the cylinder shown in Figure 44.

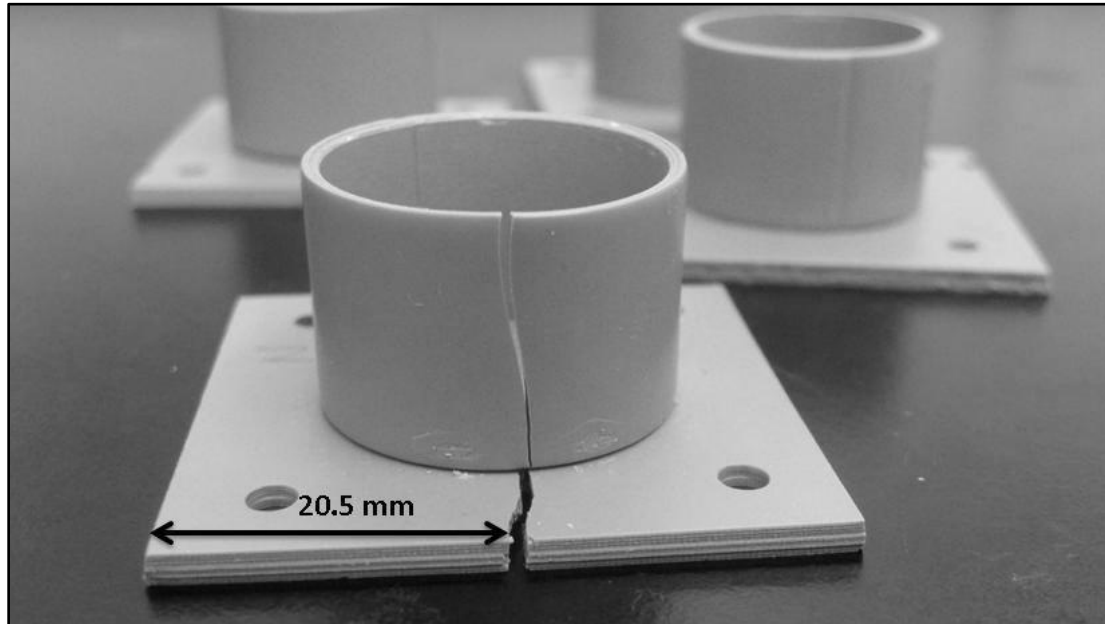


**Figure 44: Crack Propagation through the Length of an LTCC Cylinder**

None of these thrusters successfully passed the visual inspection as they all had cracking. With the cracks appearing immediately after a pressing process in the unfired state, it was suspected that the pressing process could be the cause and should be altered. For the single thruster that had no visible cracks prior to firing, internal cracks could have been present from the pressing process, or another potential source of fracture could have been from the carbon not completely burning out. A change to the firing profile was considered.

### 5-1.3 Gas Flow

The gas flow of the thrusters was the next criteria to be tested. Because of the cracks through the gas inlet holes in two of the thrusters, the gas flow of those thrusters

was deemed unsuccessful as a large loss in propellant pressure would occur from gas leaks. The other two thrusters were checked for leaks by sealing the top of the cylinder and the gas inlet hole on the control interface side of the thruster and applying air pressure. Both of these thrusters displayed leaks during the pressure test, which did not allow pressure to build up inside the thruster. A close up of a crack through a gas inlet hole is shown in Figure 45. It appears the lamination pressure was too high during the installation of the antenna disc to the thruster base.

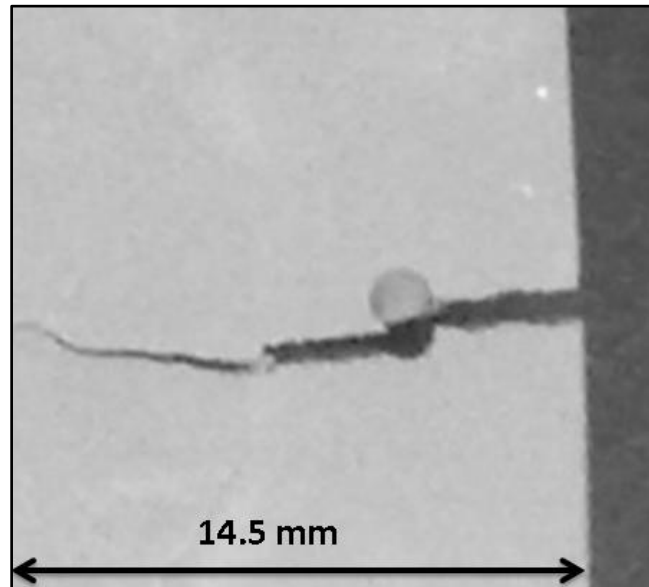


**Figure 45: Close up View of a Crack through the Gas Inlet Hole**

#### 5-1.4 Electrical Connectivity

The next stage of testing the fired thrusters involved checking the electrical connectivity of each thruster. This test demonstrated whether the silver paste was able to successfully conduct through the body of the thruster. When tested for electrical continuity through the antenna, two of the four antennas were electrically connected.

Two likely sources could have been the cause of the electrical connectivity issues. The first potential source was inadequate silver paste placement in the vias when the parts were created. The second potential source was the crack formation in the thruster base propagating through one of the two internal electrical traces inside the thruster, which would sever the connection. Figure 46 shows a close up view of a crack through an electrical via on the control interface side of one of the thrusters.

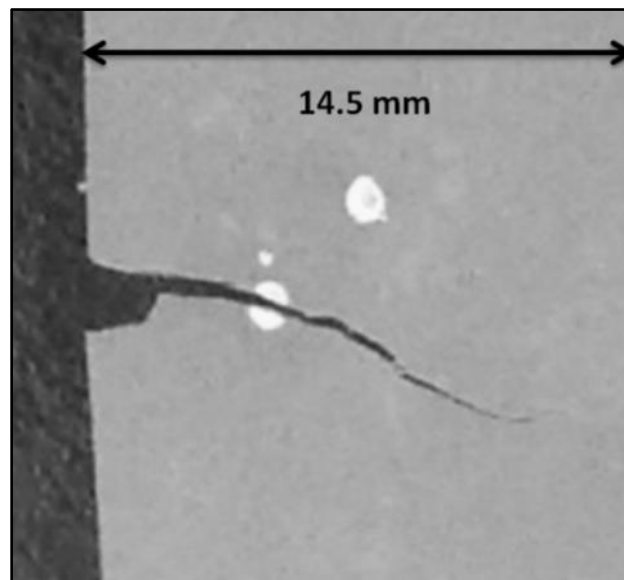


**Figure 46: Close up View of a Crack through an Electrical Via**

Both possible sources of error were evaluated to correct the issue for the next version of thrusters. Alternate pressing methods were looked at as a fix for these electrical issues and are described in the next section.

## **5-2 Thruster Version 2**

Before fabrication of the Version 2 thrusters, improvements were made in the fabrication process to correct the identified Version 1 issues. The main issue with

Version 1 was the cracking present in the thruster bodies. Pressing a single LTCC part more than two times can result in the LTCC drying out and becoming more brittle due to repetitive heating of the part. Pressing the LTCC in this brittle stage can cause cracking as it is not as flexible when it is dried out. A BSU C-MEMS laboratory guideline is to limit the LTCC lamination process to two times per part; such a limitation is difficult with as many lamination steps as are present in the creation of the thrusters.

Another possible reason for the cracking of the LTCC was that the firing profile may not have allowed the carbon to completely burn out of the internal thruster cavities before the sintering process began. Carbon burnout occurs during firing at a temperature of approximately 730°C. Above this temperature, the LTCC substrate begins to sinter and prevent sufficient oxygen from diffusing into the substrate to sustain oxidation of the carbon. The firing profile may not have provided sufficient time for the carbon to oxidize before sintering, leaving carbon in the thruster channels after firing.

After the areas of concern for the Version 1 thrusters were studied, new processes needed to be implemented with Version 2 of the thrusters to avoid repeating the same errors in fabrication. There were three primary changes that were implemented in the Version 2 build:

- Redesigned multiple thruster layout to efficiently use LTCC from new order of 152.4 mm square sheets rather than previous 203.2 mm square sheets. This new sheet size allowed for the creation of three thrusters at a time.
- A single press for the thruster base layers was used.
- Altered firing profile to include an additional dwell at 730°C for one hour.

### 5-2.1 Thruster Version 2 Fabrication Results

Three Version 2 thrusters were fabricated with the new techniques described previously. During fabrication, PEOX was added to the antenna shield layers as a method of holding them in place during the pressing process and avoiding misalignment. The layers were added manually by applying PEOX with a lint-free swab to hold the layers in place on the antenna during the press. This was not successful as the PEOX saturated the 0.05 mm sheets of LTCC. Since these layers were on top of the antenna discs during the press, the saturated layers allowed PEOX to spread to the lamination fixture liner as well as the antenna discs. After the press, the antenna shield layers stuck to the lamination fixture liner and were either completely or partially torn and removed. These results can be seen in Figure 47. The antennas on the right and left sides of the figure were partially exposed and the middle antenna was almost entirely exposed. PEOX will no longer be added while adding the antenna shields to the antenna disc.

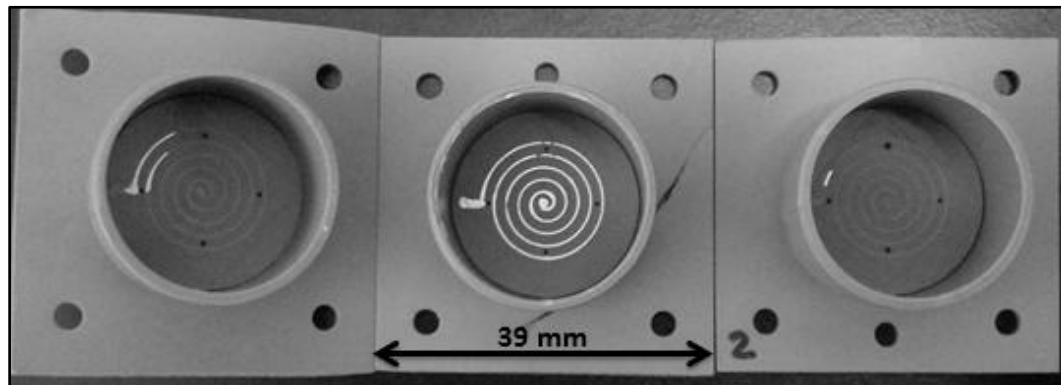


**Figure 47: Second Version Thrusters Showing Antenna Shields Partially and Fully Removed (Left Thruster is Elevated Slightly)**



### 5-2.2 Visible Defects

The three thrusters seen in Figure 47 had fewer and smaller (hairline) cracks than the Version 1 thrusters, which displayed large cracks in all four thrusters.

Circumferential, hairline cracks were located on the control interface side of the thrusters directly behind where the cylinders were placed. These circumferential cracks can be seen in Figure 48. The thruster on the right originally had no detectable cracking, but was mishandled and broken during inspection. The location of the break appeared to originate in the same location as the cracks in the other two thrusters, underneath the interface of the cylinder and the antenna disc. This break in the same location as the circumferential cracks on the other thrusters suggested there may have already been a weak area that formed during LTCC fabrication. All three thrusters still displayed weakness or cracking in the location of the antenna disc. This suggested an improper pressing process as pressure is directly applied in that region from the antenna disc during lamination. The carbon appeared to be completely oxidized and there was no evidence that the cracking could still be caused by the carbon. Further refinement on the pressing process would be implemented on the next version of the thruster.

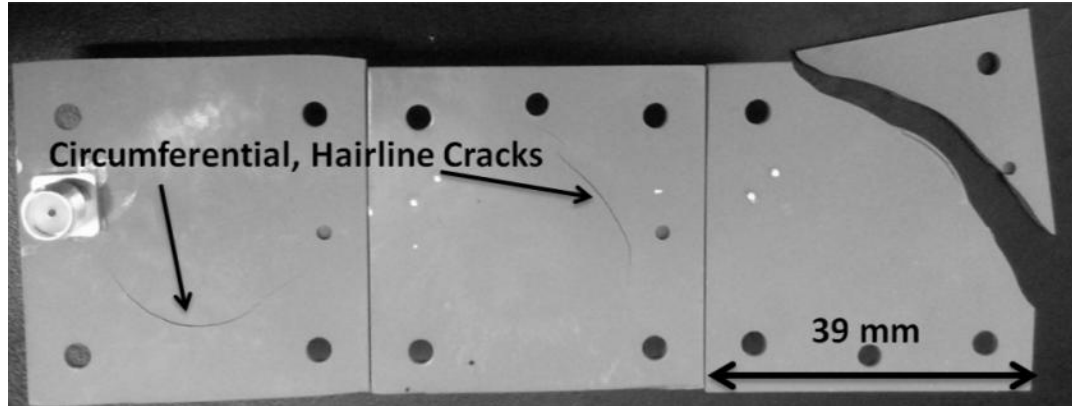


**Figure 48: Back Side of Second Version Thrusters Displaying Cracks (Left Thruster Has an SMA Connector Attached to Test Silver Epoxy Bond Strength)**

### 5-2.3 Gas Flow

Testing the thrusters for proper gas flow was done prior to the mishandling of the third thruster. After testing the three thrusters for leaks, it was determined that only one of the three thrusters could maintain a gas pressure inside the propellant channels (two had leaks). The two thrusters shown to the left on Figure 48 both had leaks through the small visible cracks. Figure 49 shows a closer view of the crack on one of the Version 2 thrusters. These cracks appeared to follow the shape of the antenna disc. This indicated the antenna disc was creating too much pressure when pressed onto the base layers. This pressure was near the internal gas channels, which created stress fractures in the LTCC. A change in the applied pressure during the antenna disc application for the Version 3 thrusters would be needed to prevent cracking.

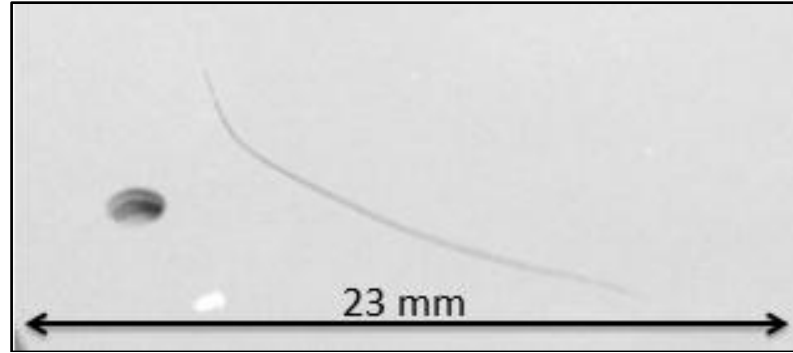


**Figure 49: Close Up View of Hairline Crack by Gas Inlet on a Version 2 Thruster**

#### 5-2.4 Electrical Connectivity

When testing the thrusters, all three of the Version 2 thrusters had no electrical connectivity through the antenna. Inspection of the antenna spirals showed there were no breaks or gaps with the antenna spiral traces; therefore, the problem had to be located internally. The cracks that were present did not appear to be located near any electrical components in the Version 2 thrusters. It was assumed that the connectivity issues must lie within the fabrication process. A more accurate method of applying silver paste would be needed for Version 3 to prevent the chance of an improperly filled electrical via. Also the silver paste should be sufficiently dry before lamination to try and prevent any connectivity issues formed during pressing the thruster bases. Fabrication of the Version 3 thrusters addressed some of the mentioned changes to correct the structural and electrical issues.

#### **5-3 Thruster Version 3**

The cracking noticed in the Version 2 thrusters appeared to be caused by excessive pressing; thus, less pressure, a shorter pressing time, or a revision in the

process was deemed necessary for Version 3. A revised three-step process was developed for the antenna disc rather than the previous two-step process consisting of a preheat cycle and a full-press cycle. This revised process eliminated the additional lamination step by attaching the antenna shield after the base had been pressed with the antenna disc. The new process incorporated a first pressing step for the antenna disc of a 10% press for 5 minutes, a second step of pressing 90% of the laminating pressure for 8 minutes, and a final step of adding the antenna shield layer and pressing for 10% pressure for an additional 5 minutes. This process was done as quickly as possible to retain as much heat in the LTCC as possible, which would reduce the preheat time prior to lamination.

The electrical connections required a new process that would give a much higher success rate for connectivity and repeatability. Two approaches were used to address the electrical continuity during fabrication. The first approach was the application of a new technique when the printed LTCC layers were removed from the stencil fixture. Originally, the layers were raised vertically to keep the silver paste from spreading across the LTCC. The new technique used a lateral slide of the LTCC prior to lifting the LTCC vertically from the fixture. This new technique broke the bond of the silver paste to the fixture prior to lifting the LTCC, which reduced the amount of silver that was removed from the LTCC via holes. This technique left more silver paste available for electrical conductivity through the thruster.

The second approach to correct the electrical continuity was changing the application of the PEOX between the antenna disc and the thruster base to secure a good lamination between the two parts. In the previous process, PEOX was applied near the

center of the antenna disc in a cross shape to avoid getting any PEOX on the silver paste or in the gas injection holes. A new process for adding PEOX was applying it to the entire section of the antenna disc that would come in contact with the thruster base. The evenly distributed PEOX was meant to create a better lamination of the two parts, which would improve electrical connectivity between the parts. The reason this process was not employed in previous thruster versions was the concern that the PEOX would interfere with electrical connectivity if it were used between the electrical vias.

A summary list of the major changes for the Version 3 thrusters are as follows:

- A revised pressing process to include a three-step press.
- A lateral slide technique prior to lifting stenciled LTCC sheets.
- A complete coating of PEOX on the reverse side of the antenna disc.

### 5-3.1 Thruster Version 3 Fabrication Results

The Version 3 thrusters were more successful than the previous versions. Some cracking was still present on all three thrusters circumferentially in the base directly below the cylinder as seen in the previous versions, but the cracks had no noticeable negative effects on the thrusters. These thrusters were used in testing as they proved to have both good gas flow and electrical connectivity. After these Version 3 thrusters were tested, gas fittings and SMA connectors were attached.

### 5-3.2 Visible Defects

As mentioned above, all three of the thrusters had circumferential cracks in the base of the thruster. These cracks were very similar to the cracks from Version 2 in size and shape. They had a rounded shape that followed the cylinder and antenna disc shape.

These hairline cracks occurred either on the top or the bottom of the thruster bases. These cracks however didn't appear to be severely detrimental to the thruster functionality. One of the cracks on the backside of one of the thrusters can be seen in Figure 50 **Error! Reference source not found..**

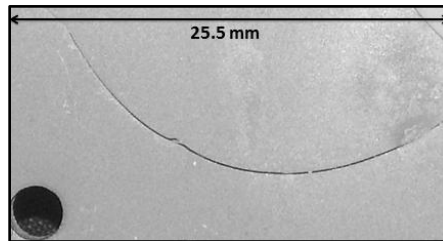


**Figure 50: Crack Located on the Control Interface Side of a Version 3 Thruster**

### 5-3.3 Gas Flow

The three Version 3 thrusters were checked for leaks and one of the three thrusters had no leaks. The other two thrusters had minor leaks through the cracks in the base that were present. The leaks into the cracks were thought to be small enough that the thrusters could still be usable by sealing the crack with LOCTITE Hysol 1C ceramic epoxy. The ceramic epoxy consists of a hardener and a resin that were mixed in equal parts. The epoxy was placed on the crack; the excess was wiped away, and then it was cured in the oven for two hours at 65°C. The two thrusters were then tested and both passed the leak test as well as an additional test to ensure they still allowed gas flow. Figure 51 shows one of the thruster's cracks filled with the white ceramic epoxy.

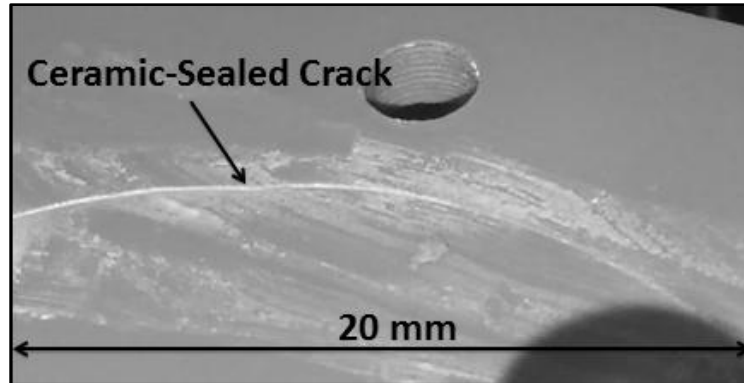


**Figure 51: Version Three Thruster Crack Filled with Ceramic Epoxy**

#### 5-3.4 Electrical Connectivity

The electrical connectivity issues from previous versions were corrected with Version 3. All three thrusters in this version had successful tests. The difference with the PEOX addition to the disc prior to placing on the base did not affect the connectivity of the internal electric vias. The technique of completely covering the base of the discs, including the electrical vias, with PEOX was incorporated with all future thruster fabrications made from this point forward. The lateral shift technique used when removing printed LTCC from the stencil fixture appeared to solve the main issue of the lack of electrical connectivity seen in the previous two versions.

#### 5-3.5 Version 3 Thrusters: Post-Processing

The Version 3 thrusters were able to be used for vacuum chamber experiments. With the proper functionality of the electrical connections as well as the gas channels, the thrusters were moved into the next phase of fabrication to ready the thrusters for testing. For testing purposes, the thrusters needed a gas fitting and an SMA connector. The installation of these two items is discussed in the next two sections.

A silver conductive epoxy by MG Chemicals (8331-146) was used for attachment of the SMA connector to the base, physically and conductively. It did not have enough bonding strength by itself, thus additional support was required. The silver epoxy created a good electrical connection from the thruster base to the SMA connector, which was tested by checking continuity between the epoxy and the connector. The SMA connector can be seen up close on the thruster in Figure 52.

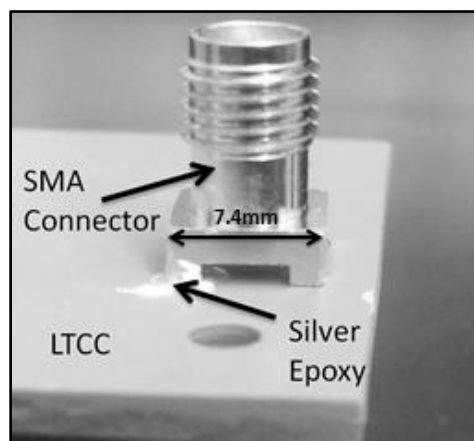


**Figure 52: Close up View of SMA Connector Showing Silver Epoxy**

The silver epoxy had a low viscosity, and had to be carefully applied to the thruster base. The epoxy was applied with the end of a small wooden dowel. Too much epoxy could be applied in a single application, which then would spread out during the curing process in the drying oven (10 minutes at 65°C). The epoxy on the center pin and the outer leg could merge together and create an electrical short.

As mentioned, the SMA connector needed additional support to allow for the cable to attach without breaking the silver epoxy connection. The ceramic epoxy was an effective adhesive that could provide the necessary bonding strength and was used to



secure the SMA connector in place. The ceramic epoxy was applied around the legs of the SMA connector. The silver epoxy around the one leg was directly covered by the ceramic epoxy. To avoid any chances of out-gassing, one side of the SMA connector had no ceramic epoxy applied. This left an opening to the middle pin of the connector, which removed the chance of having an area of atmospheric pressure under the connector when it was in the vacuum chamber. The ceramic epoxy was then cured in the oven for the required two hours. The SMA connector connected with silver epoxy as well as ceramic epoxy can be seen in Figure 53.

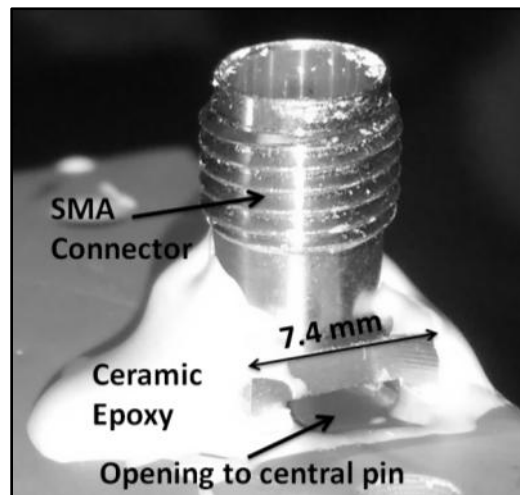


**Figure 53: SMA Connector Applied with Both Silver Epoxy and Ceramic Epoxy**

The gas fitting attachment used for these thrusters was a Swagelok Weld Connector with a 1/8" tube outer diameter and weld size. This fitting was used because it had a flat end that could be directly bonded to the LTCC substrate around the gas inlet hole on the control interface side of the thruster body. The gas fitting attachment was approached with the same technique as the SMA connector. Ceramic epoxy was applied between the base of the gas fitting and the LTCC substrate to create a secure connection

to the thruster body. The gas fitting was visually placed to make sure the gas inlet to the thruster was located in the center of the end of the gas fitting. The inside diameter of the fitting was larger than the inlet hole on the LTCC thruster base, which made alignment a manual task. The whole thruster was placed into the oven and the epoxy was cured for two hours. One of the attached gas fittings can be seen in Figure 54.

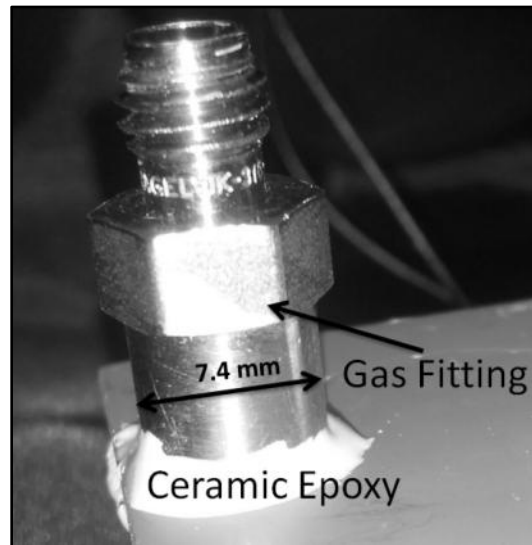


**Figure 54: Gas Fitting Attached to the Backside of a Version Three Thruster**

All three Version 3 thrusters were tested in the vacuum chamber and plasma was formed with all three thrusters, validating the function of the design and fabrication. The incorporated gas channels successfully supplied gas to the thruster cylinder from the gas line and the antenna supplied RF power to generate plasma with the LTCC thruster. While the Version 3 thrusters were usable, there was still the issue of cracking on the thruster base that needed to be addressed in Version 4.

#### 5-4 Thruster Version 4

The Version 3 thrusters had been tested for their ability to generate plasma and the design proved to work, but further refinements were needed to completely eliminate the cracking that was present in the base of the thruster. The cracking appeared to be less about the pressure of the pressing process and more about the actual geometry of the thruster itself. The propellant channels ran through the thruster in approximately the same location where the disc was applied to the top. It was proposed that where the disc was being pressed onto the base, there was a location with a large shearing stress concentrated on a few layers between the disc and the top of the propellant channel. The geometry in question can be seen in Figure 55.

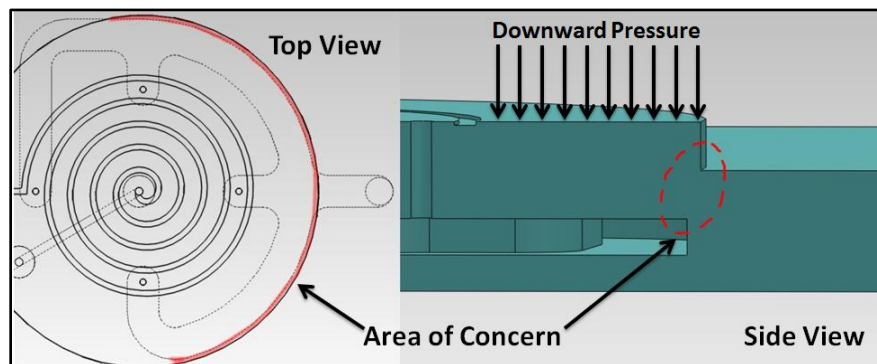


**Figure 55: Top View (Left) and Section View (Right) of the Area of High Stress Concentration during Pressing**

The left view on the figure shows the area of concern in red. The outer diameter of the gas channel and the diameter of the raised antenna disc above are virtually concentric. The sectional view on the right shows the area of LTCC that could be cracking to the downward pressure during lamination. The downward arrows display the direction of the lamination pressure applied to the antenna disc. To correct this issue, the

design of the channel was narrowed to 1.5 mm and moved inward towards the center of the thruster base. This change increased the amount of LTCC laterally between the outer diameter of the propellant channel and the outer diameter of the antenna disc and dissipated the shear load through the structure.

Thermal gradients during the firing process were still a concern because of the highly irregular geometry of the device. For thruster Version 4, additional modification was made to the firing profile to minimize thermal stresses, which could cause cracking. If the outside of the thruster was heating up well before the center of the thruster, a thermal expansion difference could contribute to the cracking in the thruster base. As the part was much wider than it was tall, most of the stresses would be seen laterally along the part. To correct this issue, a new firing profile was developed that added a temperature dwell at 700°C (to replace the previous 730°C dwell) for one hour. The new profile also included a temperature dwell at 800°C for 30 minutes before the sintering temperature of the LTCC (850°C) was reached. With a new firing profile as well as a new design for the internal channels, Version 4 of the thruster was fabricated.

The Version 3 thrusters were all functional, therefore additional thrusters were not immediately needed for testing purposes; however, the thrusters were needed for the pressure-testing device used in this thesis to properly simulate the internal gas manifold. The Version 4 thrusters were created for that purpose and therefore did not need to include the cylinders as the pressure-testing device simulates the cylinder of a thruster.

A summary list of the Version 4 fabrication process changes is as follows:

- Internal gas channels were narrowed to 1.5 mm width.
- Internal gas channels were moved radially inward.

- The firing profile was altered to replace a single dwell at 730°C with two dwells, one at 700°C and another at 800°C.

#### 5-4.1 Thruster Version 4 Fabrication Results

A new process was introduced to the end of the fabrication cycle for these thrusters. A final step was added just before firing that consisted of applying two 4 square millimeter sections of silver paste to the vias on the backside of the thrusters. The silver paste was placed to enlarge the area of each of the vias that connect to the SMA connector. This change was made to increase the surface area of the silver connection pads on the surface of the LTCC substrate to aid in lining up the SMA connector and making a good electrical connection. The thrusters were then installed as before with the base flat on the alumina firing squares in the furnace. Once fired, the thrusters were assessed for any defects or loss of functionality.

#### 5-4.2 Visible Defects

All three of the thrusters were produced without any visible cracks. The cracking was resolved by changing the design of the channels, adjusting the firing profile, not adding the thruster cylinders, or by a combination of these options. Two of the three shield layers were slightly small and left a small section of the antennas exposed. This was not an issue for these thrusters because they were planned as pressure-testing devices and only the gas flow was needed. One of the thrusters can be seen in Figure 56 with both a top (left) and a bottom (right) view of the thruster.

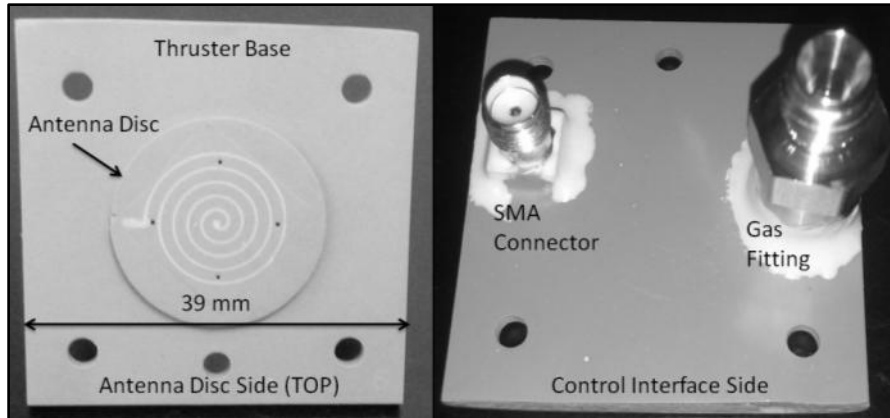


**Figure 56: Version 4 Thruster without Thruster Cylinder, Showing the Top View (Left) and the Bottom View (Right)**

#### 5-4.3 Gas Flow and Electrical Connectivity

The gas flow appeared to work properly for these thrusters. The electrical connections were functional in each thruster device. The larger silver pads on the bottom were successful as they aided in attachment of the SMA connectors by helping with alignment of the connector to the vias.

#### **5-5 Final Thoughts on Fabrication Process**

The Version 4 fabrication process produced the best result from all thruster versions and only a single item should be changed with the process in the future. The antenna shield layers should be cut with the laser if possible to increase repeatability in fabrication. The antenna shield could have a circular shape rather than the square shape made with the first four versions of these thrusters. The circular shape would be simpler to align on the antenna and to ensure full coverage prior to the final press of the discs. A comparison of the initial solid model design of the thrusters and actual fabricated results is shown in Figure 57 and Figure 58.

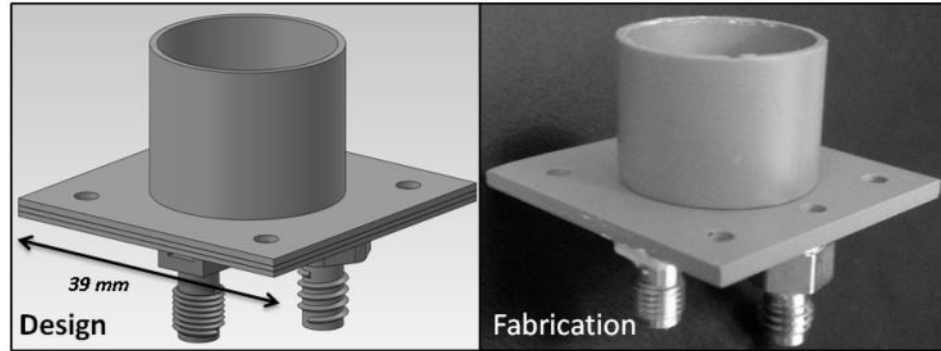


**Figure 57: Solid Model Design (Left) and Fabricated (Right) Whole Thruster Body Comparison**

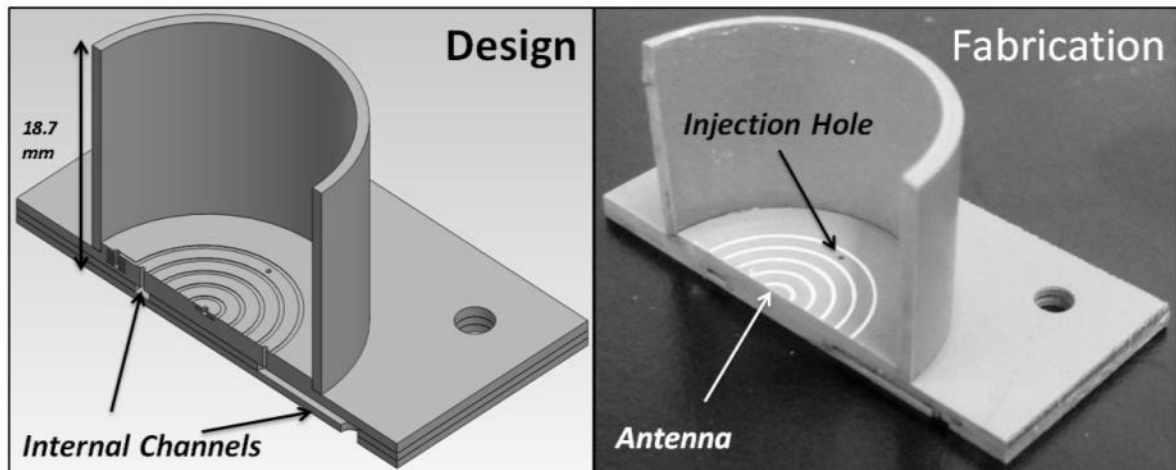


**Figure 58: Comparison of a Sectional View of the Solid Model (Left) and the Fabricated Thrusters (Right)**

An overview of the results of the fabrication was documented. The four thruster versions were compared for the number fabricated, visible defects before and after firing, gas leaks, electrical connectivity, and ability to be used in experiments. These results can be seen in Table 9. As can be seen in the table, the fabrication process was improved dramatically from Version 1 to Version 4. The Version 4 thrusters were all functional for experimental pressure tests.

**Table 9: Overview of Thruster Fabrication Results for Version 1 through Version 4**

Version #	Number Fabricated	Visible Defects Before Firing	Visible Defects After Firing	Gas Leaks	Poor Electrical Connection	Usable for Thrust Measurement Experiments	Changes to Fabrication Process
Version 1	4	3	4	4	2	0	--
Version 2	3	0	2	2	3	0	Single Base Press, New Firing Profile, New Design Layout
Version 3	3	0	3	2 (fixed)	0	3	Revised Pressing Process, Lateral Slide Stencil Technique, PEOX Addition to Entire Disc
Version 4	3	0	0	0	0	3	Firing Profile Change, Internal Gas Channels Narrowed and Moved Radially Inward



## CHAPTER 6: THRUSTER TESTING AND RESULTS

This chapter discusses the mass flow controller setup as well as the pressure-testing device and how it was used in experimental testing. Also discussed will be the testing process, the experimental results, and the CFD modeling results. The experimental results will be compared to the CFD modeling results to verify the CFD model for future thruster configurations. Appendix A contains a list of detailed information regarding the readying of the vacuum chamber for these tests as well as information about the entire experimental setup.

### 6-1 Variable Mass Flow Rate Setup

The mass flow setup for the testing of thrusters was required to have accurate flow control of gas up to 500 sccm to test thrusters. In order to achieve accurate flow through this entire range, multiple mass flow controllers were needed.

The first mass flow controller (MFC) added to the system, a Horiba Stec STEC-Z512, was capable of accurate flow as low as 0.08 sccm to 4 sccm of argon. This MFC was thought to be the most important controller for sustaining plasma as previous tests had shown the ability to maintain plasma generation with gas flow in the few sccm range. The second mass flow controller added to the system, a Porter 201 Series, was capable of a 0 to 28 sccm of argon flow, but it had limited accuracy at the upper and lower flow rate limits. A third and final mass flow controller, another Porter 201 Series, was capable of a 500 sccm maximum flow rate of argon. These three flow controllers gave 3 different

ranges of accuracy for testing thrusters and a combined accurate flow range of 0.08 to 500 sccm. The simplified flow schematic from the supply to the thruster can be seen in Figure 59.

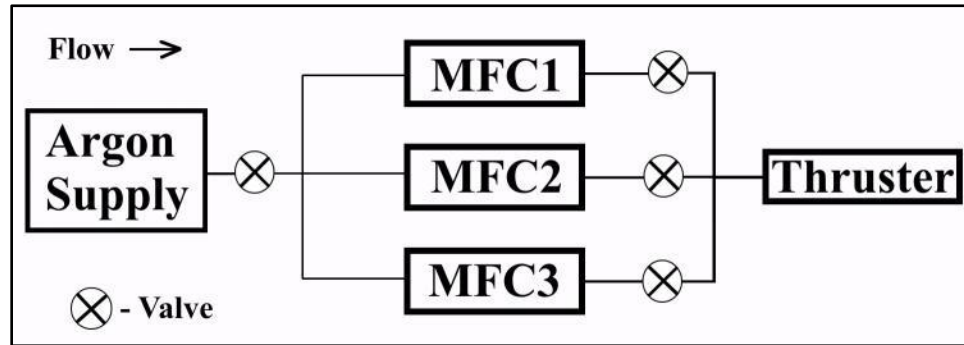


**Figure 59: Simplified Flow Schematic from Argon Supply to Thruster or Pressure-Testing Device**

In order to design this variable mass flow setup, an estimated footprint was needed for all three mass flow controllers and the associated tubing that would connect them to the system. Swagelok valves and fittings were used to add these MFCs into the system; thus, Swagelok recommendations were used with entrance tube lengths [53]. The recommendations state that when having a tube bend near a fitting, there should be at least 20.6 mm of straight tubing before the end of the tube that will house the fitting. With this value in mind, a setup was designed to take up as little space as possible. A two-way valve was included after each controller to shut off each branch when it was not in use to minimize leaks. With a single argon gas line feeding the system, a splitter was needed that would split the single line into three lines to feed all three controllers. Beyond the flow controllers, another fitting was needed to merge the three lines back into

a single gas line feeding the vacuum chamber. The front and back of the variable mass flow controller setup can be seen in Figure 60.



**Figure 60: Variable Range Mass Flow Controller Setup: Front View (Left) Back View (Right)**

The three controllers were attached to a plate with holes for the valve handles to fit through. The three valves and the bolts holding the controllers to the plate are all that are visible from the front. The back side of the setup shows all three mass flow controllers as well the main gas flow path where the line splits and re-merges. The three valves simply have an on and off position for when specific controllers are in use.

*LabVIEW* Virtual Instrument (VI) software on a lab computer controls the MFCs [54]. The software needed to be modified to incorporate all three mass flow controllers. Two separate computer controls were created on the front panel of the *LabVIEW* interface that allowed for management of all three controllers depending on which flow rate range was chosen for the thruster. The first computer control only governed the low flow range MFC with increment resolution of one hundredth of a sccm. The second computer control changed between the remaining two MFCs depending on which flow range was desired. From 4.1-28 sccm, the 28 sccm MFC provided the mass flow rate, while the range above 28 sccm the mass flow was provided by the 500 sccm controller. This second computer control had an increment resolution of 1 sccm. Finer resolution was achieved by manually entering the desired value into the control.

## **6-2 Second Version Pressure-Testing Device**

A new pressure-testing device was needed that would incorporate the fluid channels and four gas injection points of the new thruster design. This device was used to compare experimental data between the one hole and four hole thrusters as well as provide preliminary vacuum pressure data for a fluid simulation. A device was needed that could incorporate an existing LTCC thruster body. The thruster body would be similar in every way minus the thruster cylinder. The pressure device would fit over the circular antenna disc layers of the thruster and be clamped to the thruster base. The testing device would simulate the thruster cylinder while allowing measurement of the local pressure.

The new testing device needed to measure pressure at various levels above the antenna similarly to the previous pressure-testing device. It was decided that a spacer

technique would be used to adjust the height of the pressure tap hole. This device would use two spacers that could be placed either on top of the device or below the device that would maintain a consistent cylinder length while allowing three different heights for pressure measurement data. This spacer approach allowed the use of only a single pressure tap, which would simplify the design and fabrication of the device. The thickness of the spacers was not critical as long as they were defined for the pressure at a specific height to be measured and compared with simulated data. Figure 61 shows the solid model design of the new pressure-testing device. As can be seen on the figure, there are four alignment holes to match the thruster body design. The pressure tap can be seen on the right side of the device with a path leading to the cylinder. Also notice the two spacers are on the bottom of the device in this configuration.

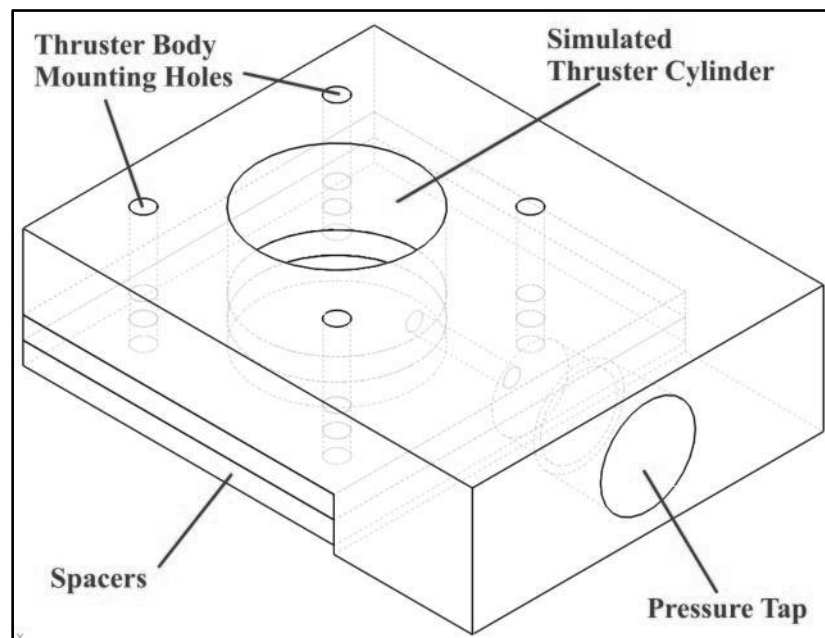


**Figure 61: Second Version of the Pressure-Testing Device**

The pressure-testing device was fabricated using Delrin plastic for its vacuum compatibility. A quarter inch gas fitting was threaded into the pressure tap with Teflon

tape to prevent gas leakage. The finished device can be seen in Figure 62. The picture on the left side of the figure shows the device from above to highlight the pressure tap in the cylinder hole wall as well as the location of the antenna inside the device. The picture on the right of the figure shows the gas line connected to the pressure-testing device while it was installed in the vacuum chamber.

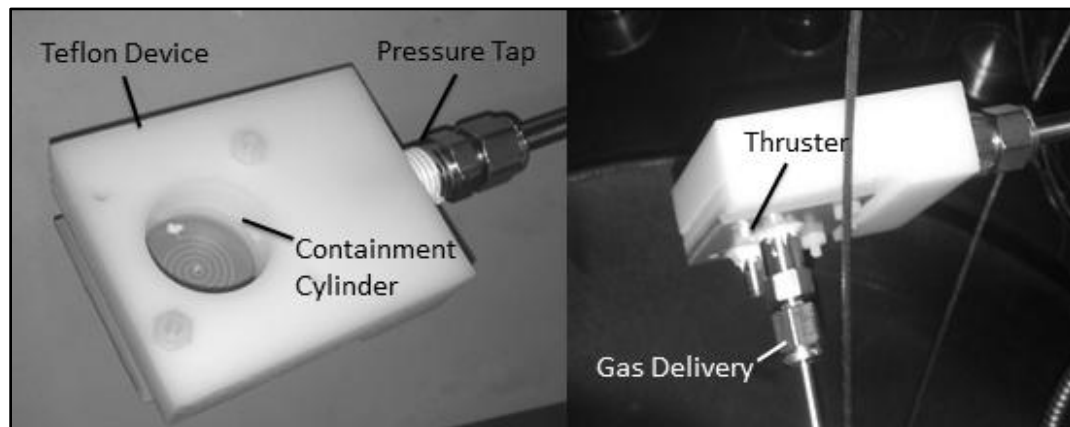


**Figure 62: Finished Experimental Pressure-Testing Apparatus Shown from Above (Left) and from the Bottom (Right)**

### 6-3 Single Hole Thruster Body Design

This section is an overview of the creation of some single hole thruster bodies that were created to test with the pressure-testing device. These single hole thrusters were needed to make a comparison experimentally to determine if the four hole design was better at producing a localized pressure inside the thruster cylinder. The fabrication process for these thrusters was the same as the final process used for the fourth version of the four hole thrusters. The only difference in the fabrication process for these new thrusters was a new design for the fluid delivery. The laser patterns as well as the carbon cutout patterns needed to be created for the single hole thrusters. When designing the

channels, the same dimensions for width and height were used (2 mm wide and 3 layers thick). The channel was designed as a straight path from the gas inlet to the injection hole in the center of the thruster. The new design for the thruster fluid delivery system can be seen in Figure 63.

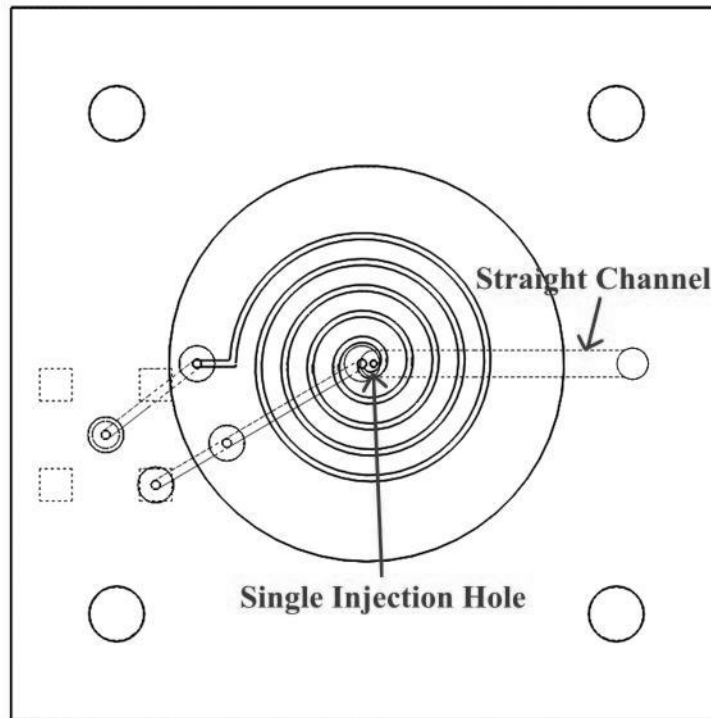


**Figure 63: Center Hole Single Injection Point Thruster Body Design**

With this center hole single injection point design completed and fabricated, the pressure-testing experiments in the vacuum chamber were able to begin.

## 6-4 Experimental Test Setup and Process

### 6-4.1 Equipment Needed For Testing

Before any experiments were started, the proper equipment and supplies were needed. When working with the vacuum chamber, gloves, a lab coat, isopropyl alcohol,

and lint-free wipes were needed. The gloves were used when touching anything that went into the vacuum chamber. This kept the oils from fingers and hands from getting into the chamber and out-gassing, which can keep the chamber from pumping down into the high vacuum range ( $10^{-3}$  to  $10^{-9}$  Torr). The lab coat was used when reaching into the vacuum chamber to prevent oils and hairs from being deposited in the chamber.

Isopropyl alcohol was used with lint-free wipes to clean oil and other debris off anything being placed in the chamber. Experimental equipment required for testing included the various thrusters and the pressure-testing device.

#### 6-4.2 Experimental Testing Process

The experimental process was run and documented with the *LabVIEW* software. This software recorded two pressure gauge values, an associated time stamp, and the flow rate value. Two pressure gauges readings were needed to demonstrate a differential pressure from the experimental data: one convectron gauge connected to the pressure-testing device and another gauge (convectron or ionization) recording pressure at the chamber wall. To begin testing, the low range (4 sccm maximum) flow controller was used. The flow was initiated at 1 sccm. The gas flow was maintained at this flow rate until the pressure readings on the gauges converged on a steady value. After the gauge pressure convergence, the pressures were recorded and the flow was increased an additional 1 sccm. Pressure readings were also obtained and recorded within *LabVIEW* for flow rates of 3, 4, 5, 6, 7, 8, 9, 10, 20, 30, 40, 50, 100, 200, 300, 400, and 500 sccm. For the step in between flow rate values of 4 sccm and 5 sccm, the control of the flow was changed from the small range VI control to the large range VI control that handled the two other MFCs with flows above 4 sccm. The pressure readings converged more



quickly as the flow rates increased. As soon as the final flow rate of 500 sccm had converged pressure readings, the flow was disabled and the gas valves in the system were all closed. The ion gauge was then turned off before shutting the cryogenic pump's gate valve.

At this point, the chamber could either be vented with air to perform another test or it could be left pumped down at the current pressure until it was needed again. To perform an additional test, the chamber is vented with air to change the pressure device tap location or replace the thruster body in the chamber. By the end of the pressure-testing cycle, six tests were completed. These tests consisted of one test at each spacer location (0, 1, or 2 spacers below the tap location) for each of the thruster designs. The results of these tests are analyzed in the following section.

### **6-5 Experimental Results**

Prior to collecting pressure test data for the thrusters, a test was run to determine the accuracy of the pressure gauges with respect to each other. With a convectron gauge being the only option for the pressure tap reading, the other reading for the background chamber pressure could come from either the other convectron gauge or the ionization gauge. The data for the convectron gauges were calibrated for nitrogen and were adjusted to the argon used for propellant. The ionization gauge was already calibrated for argon. To convert the convectron gauge pressure data to argon, a conversion curve was used [55]. This curve is shown in Figure 64 with the gauge reading value on the x-axis and the true argon pressure on the y-axis. The data points for this curve were input into *MATLAB*, and an interpolation was performed within the program. The program code required input of the number of values to interpolate as well as convectron gauge

readings in mTorr and produced output values of argon pressure. The program code for the automatic argon interpolation can be seen in Appendix B.

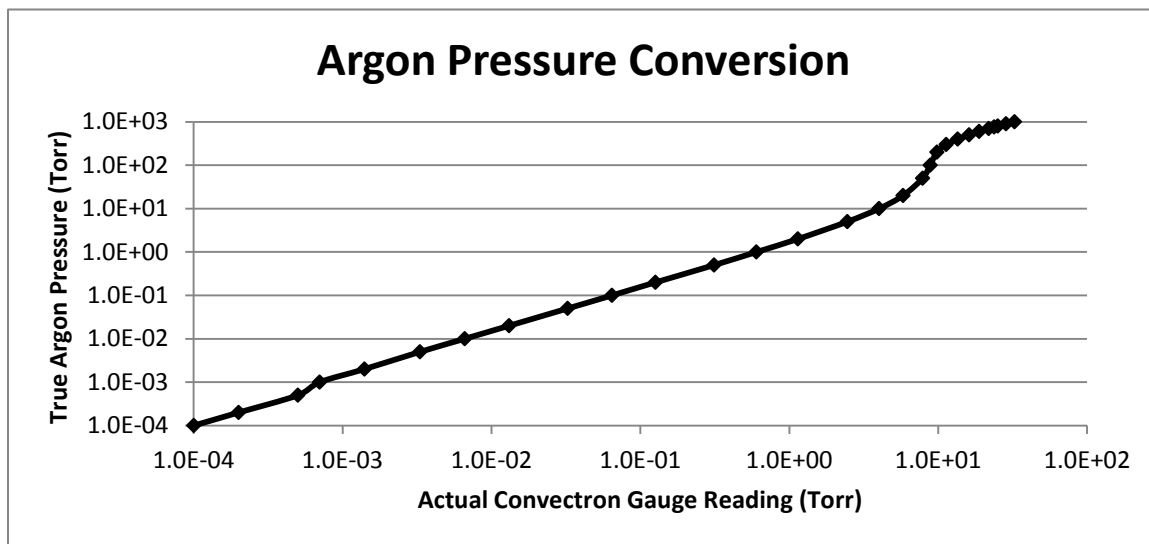


**Figure 64: Convectron Gauge Conversion Curve for Argon Gas**

The initial test showed that the convectron gauge and the ionization gauge were reading within allowable accuracy of each other for most of the flow range. The accuracy drops in the lower flow range (<20 sccm) because the convectron gauge is below its minimum accuracy value of 1 mTorr. As this flow range is the desired range for the thruster operation, the ionization gauge will be used for the chamber background pressure values as it is considered more accurate in this pressure range.

There are a total of six pressure tests that will be discussed in this section. The tests include three measured locations above the antenna in the thruster cylinder for two separate thruster designs. The height from the antenna for the spacer configurations 0, 1, and 2 are 1.24 mm, 4.42 mm, and 7.59 mm, respectively. The two thrusters will be compared by their experimentally measured pressure readings at these locations relative

to the vacuum chamber pressure reading. The resulting delta pressure (thruster pressure minus vacuum chamber background pressure) will be displayed as the pressure values in this section. The effectiveness of each thruster will be judged by the pressures seen in desired flow rate ranges. The results of the thruster testing for the four hole design at all three spacer heights can be seen in Figure 65.

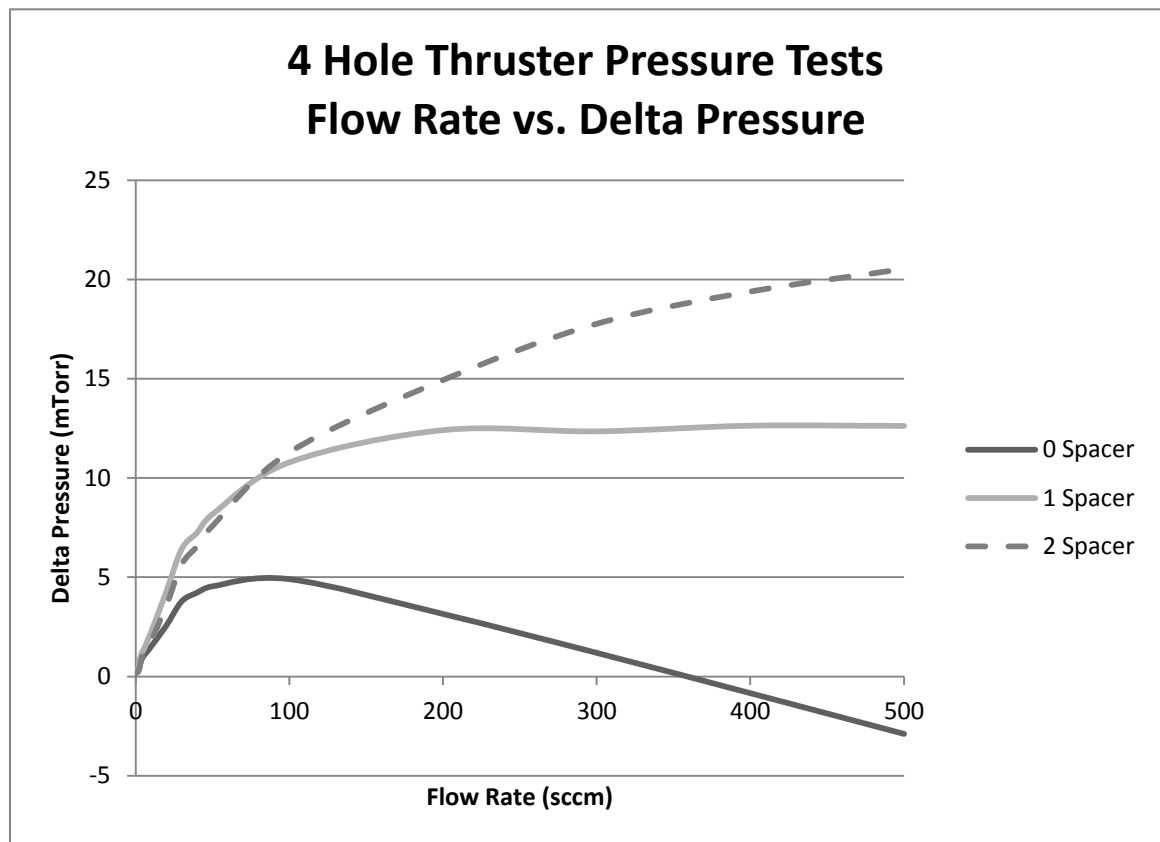


**Figure 65: Pressure Tests for 4 Hole Thruster at Various Spacer Heights**

This figure shows how the pressure inside the device increases as the flow rate is increased. The delta pressure also rises with spacer location as the flow rate increases. There is a small section of the flow range that the 1 spacer tap measures a higher pressure than the 2 spacer tap. This is most likely due to diffusive effects of the gas seen with the

lower flow rates. The 0 spacer pressure tap location sees a constant drop in pressure after approximately 100 sccm as the flow rate increases and above 350 sccm produces a negative delta pressure. This effect is demonstrating that the gas flow is succumbing to momentum effects out towards the end of the thruster before it can diffuse towards the pressure tap on the wall, which is what would be expected for a pressure tap location at the antenna level. Another way of describing this trend is that the momentum effects of the gas are stronger than the diffusive effects at the high flow rates. This effect causes a negative pressure delta because the gas is flowing directly out in to the vacuum before the tap can experience a pressure change; therefore, the background pressure is actually larger than the pressure at the tap location. The single hole and channel test thruster data results are plotted in Figure 66.

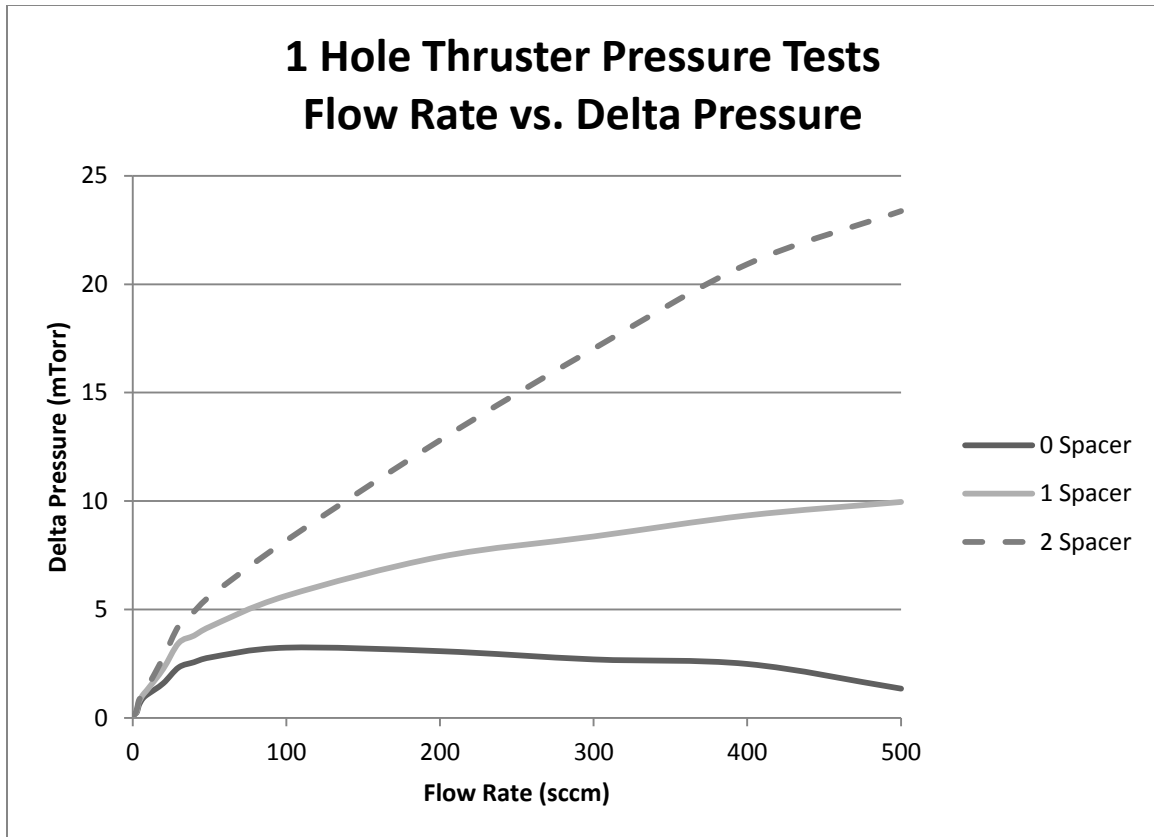


**Figure 66: Pressure Tests for 1 Hole Thruster at Various Spacer Heights**

The results of these tests follow the same patterns at the tests for the 4 hole thruster. The increase of flow rate or pressure tap height tends to increase the pressure seen by the pressure tap. The 0 spacer location also sees the decrease in pressure at the larger flow rate values. The delta pressure however does not reach a negative value in this flow range. Seeing both of these plots for the two thrusters separately is beneficial when comparing the spacer locations for each thruster. All six of these results plotted on a single graph will better demonstrate the effectiveness of which thruster is better. The comparison of the thruster pressures developed at each height between the two thruster configurations can be seen in Figure 67.

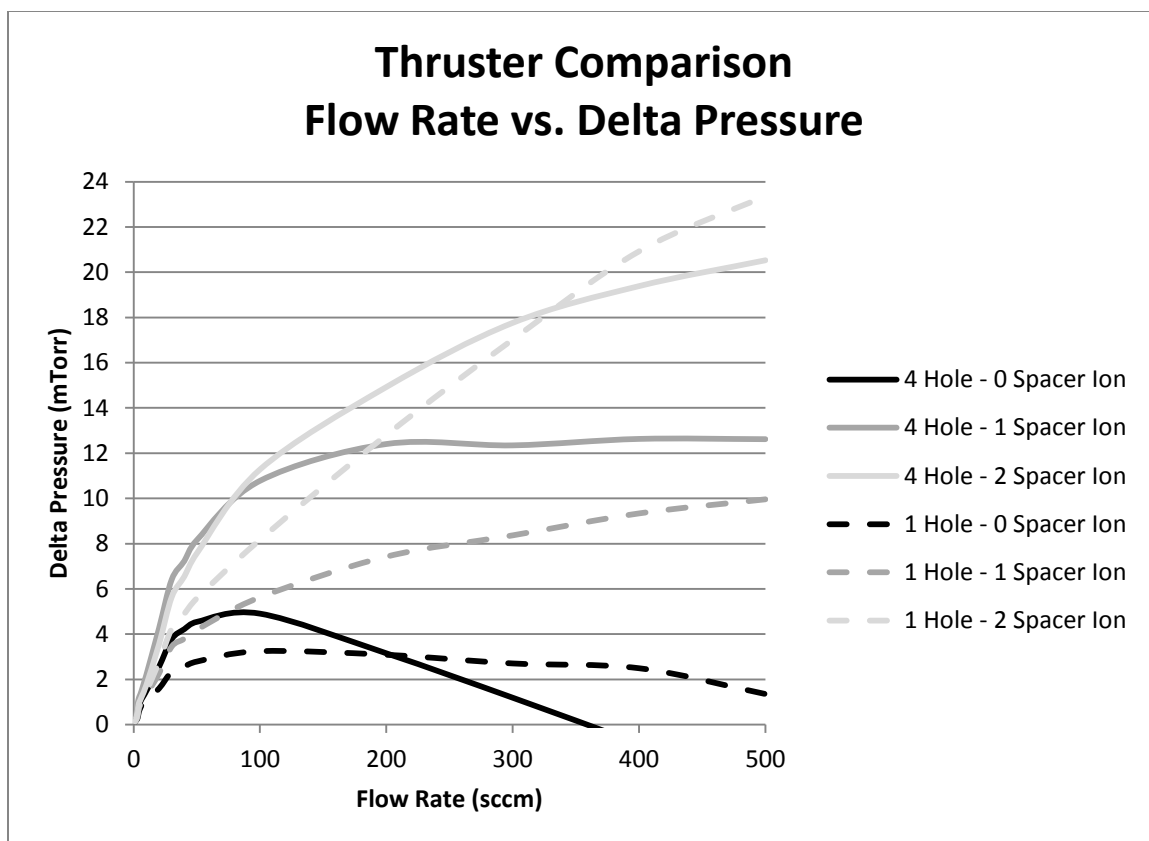


**Figure 67: Thruster Comparison of Localized Pressures at Various Spacer Heights**

The solid lines represent the 4 hole thruster configuration, while the dashed lines represent data values that represent the 1 hole thruster. Similar shades of gray are used between the two thrusters for pressure data sets that correspond to the same spacer height. This figure shows the 4 hole thruster developed a larger delta pressure for a majority of the flow range. The 0 spacer location between the two thrusters shows an interesting difference where the 4 hole thruster drops into a negative pressure and the 1 hole does not. This can be attributed to the Bernoulli Principle, which states that a fast moving fluid creates a low pressure region [56]. The 4 hole thruster has a location of fast moving perpendicular flow closer to the wall than the 1 hole thruster. The faster moving flow creates a region of low pressure near where the pressure tap is measuring pressure, which

in turn lowers the pressure in the pressure tap region. The 1 hole thruster still creates a drop in pressure but does not drop as low because the region of low pressure is farther away from the pressure tap location with this center hole configuration.

Another interesting thing to note about this plot is that the 1 hole antenna actually produced larger pressures at the high end of the flow range. While this means the single hole antenna performs fairly well at the end of the flow range, this part of the flow range will most likely not be necessary for thruster operations. The tests ranged up to 500 sccm flow to demonstrate how the pressure was affected at the high range of system capable flow. Looking at this plot, a maximum of 200 sccm would be assigned for the range with the 4 hole thruster. This is due to the fact that the 0 spacer location pressure value drops below the 1 hole value, and the 1 spacer location pressure appears to reach a plateau delta pressure.

The flow in the low range was hard to visualize on the last plot; consequently, a plot was created to display these results for the low flow range of 0 to 10. This low flow rate range plot can be seen in Figure 68. It should be noted that there are two separate flow controllers in this plot's flow range and the transition between the two can clearly be seen with the hump present between 3 and 4 sccm in all of the pressure curves. The first four flow measurements (1-4 sccm) are operated by the low range controller, while the values 5 through 10 on this plot relate to the second flow controller.

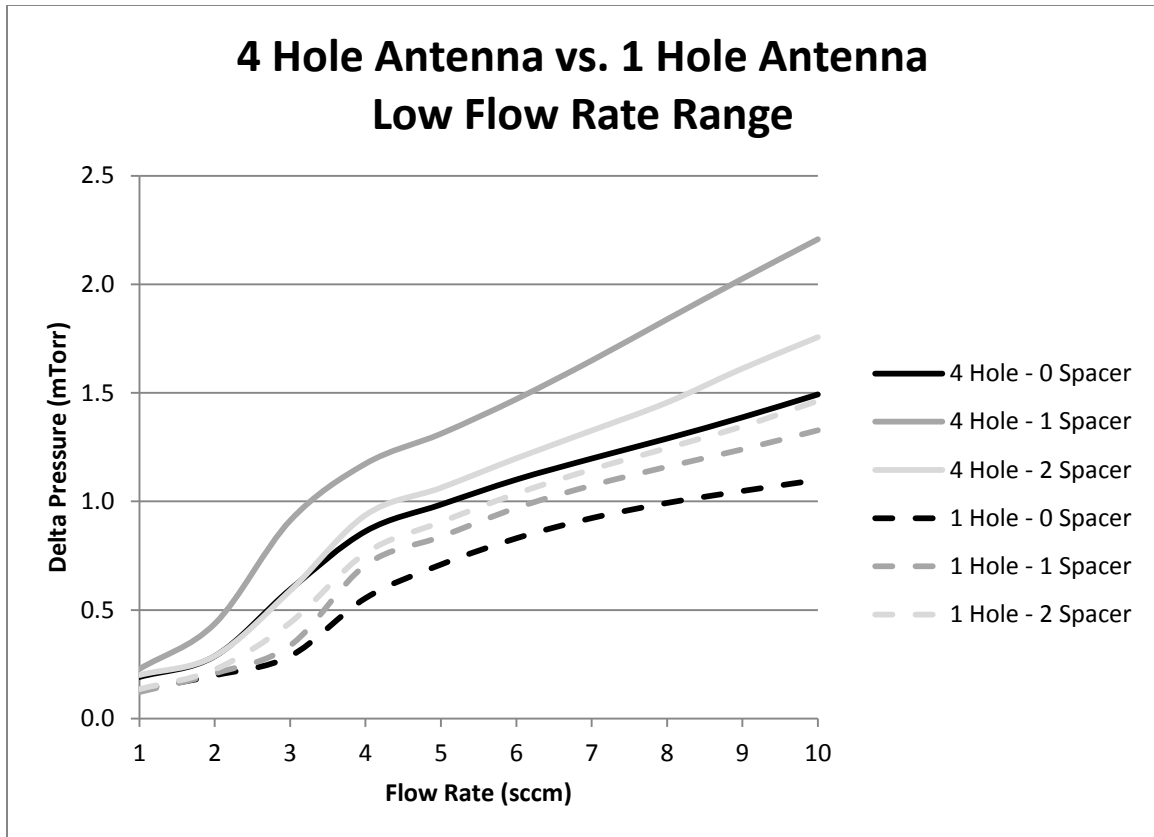


**Figure 68: Low Flow Range (0-10 sccm) Thruster Pressure Test Comparison at Various Heights**

This plot shows a few interesting characteristics of the setup. The low flow range actually creates the highest local pressure in the 1 spacer region for the 4 hole thruster. Even in this low flow range, it can be seen that the 4 hole antenna produces a larger delta pressure at all spacer locations than the 1 hole thruster.

Another explanation for the variance in the flow from the low flow controller to the second controller is the calibration settings for these two controllers. The low flow controller has standard conditions as 273K and atmospheric pressure, whereas the second controller has 274K and atmospheric pressure for standard conditions. This creates a variation in density of  $1.78 \text{ kg/m}^3$  for the low range controller to  $1.66 \text{ kg/m}^3$  for the



second controller. This change in density creates a difference of approximately 8% between the two controller outputs to the system for similar flow rates. This explains the large ramp in flow prior to the transition between MFCs as the first controller has a slightly higher mass flow rate in kilograms per second.

Overall, the 4 hole thruster has proven experimentally to be the better design for creating a higher localized pressure inside the thruster cylinder for all three spacer locations as can be seen by Table 10.

**Table 10: Thruster Configuration Experimental Delta Pressure Mean Percent Increase Over Full Flow Range**

<i>Location of Measurement</i>	<b>4 Hole Thruster Mean Percent Pressure Increase</b>
Spacer 0	13.0%
Spacer 1	74.3%
Spacer 2	21.4%

The data in this table was calculated by finding the percent difference of the four hole thruster delta pressure ( $\Delta p$ ) to the single hole thruster delta pressure at each recorded flow rate, seen as Equation 18.

$$\text{Percent Difference} = \frac{4\text{hole}\Delta p - 1\text{hole}\Delta p}{\left(\frac{4\text{hole}\Delta p + 1\text{hole}\Delta p}{2}\right)} (100\%) \quad (18)$$

Once the delta pressure percent difference of each flow rate was calculated, the mean percent difference of all the flow rates (1-500) at each spacer location was calculated. The four hole thruster produces the listed percent higher pressure relative to

the spacer location for the full range of flow. This higher pressure provides a better environment for initiating plasma with equal electric fields. With this experimental data analyzed and values readily available for the CFD model, the CFD model inputs were entered and simulations ran.

### 6-6 CFD Model Results

For an initial run of the CFD model, an arbitrary argon flow rate of 100 sccm was chosen. This simulation was then compared to the 100 sccm experimental data. The data was compared at the various spacer locations of the pressure-testing device. The results of the *Fluent* CFD model at 100 sccm flow rate can be seen for all three pressure-testing device spacer locations in Figure 69. The pressures used for comparison were the averaged static pressure values at wall locations near the high-pressure regions minus the background pressure. These pressure values simulated the pressure seen at the wall tap in the pressure-testing device (wall taps measure static pressure). The delta pressure values were used in order to neglect the background pressure's influence on the data readings inside the thruster cylinder in a way to better simulate a space environment. The delta pressure was also used to replicate the experimental setup for the CFD model.

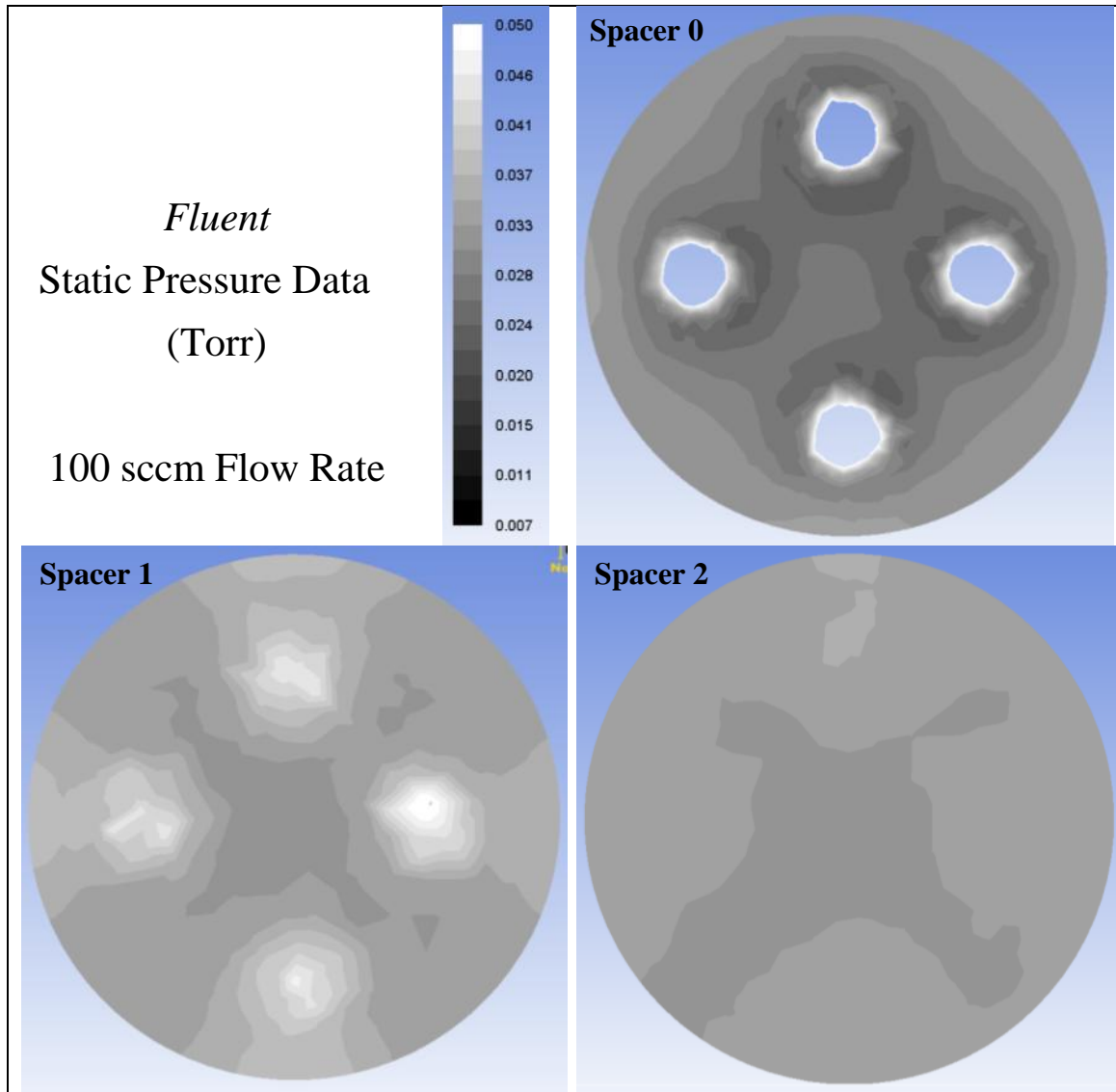


**Figure 69: *Fluent* Static Pressure Readings in Torr at the Corresponding Heights for the Pressure-Testing Device’s Spacer Locations**

The three plots have a pressure range from 7 mTorr to 50 mTorr. The “Spacer 0” plot has pressure values as high as 160 mTorr at the gas injection holes, but they do not show up on the plot due to the pressure range displayed. As can be seen in the figure, the pressure near the wall is actually highest in the “Spacer 1” configuration. The results of the *Fluent* simulation were then compared to the results from experimental testing with

the pressure-testing device. These results are both shown in Table 11. The delta pressure for *Fluent* was calculated by taking the average wall pressure and subtracting the outlet boundary condition pressure corresponding to 100 sccm argon flow assigned at the beginning of the simulation creation.

**Table 11: Experimental and *Fluent* Delta Pressures for 100 sccm Argon Flow**

	Delta Pressure Experimental (mTorr)	Delta Pressure <i>Fluent</i> (mTorr)	% Error
Spacer 0	4.9	26.7	445%
Spacer 1	10.8	31.7	194%
Spacer 2	11.3	27.8	146%

The values seen in the experimental data were much lower than what was simulated in the CFD model. The percent errors for these spacer locations are 445%, 194%, and 146%, respectively. These high percent error values indicate the fluid model is not within the desired range of accuracy for this simulation. An additional flow rate at the lower end of the flow range was considered as well to verify if the lower portion of the range was more accurate. Results from this comparison can be seen in Table 12.

**Table 12: Experimental and *Fluent* Delta Pressures for 10 sccm Argon Flow**

	Delta Pressure Experimental (mTorr)	Delta Pressure <i>Fluent</i> (mTorr)	% Error
Spacer 0	1.5	14.7	880%
Spacer 1	2.2	14.2	545%
Spacer 2	1.8	12.8	611%

The values seen in this delta pressure data comparison indicate the same trend as the previous 100 sccm comparison. The experimental results were much lower than the simulated results. The percent errors for this data came out to be 880%, 545%, and 611%, respectively. These error percentages are much larger than the previous 100

scm comparison. Three other simulations were attempted at flow rates of 1 scm, 200 scm, and 500 scm to check other portions of the experimental testing range. These simulations had errors during the runs and were not successfully completed. The CFD model settings were then evaluated to check for errors.

Upon further inspection of the settings in the simulation, it was found in the *ANSYS 12.0 Theory Guide* for the software that *Fluent* uses a different value for Knudsen number than the value stated in Chapter 4 to distinguish molecular flow. According to the guide, in order for continuum theory to be valid in the CFD model, the Knudsen number should be less than 0.01 [57]. This is quite a large difference from the more traditional value of 10 used in the original calculations. As this value is directly from the software help section, it was used to calculate values for the gas injection channels to be in continuum as well as the gas containment cylinder.

The recalculated value for the required flow rate into the system to maintain continuum flow was found to be 132.8 scm. This number is three orders of magnitude larger than the previous calculation for this location of the flow. For the containment cylinder to be in continuum, a calculated value of larger than 220 mTorr was calculated. This is a large pressure relative to the pressures observed in the experimental pressure-testing device. The largest pressure seen by the device at 500 scm of argon flow was 23.4 mTorr, relative to the background pressure. The analytically calculated value for continuum within the thruster containment cylinder was 1900 scm. This is well above the range of our experimental setup and, therefore, cannot be compared to testing results to validate the CFD model. A CFD model is needed that can successfully be validated in the operational flow range of the thruster.

Although the CFD model was not validated for pressure values, it can at least be seen in the previous figure, Figure 69, that the pressure in the vicinity of the gas injection holes was considerably larger than the remainder of the cylinder. These higher pressure regions could be seen through the second spacer location at a height of 4.42 mm.

Although the values could change considerably with a rarefied flow, it is assumed the same trend would apply as the gas leaving the injection holes would have to diffuse from a much higher pressure to the vacuum pressure. The conclusions drawn from the experimental results as well as the CFD model results will be presented in a final form in the Chapter 7.

## CHAPTER 7: SUMMARY AND CONCLUSIONS

### 7-1 Four Hole Thruster Design

This research into the development of a new thruster gas injection hole configuration proved successful through experimental testing. The new four hole injection design displayed a larger localized pressure inside the thruster containment cylinder for all three spacer locations. This larger pressure will assist with ionization efficiency in two ways. First, the larger pressure increases the probability of initially generating plasma, reducing wasted neutral gas. Second, the larger pressure will help support continued ionization by increasing the number of neutral gas molecules available to create plasma. The distributed gas pattern will also help make use of a larger area of the RF electric field, which will increase the area of ionization within the cylinder.

This goal of increased ionization should be tested for verification that the larger pressures and distributed pattern do in fact help by doing experiments involving plasma testing. The thruster should be checked for the minimum gas flow rate to both start and sustain the plasma. The thruster should also be checked for minimum power requirements to the antenna in order to initiate plasma. These items are all considered future work to be done with these thrusters and would give a great overall view of the thruster for a complete mechanical and electrical design.

## 7-2 CFD Modeling

The CFD modeling portion of the work in this thesis provided some valuable insight on how the *ANSYS Fluent* software works as well as the different views of Knudsen correlation values for both molecular and continuum flow. While some literature states a Knudsen value of greater than 0.01 for molecular flow, other literature suggests larger values of 0.1 and 10. There is a “slip” region according to *ANSYS* that occurs above 0.01 and below 0.1 that can be modeled in *ANSYS* with a variation of the slip parameter in the boundary conditions. This value is still considered low for the application of modeling these thrusters and isn't feasible for the flow range desired for thruster operational use of 0-20 sccm.

As *Fluent* is a CFD modeling software that uses Navier-Stokes equations and relationships (continuum assumption), Direct Simulation Monte Carlo (DSMC) methods can use kinetic theory to solve rarefied fluid flow problems [58]. The DSMC method can be computationally expensive and should only be used in these rarefied flow conditions, as it computes properties of individual molecules rather than a fluid as a whole. The DSMC method can be utilized for the small flow range in consideration for these experiments, but a combined approach with the Navier-Stokes equations could prove useful for calculating the flow as two computational domains as done by Vashchenkov et al. [59]. For larger flow rates, this approach would separate the gas manifold channels as a continuum flow and the flow inside the thruster cylinder as a molecular flow. Using the results from the continuum model, the boundary conditions could be set for the molecular model at the exit plane of the gas channels. This approach would reduce the amount of



computational resources required for the DSMC method and speed up the simulation process dramatically.

### 7-3 Future Fabrication Concerns

Eventually, a better way of connecting the SMA connector and gas fitting should be employed. Brazing metal to the LTCC structure has been attempted, but no successful devices have been completed. The end result of this thruster design will include an integrated grid system held inside the end of the thrust cylinder as seen in the concept drawing in Figure 70.

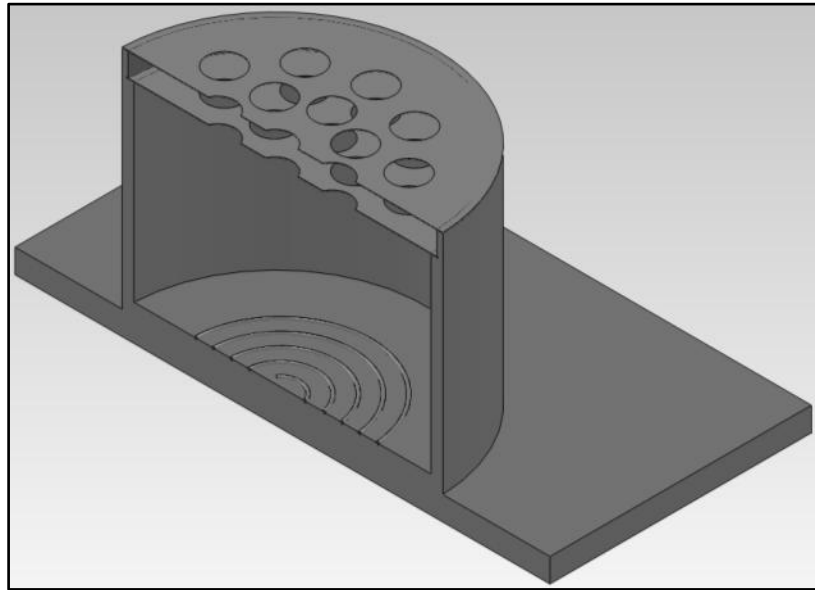


**Figure 70: Concept Drawing of Integrated Grids in the Thruster Cylinder**

The thruster in this thesis currently has a pair of grids held together with an LTCC clamping structure that attaches to the top of the thruster with nylon all-thread and bolts. A picture of the grids attached to the thruster as well as the yoke adapter plate and can be seen in Figure 71. (The design process for the adapter plate can be seen in Appendix C.) The main picture in the figure shows the grids and the LTCC grid clamps. In the bottom-

right of the figure, there is an inset picture that shows the same assembly from a side view to highlight the thruster body as well as how the whole assembly is held together with the nylon all-thread.

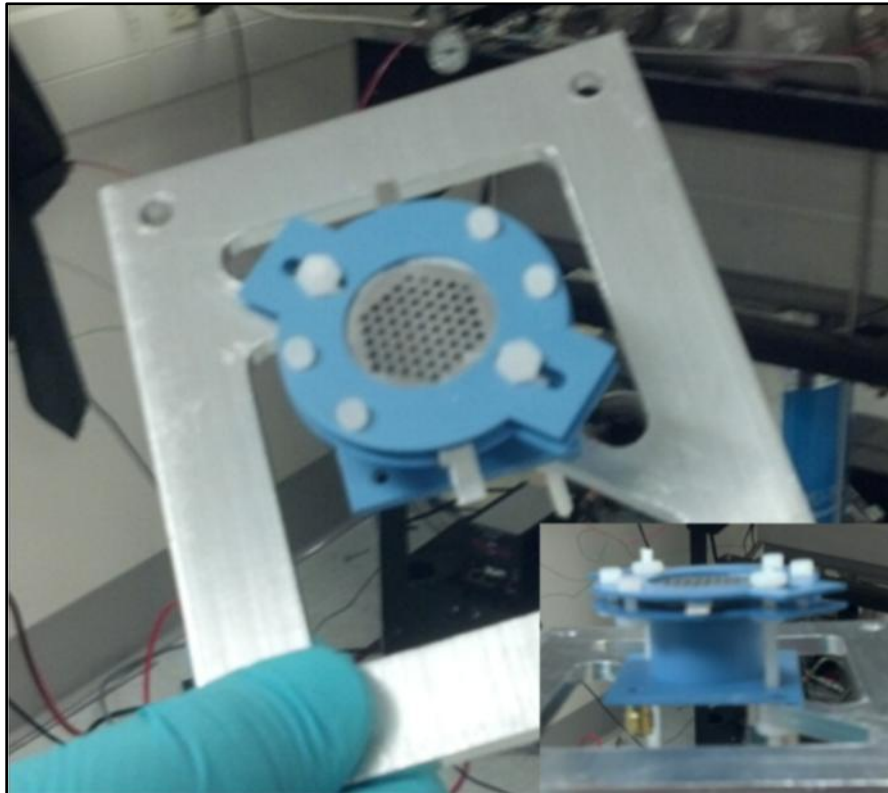


**Figure 71: LTCC Thruster and Grids**

#### **7-4 Successful Plasma Generation**

A successful test of plasma generation was performed and demonstrated in Figure 72. The plasma plume can be seen exiting to the left of the figure. The plasma inside the cylinder is able to produce visible light through a portion of the thruster cylinder walls. The electrical grids will be supplied voltages to harness the plume and produce more of a linear look to the plume rather than the rounded appearance in this figure. This optimization of the plume will generate more forward thrust force as the main component of the plume will be directed normal to the grids. This test was used as a functional test

for plasma generation. Further testing as mentioned in Section 7-1 will be done to actively compare the thruster designs for ionization efficiency and ease of plasma generation.

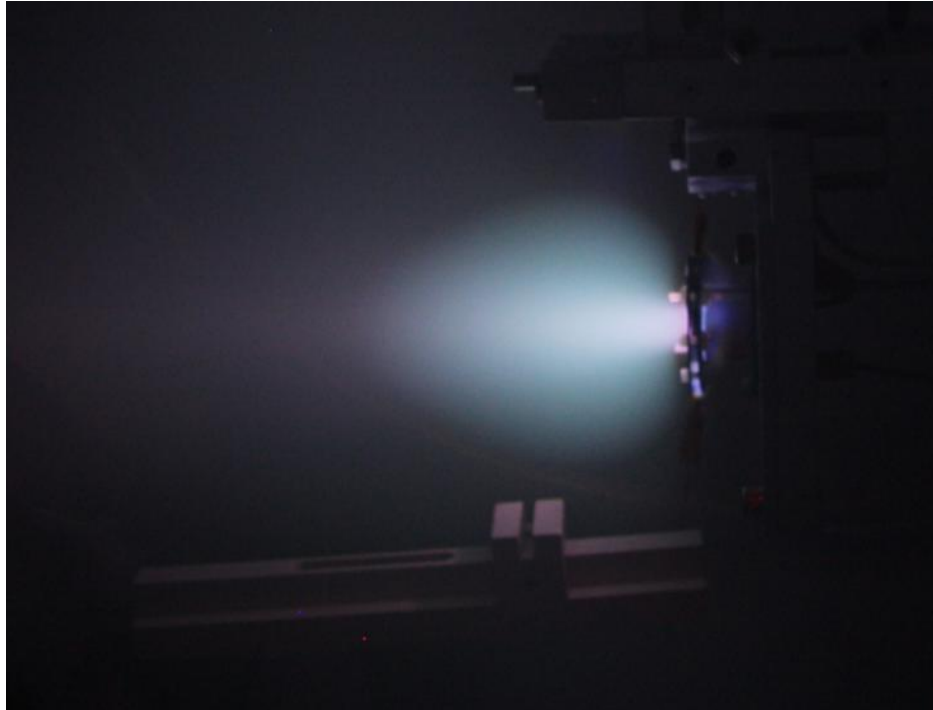


**Figure 72: Successful Plasma Generation Test for 4 Hole Thruster Design**

### **7-5 Conclusions**

There are multiple conclusions to draw from the overall process discussed in this thesis. Conclusions about the design, fabrication process, and CFD modeling are listed below.

#### **Thruster Design**

- Potential shear planes with LTCC designs that require lamination pressure should be avoided.

- A distributed gas injection system increases the pressure inside the containment cylinder compared to a single hole injection.

### **Fabrication**

- PEOX can be used between electrical via interconnects without loss of conductivity.
- PEOX should not be used to attach 951 C2 LTCC, as the LTCC is too thin and easily gets saturated.
- Silver epoxy creates a good electrical connection between the SMA connector and DuPont's silver paste for vias.
- Silver epoxy does not create a strong physical bond between LTCC and the SMA connector.
- Ceramic epoxy creates a good physical bond for connectors to the LTCC.
- Ceramic epoxy can seal small cracks in an LTCC body.
- After applying silver paste to via holes, a lateral slide prior to lifting the LTCC sheet was successful for preserving silver paste in vias.

### **CFD Modeling**

- *ANSYS* cannot be effectively used for modeling the gas behavior outside the gas ports in an electric thruster.
- A combination of DSMC code and *ANSYS* should be used to model electric thrusters.

## REFERENCES

- [1] Small Satellite Home Page. "Satellite Classification." Web. October 2012.  
<[http://www.centaur.sstl.co.uk/SSHP/sshp\\_classify.html](http://www.centaur.sstl.co.uk/SSHP/sshp_classify.html)>
- [2] Larangot, B., et al. "Solid Propellant MicroThruster: An Alternative Propulsion Device for Nanosatellite." Web. October 2012.  
<<http://www.norlandprod.com/Applicationpages/solidpropellantmicrothruster%20mems.pdf>>
- [3] Boyarko, G. A., et al. "Catalyzed Combustion of Hydrogen-Oxygen in Platinum Tubes for Micro-Propulsion Applications." *Proceedings of the Combustion Institute*, Vol. 30, pp. 2481-2488, 2005.
- [4] Yashko, G. J., Hastings, D. E. "Analysis of Thruster Requirements and Capability for Local Satellite Clusters." *American Institute of Aeronautics and Astronautics*. 1996.
- [5] Xupeng, C., et al. "A Homogeneously Catalyzed Micro-Chemical Thruster." *Sensors and Actuators A: Physical*, Vol. 108, pp. 149-154, 2003.
- [6] Zhang, K. L., et al. "Development of a Low-Temperature Co-Fired Ceramic Solid Propellant Microthruster," *Journal of Micromechanics and Microengineering*, vol. 15, pp. 944-952, 2005.

- [7] Lewis, D. H., Jr., et al. "Digital MicroPropulsion." *Proceedings of the International Conference on Micro Electro Mechanical Systems*, January 1999.
- [8] Coxhill, I. G., Gibbon, D. "A Xenon Resistojet Propulsion System for Microsatellites," *Proceedings of 41<sup>st</sup> AIAA/ASME/SAE/ASEE Joint Propulsion Conference & Exhibit, Tucson, AZ, 2005.*
- [9] Xiong, J., et al. "Development of a MEMS Based Colloid Thruster with Sandwich Structure," *Sensors and Actuators A: Physical*, vol. 117, pp. 168–172, 2005.
- [10] Simon, D. H., Land, H. B., "Instrumentation Development for Micro Pulsed Plasma Thruster Experiments," *Proceedings of 41<sup>st</sup> AIAA/ASME/SAE/ASEE Joint Propulsion Conference & Exhibit, Tucson, AZ, 2005.*
- [11] Hofer, R. R. *Development and Characterization of High-Efficiency, High-Specific Impulse Xenon Hall Thrusters*. Dissertation, Ann Arbor: University of Michigan, 2004.
- [12] Goebel, D. M., Katz, I. *Fundamentals of Electric Propulsion: Ion and Hall Thrusters*. Jet Propulsion Laboratory & California Institute of Technology, 2008.
- [13] Slough, J., Ewing, J. J. "Microarcjet Microthruster for Nanosat Applications." *Proceedings of the 43<sup>rd</sup> AIAA/ASME/SAE/ASEE Joint Propulsion Conference, Cincinnati, OH. July 8-11, 2007.*
- [14] Miyoshi, M., et al. "Microwave Discharge Ion Thruster using Argon as a Propellant." *Proceedings of the 30<sup>th</sup> International Electric Propulsion Conference, Florence, Italy, September 2007.*
- [15] Rüdener, F., et al. "Indium Field Emission Microthrusters." *Proceedings of the Second European Spacecraft Propulsion Conference, Noordwijk, Netherlands. May 27-29, 2007.*

- [16] Choueiri, E. Y., Ziemer, J. K., “Quasi-Steady Magnetoplasma-dynamic Thruster Performance Database.” *Journal of Propulsion and Power*. Vol. 17, No. 4, September/October 2001.
- [17] Eastman, T. E. “Perspectives on Plasmas – the fourth state of matter.” Web. October 2012. <<http://www.plasmas.org/basics.htm>>
- [18] Lestrade, R. “Interior of Plasma Ball with Slightly Slow Shutter Speed.” Feb. 19, 2008. Web. July, 2012. <<http://www.en.wikipedia.org/wiki/File:Plasmabaw.jpg>>
- [19] Samsung. “Samsung Plasma TVs.” Web. October 2012. <<http://www.samsung.com/us/video/plasma-tv>>
- [20] Victor Technologies. “Thermal Dynamics.” Web. October 2012. <<http://www.victortechnologies.com/thermaldynamics>>
- [21] N.A.S.A. “Ion Propulsion: Farther, Faster, Cheaper.” Web. October 2012. <[http://www.nasa.gov/centers/glenn/technology/Ion\\_Propulsion1.html](http://www.nasa.gov/centers/glenn/technology/Ion_Propulsion1.html)>
- [22] Tipler, P. A., Mosca, G. *Physics for Scientists and Engineers*. 5<sup>th</sup> Edition. W. H. Freeman and Company, 2004.
- [23] U.C. Davis ChemWiki. “Group 18: The Noble Gases.” Web. October 2012. <[http://chemwiki.ucdavis.edu/Inorganic\\_Chemistry/Descriptive\\_Chemistry/Main\\_Group\\_Elements/Group\\_18%3A\\_The\\_Noble\\_Gases](http://chemwiki.ucdavis.edu/Inorganic_Chemistry/Descriptive_Chemistry/Main_Group_Elements/Group_18%3A_The_Noble_Gases)>
- [24] Xiong, J., et al. “A Colloid Micro-Thruster System.” *Microelectronic Engineering*, Vol. 61-62, pp. 1031-1037, July 2002.
- [25] Ye, X.Y., et al. “Study of a Vaporizing Water Micro-Thruster.” *Sensors and Actuators A: Physical*, Vol. 89, Issue 1-2, pp. 159-165, March 20, 2001.

- [26] Madou, Marc J. *Fundamentals of Microfabrication: The Science of Miniaturization, 2<sup>nd</sup> Edition*. CRC Press, 2002.
- [27] Plumlee, D. G. *Fabrication of a Miniature Ion Mobility Spectrometer in Low Temperature Co-Fired Ceramic*. Thesis, Boise: Boise State University, 2003.
- [28] DuPont Microcircuit Materials. "Cost Effective Solutions for High Density Interconnect and RF Modules Using Low Temperature Cofired Ceramic Materials," July 27, 2001. Web. September 2012.  
<[http://www2.dupont.com/MCM/en\\_US/PDF/techpapers/A053\\_Paper\\_for\\_IEM-IEMT-2000.pdf](http://www2.dupont.com/MCM/en_US/PDF/techpapers/A053_Paper_for_IEM-IEMT-2000.pdf)>
- [29] Malecha, K. "Integration of Optoelectronic Components with LTCC (Low Temperature Co-Fired Ceramic) Microfluidic Structure." *Metrology & Measurement Systems*, Vol. XVIII (2011), No. 4, pp. 713–722.
- [30] Peterson, K. A., et al. "Novel Microsystem Applications with New Techniques in Low-Temperature Co-Fired Ceramics." *International Journal of Applied Ceramic Technology*, Vol. 2, No. 5, pp. 345-363. 2005.
- [31] Baker, A., Randall, C. "Fabrication of a Multilayered Low-Temperature Cofired Ceramic Micro-Plasma-Generating Device." *International Journal of Applied Ceramic Technology*, Vol. 3, No. 6, pp. 413-418. 2006.
- [32] Shawver, S. M. *Modeling and Measuring the Characteristics of an Inductively Coupled Plasma Antenna for a Micro-Propulsion System*. Thesis, Boise: Boise State University, 2012.



- [33] Browning, J., et al. "A Miniature Inductively Coupled Plasma Source for Ion Thrusters." *IEEE Transactions on Plasma Science*, Vol. 39, No. 11, November 2011.
- [34] Iza, F. and Hopwood, J., "Influence of operating frequency and coupling coefficient on the efficiency of microfabricated inductively coupled plasma sources," *Plasma Sources Science and Technology*, Vol. 11, pp. 229-235, 2002.
- [35] Holt, G., et al. "Relative Navigation, Microdischarge Plasma Thruster, and Distributed Communications Experiments on the FASTRAC Mission." *Proceedings of the 17<sup>th</sup> Annual AIAA/USU Conference on Small Satellites, Logan, Utah*, August 2003.
- [36] Smirnov, A., et al. "Parametric Investigations of Miniaturized Cylindrical and Annular Hall Thrusters." Web. October 2012.  
<[http://erps.spacegrant.org/uploads/images/images/iepc\\_articledownload\\_1988-2007/2001index/38\\_4.pdf](http://erps.spacegrant.org/uploads/images/images/iepc_articledownload_1988-2007/2001index/38_4.pdf)>
- [37] Surrey Satellite Technology Ltd. "Microsatellite Gas Propulsion System." Web. October 2012. < <http://www.sstl.co.uk/Downloads/Datasheets/Subsys-datasheets/Gas-Propulsion-System-ST0065932-v004-00>>
- [38] DuPont Microcircuit Materials. "951 Green Tape<sup>TM</sup>." Sept. 3, 2003. Web. August 2010.  
<[http://www2.dupont.com/MCM/en\\_US/assets/downloads/prodinfo/951LTCCGreenTape.pdf](http://www2.dupont.com/MCM/en_US/assets/downloads/prodinfo/951LTCCGreenTape.pdf)>

- [39] McCrink, M. H. *Design and Analysis of a Low Temperature Co-Fired Ceramic Micro Combustor*. Thesis, Boise: Boise State University, 2010.
- [40] Plumlee, D. G. *Development of a monopropellant micro-propulsion device in low temperature co-fired ceramics*. Dissertation, Moscow: University of Idaho, 2007.
- [41] Dupont Microcircuit Materials. "DuPont Green Tape™ Material System Design and Layout Guides," May 2005. Web. September 2012.  
<[http://www2.dupont.com/MCM/en\\_US/assets/downloads/prodinfo/LTCC\\_DesignGuide.pdf](http://www2.dupont.com/MCM/en_US/assets/downloads/prodinfo/LTCC_DesignGuide.pdf)>
- [42] Parrish, Kelci, et al. "Characterization of the Fabrication Process of Rolled LTCC Structures." *Proceedings of the 8<sup>th</sup> International IMAPS/ACerS Conference, Erfurt, Germany, April 2012*.
- [43] Shaw, R. "The influence of hole dimensions on static pressure measurements." *Journal of Fluid Mechanics*, 7, pp. 550-564. 1960.
- [44] Çengel, Y. A., and Boles, M. A. *Thermodynamics: An Engineering Approach*. 6<sup>th</sup> Edition. McGraw Hill, 2008.
- [45] Janna, W. S. *Design of Fluid Thermal Systems*. 3<sup>rd</sup> Edition. Cengage Learning, 2010.
- [46] Woldtvedt, J. T. *The Design, Fabrication, and Calibration of a Micro-Newton Thrust Measurement Stand*. Thesis, Boise: Boise State University, 2011.

- [47] Wirz, R., et al. "Development and testing of a 3cm electron bombardment micro-ion thruster". *Proceedings of the 27<sup>th</sup> International Electric Propulsion Conference, Pasadena, California*, October 2001.
- [48] ANSYS. "ANSYS Fluent." Web. March 28, 2013.  
<<http://www.ansys.com/Products/Simulation+Technology/Fluid+Dynamics/Fluid+Dynamics+Products/ANSYS+Fluent>>
- [49] Laurendeau, N. M. *Statistical Thermodynamics: Fundamentals and Applications*. Cambridge University Press, 2005.
- [50] Bondi, A. "Van der Waals Volumes and Radii." *Journal of Physical Chemistry*, Volume 68, No. 3, pp. 441-451. 1964.
- [51] Mathcad. "PTC Mathcad: The Industry Standard for Engineering Calculations." Web. March 28, 2013. <<http://www.ptc.com/product/mathcad/>>
- [52] Anderson, J. D. *Computational Fluid Dynamics: The Basics with Applications*. McGraw-Hill, 1995.
- [53] Swagelok. "An Installer's Pocket Guide for Swagelok® Tube Fittings." Web. September 2011. <<http://www.swagelok.com/downloads/webcatalogs/EN/MS-13-151.PDF>>
- [54] National Instruments. "What is LabVIEW?" Web. October 11, 2012.  
<<http://www.ni.com/labview/whatis/>>
- [55] Kurt J. Lesker Company. "275 series Convection Vacuum Gauge." Web. May 2012.

<[http://www.lesker.com/NewWeb/Gauges/pdf/manuals/KJLC\\_275\\_Series\\_manual\\_v103.pdf](http://www.lesker.com/NewWeb/Gauges/pdf/manuals/KJLC_275_Series_manual_v103.pdf)>

- [56] U.S. Centennial of Flight Commission. "Bernoulli's Principle." Web. October 2012. <<http://www.centennialofflight.gov/essay/Dictionary/bernoulli/DI9.htm>>
- [57] ANSYS. "ANSYS FLUENT 12.0 Theory Guide." Web. October 22, 2012. <<http://www1.ansys.com/customer/content/documentation/121/fluent/flth.pdf>>
- [58] Alexander, F. J., Garcia, A. L. "The Direct Simulation Monte Carlo Method." Web. October 24, 2012. <<http://www.algarcia.org/Pubs/DSMC97.pdf>>
- [59] Vashchenkov, P. V., et al. "DSMC and Navier-Stokes Study of Backflow for Nozzle Plumes Expanding into Vacuum." Web. October 24, 2012. <<http://www.dtic.mil/dtic/tr/fulltext/u2/a445940.pdf>>

APPENDIX A

**A-1 Detailed Experimental Setup and Processes**

### A-1.1 Thruster Experimental Test Setup

A thrust stand was completed last year for the project that will allow the BSU electric propulsion team to measure potential thrust output of the experimental thrusters. This thrust stand can measure very fine thruster measurements from 0 to 100  $\mu\text{N}$ , but will need additional improvements to get better resolution above 100  $\mu\text{N}$ . This thrust stand utilizes a pendulum arm with counterweights to determine thrust and can be seen in Figure 73 [45].

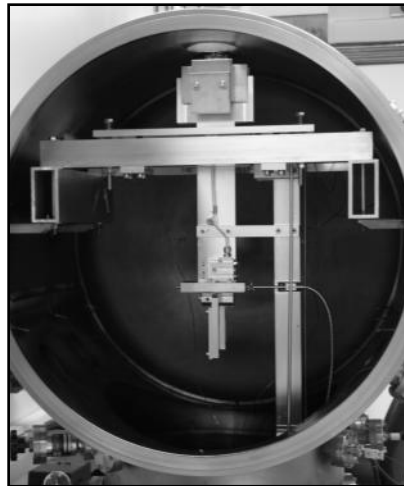


**Figure 73: BSU Electric Propulsion Thrust Stand**

Each thruster designed for the BSU electric propulsion project will be tested in a small vacuum chamber located at Boise State University. This chamber has an approximate volume of 1.5 cubic meters. The vacuum chamber aids in the experimentation by simulating space conditions for thrust generation. This vacuum chamber can be seen in Figure 74.

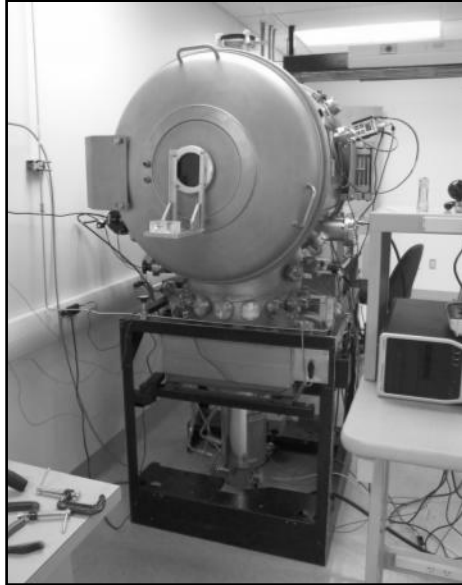


**Figure 74: BSU Electric Propulsion Vacuum Chamber**

The vacuum chamber pressure is controlled by two different pumping systems. The first pump to initiate at atmospheric pressure, 760 Torr, is a two-stage mechanical pump. The top stage of the pump, which is the first to see chamber exhaust, is comprised of a Root's blower that has two figure-eight rotors that rotate rapidly, collecting gas, compressing it, and then sending it to the second stage of the pump. The second stage has a screw drive that collects the gas from the first stage and pushes it out to the exhaust line. Along the chamber exhaust line is a two-stage valve that allows for a larger range of pumping with this single pump. The valve has a small orifice that is initially activated at atmospheric pressure to lower the pressure seen by the Root's pump. Once the pressure in the chamber is dropped to 100 Torr, the second stage of the valve activates, which allows for a faster pumping speed. The bottom end of the pressure range of this mechanical roughing vacuum pump is approximately 1 mTorr. Figure 75 shows the pump located at Boise State University.



**Figure 75: Two-Stage Mechanical Vacuum Pump**

The second pump used with this vacuum system is a cryogenic pump. This pump is constantly running and is located at the base of the vacuum chamber. It allows the vacuum chamber to reach pressures as low as  $1e-6$  to  $1e-8$  Torr. The cryogenic pump works by using compressed gas to cool a surface, which then collects the condensed gases from the vacuum chamber. The pump stores the gases until it is regenerated, which involves bringing the temperature of the pump up to release the trapped gases. This pump is activated by opening a gate valve when the pressure of the vacuum chamber is below 5 mTorr. The cryogenic pump and associated gate valve can both be seen in Figure 76.





**Figure 76: Cryogenic Pump and Gate Valve**

There are three pressure gauges located on the vacuum chamber to assist in operation and experimentation with the chamber. Two Kurt J. Lesker convectron gauges are connected to the chamber with ConFlat (CF) flanges and an InstruTech ionization gauge is connected to the chamber wall between the gate valve and the cryogenic pump. The convectron gauges read pressure with 10 percent accuracy in the pressure range of 1 mTorr to 400 Torr and the ionization gauge reads pressure with 15 percent accuracy in the pressure range of  $10^{-9}$  Torr to 50 mTorr. The full capable range of the convectron gauges is 0.1 mTorr to 1000 Torr.

A convectron gauge is a thermal conductivity gauge and works by using a constant electrical current sent through a filament. The gas molecules that collide with the filament receive thermal energy from the filament and a change in filament

temperature is sensed with a thermocouple welded to the filament. The reading from the thermocouple is then converted to a pressure value at the gauge controller. The convector gauge is unique from other thermal conductivity gauges because it can read higher pressures (up to 1000 Torr). This gauge uses a gold-plated tungsten current filament wire surrounded by an insulating wire wound cylinder. An ionization gauge uses three electrodes to function properly. The first electrode uses low voltage electric current to emit electrons, which collide with gas atoms, creating ions. A second electrode acts as an electron collector, which increases ionization efficiency. The third electrode collects the gas ions created from the electron bombardment. The ions collected generate a current, which is then converted to a pressure by the gauge controller. Both the convector gauge and the ionization gauge are sensitive to different species of gas. Thus, each gauge has to be calibrated for a specific gas or a conversion is needed to manipulate the gauge data.

In order to achieve a consistent flow of gas into the thruster body, mass flow controllers are used to control a regulated upstream pressure coming from the pressurized argon tank. The mass flow controller receives approximately one atmosphere of pressure (760 Torr) from the argon tank. To control the mass flow rate, a user has to send a 0 to 5 volt signal to the controller. The ratio of this signal to the full signal range is then the proportion of the full gas flow range of the valve. For example, a 1 volt signal will create a 20% of full scale flow ( $1V/5V$ ). Since gases have different masses associated with them, the flow controller has to be calibrated to the appropriate gas or a conversion must be applied.

Standard pressure is considered to be 1 atmosphere or 760 Torr and standard temperature can have several values depending on the MFC manufacturer's calibration standards. Common standard temperature values tend to be one of the following values: 273K (0°C), 293K (20°C), 294K (21°C), 298K (25°C), or 300K (27°C). The sccm volumetric flow rate can be converted to a mass flow rate by using the ideal gas law, seen as Equation 19 in conjunction with the volumetric flow rate.

$$P = \rho RT \quad (19)$$

$P$  is the pressure of the gas,  $\rho$  is the density of the gas,  $R$  is the gas constant for the specific gas in question, and  $T$  is the gas temperature. As an example, argon at atmospheric pressure and room temperature (294K), using Equation 19, has a density of 1.66 kg/m<sup>3</sup>. Once the density of the gas at standard conditions is known, it is multiplied by the standard volumetric flow rate,  $Q$  (sccm), from the mass flow controller to calculate the mass flow rate,  $\dot{m}$ , of the gas, as seen in Equation 20.

$$\dot{m} \left( \frac{kg}{s} \right) = \rho \left( \frac{kg}{m^3} \right) \cdot Q (sccm) \cdot \frac{(1m)^3}{(100cm)^3} \quad (20)$$

### A-1.2 Preparation of Vacuum Chamber for Testing Conditions

This section of the thesis details how the experiments were done to ensure repeatability between successive experiments as well as how to properly utilize the vacuum chamber equipment. Whenever beginning an experiment, the vacuum chamber was inspected to see if it was in use or if any pumps were on and actively pumping the

chamber down. If any pumps were running, they were disconnected from the system by closing any associated valves to the vacuum chamber. The roughing pump could be turned off when it was not in use. The cryogenic pump continued to run and was not turned off unless it needed to be regenerated. The gate valve to the cryogenic pump was closed if open. Once ensured that both pumps were not actively connected to the chamber, the chamber could be vented to atmospheric pressure. The chamber was vented slowly to avoid a large pressure differential, which can shift parts inside the chamber.

As the chamber was venting, the pressure device and thruster configuration to be tested were cleaned thoroughly with alcohol. Once the parts were clean, the chamber was opened and the parts were placed carefully in the chamber. The thruster should already be attached to the pressure device when placing it in the chamber. The pressure-testing device was attached with the quarter-inch tubing to the right side of the chamber behind the thrust stand pendulum arm. The location where the connection was made was on the vacuum chamber side of the convectron gauge flange. This convectron gauge was the gauge that recorded the gas pressure inside the pressure-testing device. Once the testing device was connected to the gauge, the gas line could be attached to the base of the thruster body. Caution was used while attaching the gas line because too much torque on the thruster could separate the ceramic epoxy and fitting from the LTCC. The opposite side of the gas line was attached to another gas line near the top of the chamber on the front side of the thrust stand.

As soon as the gas line was hooked up, the chamber could be wiped down and closed. The lint-free wipes and alcohol are used to wipe the metal sealing surface for the O-ring located on the door of the chamber. The chamber door was then closed and two

clamps were used to create an initial seal between the door and the chamber. The final step to seal the vacuum chamber was closing the vent valve.

The next step in the process involved pumping down the chamber. To send and receive signals to the chamber components such as the mass flow controllers, roughing pump, and pressure gauges, the *LabVIEW* project file for the vacuum chamber was opened. Once the project file was opened, the main vacuum chamber control file was opened. In order to get the computer to start sending and receiving information from all the electronic devices, the “Run” button was pressed in the chamber file. For the purpose of the testing in this thesis, the only controls needed from this file were the auto log, auto pump, and mass flow controls. The auto log control allowed the data from the pressure gauges to be written to a text file. The auto pump control automatically controls the two stage valve for the roughing pump depending on what pressure range the chamber is in. The indicators for mass flow rate as well as the pressure gauges were used to determine the stability of the flow into the system. Once *LabVIEW* was up and running, the pumping process was started. Prior to starting the pumping process, the auto log function was used to start recording chamber pressure to a file.

To begin the pumping down of the vacuum chamber, the roughing pump had to be turned on and the valve on the pump opened. Back at the computer, the auto log control was used to start the pumping of the chamber. Once the control was used, a dialogue box opened, which required a target pump-down pressure. A value was entered of zero Torr to make the roughing pump max out its pumping capabilities. This first part of the pumping cycle involved waiting for a short while for the first stage of the roughing pump to take the pressure of the chamber down to 100 Torr. Once the average pressure

between the two convectron gauges reached 100 Torr, the large opening of the two-stage valve connected to the roughing pump line was automatically opened. This process evacuated the gas in the chamber down to a pressure near the  $1 \times 10^{-3}$  Torr pressure range within a few minutes.

When the pressure in the chamber was below 5 mTorr, the gate valve for the cryogenic pump was opened. An operating procedure for properly opening and closing the gate valve can be seen in Appendix D. With the gate valve open, the roughing pump auto pump control was disabled. The roughing pump valve was then closed and the pump turned off because at low pressures below 1 mTorr, the roughing pump actually acts like an air leak into the system, which hinders the cryogenic pump's effectiveness. At this point, the ionization gauge controller could be toggled to turn the ionization gauge on. The gauge was turned on once the pressure in the system was low because the ionization gauge could be damaged if it was exposed to a pressure above 50 mTorr. The chamber continued to pump down for several hours to reach a pressure of  $5 \times 10^{-6}$  Torr. Once this pressure was reached, the ion gauge was toggled off and then the gate valve closed.

The next phase in the process was used to remove air-adsorbed molecule layers on the surface of the chamber. Air molecules in the chamber can contain moisture due to the humidity in the air. These moisture in these molecules is slowly released when the vacuum chamber gets pumped down, which makes the pumping process take longer and is less consistent. The initial pump down to  $5 \times 10^{-6}$  Torr was to remove most of the air out from the chamber. Next, the valves for the gas flow into the system were all opened. This included the argon main valve, the mass flow controller valves, and the three-way

valve (gas calibration setting). The large flow rate control in *LabVIEW* was turned on to the maximum capacity of 500 sccm.

When the pressure in the chamber rose to 1 Torr, the flow was shut off and the chamber sat at 1 Torr of argon pressure for 30 minutes. This period was used to allow for argon gas adsorption to the chamber walls. If a chamber has been exposed to air for any period of time, the air molecules can adsorb to the surface of the chamber, building up multiple layers of adsorbed gas. The air molecule layers needed to be removed and adding the higher pressure of argon for a while can help remove the adsorbed air molecules. After the 30 minutes, the chamber was pumped back down with the roughing pump. The pump needed to be turned back on, the roughing pump valve opened, and the auto pump feature enabled. The chamber quickly pumped back down to a range suitable to open the gate valve. With the gate valve open, the auto pump, roughing valve, and roughing pump were all disabled once again. The ion gauge was then turned back on to record the lower pressures seen by the chamber. When the chamber reached a pressure of  $5 \times 10^{-6}$  Torr, the pressure-testing began.

## APPENDIX B

**B-1 MATLAB Code for Argon Interpolation with Convectron Gauges**



```

clc

clear

format shorte

% Argon Conversion Table Data

y=[1e-4;2e-4;5e-4;1e-3;2e-3;5e-3;1e-2;2e-2;5e-2;1e-1;2e-1;5e-
1;1;2;5;10;20;50;100;200;300;400;500;600;700;760;800;900;1000];

x=[1e-4;2e-4;5e-4;7e-4;1.4e-3;3.3e-3;6.6e-3;1.31e-2;3.24e-
2;6.43e-2;1.26e-1;3.12e-1;6e-
1;1.14;2.45;4;5.8;7.85;8.83;9.79;11.3;13.5;16.1;18.8;21.8;23.7;25.1;28.
5;32.5];

% Set up x range and interpolate using pchip function

xq=(1e-4:1e-6:1e-1);

yq=interp1(x,y,xq,'pchip');

% Plot data points and interpolated line

plot(x,y,'o');

hold on

plot(xq,yq,'-');

% Enter number of values and CG values in milliTorr to
interpolate

```

```
numberofvalues=19;
```

```
mTorrValues=[
```

```
0.258;
```

```
0.430;
```

```
0.619;
```

```
0.772;
```

```
0.883;
```

```
1.011;
```

```
1.137;
```

```
1.259;
```

```
1.376;
```

```
1.491;
```

```
2.524;
```

```
3.956;
```

```
4.801;
```

```
5.125;
```

```
7.291;
```

```
10.022;
```

```
12.351;
```

```
14.369;
```

```
16.179
```

```
];
```

```

%Convert CG values to Torr

values=mTorrValues/1000;

% For loop to find index of values in x array and ouput
associated y values

% Remove Floating Point Errors at the same time

tol=.000000001;

index=zeros(1,numberofvalues);

for i=1:numberofvalues;

    index(i)=find(abs(xq-values(i))<tol);

end

% Display Values in mTorr

format short

yq(index)*1000

```

### B-2 MATLAB Code Example Output

ans =

Columns 1 through 8

```

    0.2537    0.4106    0.7942    1.1306    1.3079    1.4864
1.6481    1.8042

```

Columns 9 through 16

	1.9648	2.1364	3.7659	6.0072	7.2856	7.7729
11.0555	15.2490					

Columns 17 through 19

18.8428	21.9617	24.7633
---------	---------	---------

APPENDIX C

**C-1 Additional Designs**

Additional designs for various components in this thesis are discussed in this section. These designs include the thrust stand yoke plate that connects the thruster body to the thrust stand for testing purposes, the variable mass flow range using multiple mass flow controllers discussed earlier in this thesis, as well as the final pressure-testing device used to verify the benefits of the four hole design as well as verify the fluidic model.

### C-1.1 Thrust Stand Adaptor Plate

In order to measure thrust from these thrusters in the future, an intermediate component is needed between the thruster body and the thrust stand. This component is used as a rigid mount for the thruster body. It also functions as an adaptor plate, which takes the larger bolt holes needed by the thrust stand yoke as well as the small nylon all-thread holes from the thruster body. Figure 77 shows a portion of the thrust stand drawing with the yoke and bolt pattern showing.

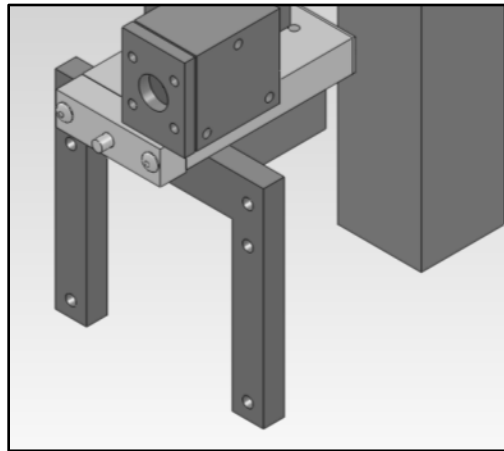


**Figure 77: Thrust Stand Yoke for Thruster Attachment**

The adaptor plate needs to be 101.6 mm tall and 127 mm wide. This plate will have four bolt holes located 9.525 mm from each edge in the corners with a diameter of

6.35 mm. Since the plate will be made from metal (aluminum) for out-gassing purposes, the portion of the plate that will be located behind the thruster body will be milled out except for two small extensions from the side of the plate that will line up with the thruster alignment holes. The ends of these extensions will have a hole sized for the close fit dimension for #4 machine screws (2.95 mm). The extensions will come from a diagonal angle to give more room for components on the opposite diagonal. Figure 78 shows the final design of the adaptor plate needed for the new thruster design.

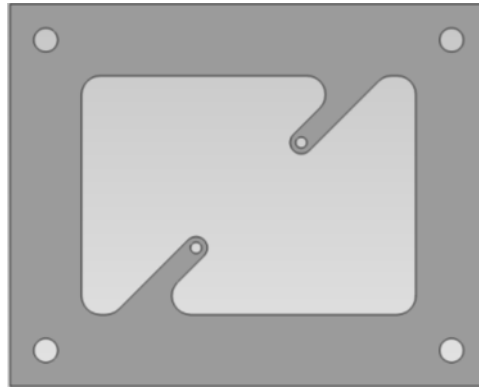


**Figure 78: Thrust Stand Adaptor Plate for New Thruster Design**

APPENDIX D

**D-1 Cryogenic Pump Gate Valve Operating Instructions**



### **Cold Start (The cryopump is running and the gate valve is closed)**

1. Ensure the gate valve is CLOSED.
2. Close the chamber door.
3. Begin pumping down the system with the roughing pump.
4. When the system reaches 5E-03 Torr, open the gate valve.
5. Disengage the roughing pump by closing its isolation valve (the roughing pump may be shutdown at this point).
6. Wait for the system to reach needed pressure and perform desired experiment.

### **Venting**

1. CLOSE the gate valve.
2. Ensure the roughing pump isolation valve is closed.
3. Open the hand relief valve on the left side of the chamber to bring the chamber up to atmosphere.
4. LEAVE the cryopump running.

### **Hot Start**

The cryopump normally operates 24/7. If it is not currently running, and the chamber is system is ready to be pumped down, follow these steps:

1. Ensure the gate valve is CLOSED.
2. Close the chamber door.
3. OPEN the cryopump isolation valve (located under the backside of the chamber).

4. Begin pumping down the system with the roughing pump.
5. When the system reaches  $5E-03$  Torr, CLOSE the cryopump isolation valve.
6. Start the cryopump.
7. OPEN the gate valve.
8. Disengage the roughing pump by closing its isolation valve (the roughing pump may be shutdown at this point).
9. Wait for the system to reach needed pressure and perform desired experiment.

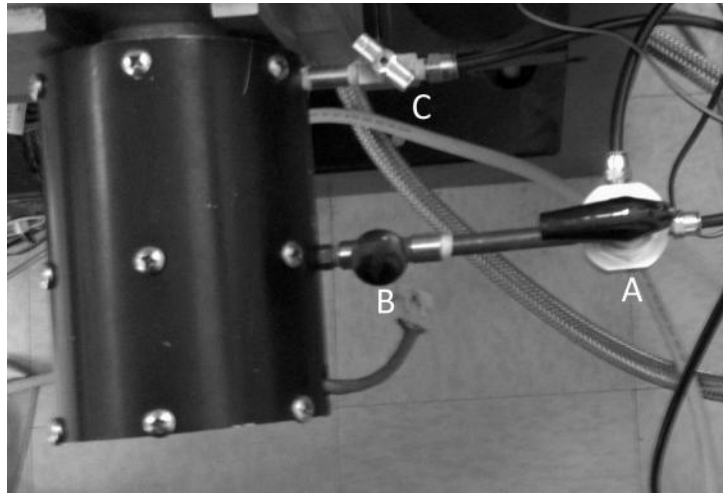


**Figure 79: Gate Valve Displaying Three Valves for Operation (A, B, C)**

**Opening the Gate Valve (Figure 79):**

1. Turn Valve A counter-clockwise so it is pointing towards the chamber.
2. Open Valve B by turning it counter-clockwise.
3. Open Valve C by turning it counter-clockwise with finesse.
4. Wait a few moments to ensure the gate valve is fully open.
5. Close Valve B by turning it clockwise.
6. Close Valve C by turning it clockwise.

### **Closing the Gate Valve**

1. Turn Valve A clockwise so it is pointing towards the wall.
2. Open Valve B by turning it counter-clockwise.
3. Open Valve C by turning it counter-clockwise.
4. Wait for a few moments to ensure the gate valve is fully closed.
5. Close Valve C by turning it clockwise.
6. Close Valve B by turning it clockwise.

Revised by Peter Bumbarger on 2/17/2012